Experimental and Theoretical Studies of a Low NO$_x$ Swirl Burner

by

Øystein Spangelo

A Thesis Submitted to
The Norwegian University of Science and Technology
for the degree of

Doktor Ingeniør

September 2004
The Norwegian University of Science and Technology
Faculty of Engineering Science and Technology
Department of Energy and Process Engineering
7491 Trondheim, Norway

EPT 2004:11

NTNU

The Norwegian University of Science and Technology
Norges Teknisk-Naturvitenskapelige Universitet

ADDRESS:	TELEPHONE			TELEFAX	
NTNU	Switchboard NTNU:	73 59 40 00		Department office:	73 59 83 90
DEPARTMENT OF ENERGY AND	Department office:	73 59 27 00		Hydropower section:	73 59 38 54
PROCESS Engineering	Hydropower section:	73 59 38 57			
Kolbjørn Hejes vei 1A					
N-7491 Trondheim - NTNU					

Title of report Experimental and Theoretical Studies of a Low NO$_x$ Swirl Burner	Date 02.06.04
	No. Of pages/appendixes 98/122
Author Øystein Spangelo	Project manager Otto K. Sønju
Division Faculty of Engineering Science and technology Department of Energy and Process Engineering	Project no.
ISBN no. 82-471-6370-5 82-471-6369-1 (electronic)	Price group

Client/sponsor of Project The Research Council of Norway	Client's ref.

Abstract

Nitrogen oxides emitted to the atmosphere can cause health problems for humans and environmental problems such as acid rain and global warming. The main part of the world energy consumption involves combustion; hence nitrogen oxide abatement in combustion is an important research field. Formation and reduction of NO$_x$ in combustion and the current regulations on NO$_x$ emissions are reviewed.

A novel low NO$_x$ swirl stabilized gas burner concept, the Swirl Burner, has been studied experimentally, theoretically and numerically. Flame stabilization, rapid air and fuel mixing and internal flue gas recirculation are provided by a strongly swirling flow generated in this patented burner concept. NO$_x$ emissions have been measured below 25 and 45 ppmv dry corrected to 3% O$_2$ in the flue gases using methane and propane as fuel respectively.

Studying the effect of varying geometrical parameters on the emissions of NO$_x$, fuel and air supply pressure and flame stability, have resulted in an optimized burner design. The optimized Swirl Burner has successfully been scaled from a 200 kW burner down to a 20 kW burner and up to a 370 kW burner, using a constant velocity scaling criteria which is the most commonly used scaling criteria for industrial burners. Experiments with the scaled burners have revealed that the fuel to air momentum should be preserved while scaling the burner. The 200 kW and the 370 kW burners were operated stable with the boiler to burner diameter (confinement) ratio in the range 5.3-6.7. The 20 kW burner, which was operated in an un-cooled and a water-cooled combustion chamber with confinement ratio of 8.1, was found to have a narrower range of stable operation with regards to thermal throughput. High post-flame heat extraction, which is enhanced by increased confinement ratio and combustion chamber cooling, reduces the emissions of NO$_x$, but might cause flame instabilities.

NO$_x$ emissions measured from the three Swirl Burners scale well with NO$_x$ scaling correlations based on flame volume as a leading-order parameter for NO$_x$ formation (Weber, 1996). The correlations consider the effect of heat extraction on flame volume and emissions of NO$_x$. These correlations indicate that the heat extraction from the 20 kW burner is increasing with increasing thermal throughput. The 200 kW and the 370 kW burners were, from the correlations, found to operate with constant heat extraction.

Flame volume and shape are studied by non-intrusive measurements of OH radicals with the 20 kW burner using laser induced fluorescence. The measurements show that the flame volume is reduced with increasing thermal throughput. Measurements of NO$_x$ from this burner also show a reduction with increasing thermal throughput. These results support the theoretical considerations of the flame volume as being the leading-order parameter for NOx formation.

An evaluation of turbulence models and combustion models suitable for studying the Swirl Burner by computational fluid dynamics has been carried out. For this evaluation, a 2D computational model of the 20 kW burner has been used. For closure of the Reynolds Averaged Navier-Stokes equations for turbulent flow, three models have been evaluated. These are the standard k-ε model, the RNG k-ε model and the Reynolds Stress model. Also for modelling of combustion, three models have been evaluated, namely the Eddy Dissipation model, the Equilibrium PDF model and the Flamelet PDF model. For studying the Swirl Burner, a combination of the Reynolds Stress model and the Flamelet PDF model were found to be most suitable for modelling of turbulence and combustion respectively. Computational results with the 20 kW burner indicate that flue gases are recirculated into a central toroidal recirculation zone downstream the burner exit. The computations are further compared with the OH concentrations measured with laser induced fluorescence.

	Indexing Terms: English	Norwegian
Group 1	Heat Engineering	Varmeteknikk
Gruup 2	Combustion	Forbrenning
Selected by author	Natural gas	Naturgass
	NO$_x$	NO$_x$
	Burners	Brennere

Abstract

Nitrogen oxides emitted to the atmosphere can cause health problems for humans and environmental problems such as acid rain and global warming. The main part of the world energy consumption involves combustion; hence nitrogen oxide abatement in combustion is an important research field. Formation and reduction of NO_x in combustion and the current regulations on NO_x emissions are reviewed.

A novel low NO_x swirl stabilized gas burner concept, the Swirl Burner, has been studied experimentally, theoretically and numerically. Flame stabilization, rapid air and fuel mixing and internal flue gas recirculation are provided by a strongly swirling flow generated in this patented burner concept. NO_x emissions have been measured below 25 and 45 ppmv dry corrected to 3% O_2 in the flue gases using methane and propane as fuel respectively.

Studying the effect of varying geometrical parameters on the emissions of NO_x, fuel and air supply pressure and flame stability, have resulted in an optimized burner design. The optimized Swirl Burner has successfully been scaled from a 200 kW burner down to a 20 kW burner and up to a 370 kW burner, using a constant velocity scaling criteria which is the most commonly used scaling criteria for industrial burners. Experiments with the scaled burners have revealed that the fuel to air momentum should be preserved while scaling the burner. The 200 kW and the 370 kW burners were operated stable with the boiler to burner diameter (confinement) ratio in the range 5.3-6.7. The 20 kW burner, which was operated in an un-cooled and a water-cooled combustion chamber with confinement ratio of 8.1, was found to have a narrower range of stable operation with regards to thermal throughput. High post-flame heat extraction, which is enhanced by increased confinement ratio and combustion chamber cooling, reduces the emissions of NO_x, but might cause flame instabilities.

NO_x emissions measured from the three Swirl Burners scale well with NO_x scaling correlations based on flame volume as a leading-order parameter for NO_x formation (Weber, 1996). The correlations consider the effect of heat extraction on flame volume and emissions of NO_x. These correlations indicate that the heat extraction from the 20 kW burner is increasing with increasing thermal throughput. The 200 kW and the 370 kW burners were, from the correlations, found to operate with constant heat extraction.

Flame volume and shape are studied by non-intrusive measurements of OH radicals with the 20 kW burner using laser induced fluorescence. The measurements show that the flame volume is reduced with increasing thermal throughput. Measurements of NO_x from this burner also show a reduction with increasing thermal throughput. These results support the theoretical considerations of the flame volume as being the leading-order parameter for NO_x formation.

An evaluation of turbulence models and combustion models suitable for studying the Swirl Burner by computational fluid dynamics has been carried out. For this evaluation, a 2D computational model of the 20 kW burner has been used. For closure of the Reynolds Averaged Navier-Stokes equations for turbulent flow, three models have been evaluated. These are the standard *k*-ε model, the RNG *k*-ε model and the Reynolds Stress model. Also for modelling of combustion, three models have been evaluated, namely the Eddy Dissipation model, the Equilibrium PDF model and the Flamelet PDF model. For studying the Swirl Burner, a combination of the Reynolds Stress model and the Flamelet PDF model were found to be most suitable for modelling of turbulence and combustion respectively. Computational results with the 20 kW burner indicate that flue gases are recircu-

ABSTRACT

lated into a central toroidal recirculation zone downstream the burner exit. The computations are further compared with the OH concentrations measured with laser induced fluorescence.

Acknowledgements

ACKNOWLEDGEMENTS

Table of Contents

List of Figures

List of Tables

Symbols

Arabic

C	Constant	
c_p	Specific heat at constant pressure	[J/kg K]
d	Diameter	[m]
D	Diffusion coefficient	[m^2/s]
E	Energy	[J]
E_a	*A*ctivation energy	[J/mol]
f	Correction factor (equation (5–3))	
f	Frequency	[1/s]
f	Mixture fraction	
F	External body force	[kg/m^2 s]
Fr	Froude number: u^2/dg	
g	Gravitational constant: 9.81	[m/s^2]
G	Axial flux of momentum	
h	Enthalpy	[J/kg]
h	Heat transfer coefficient in *Nu*-number	[W/m^2 K]
h	Planck's constant: 6.626068x10^{-34}	[Js]
I	Light intensity detected by ICCD camera	
J	Diffusion	[kg/m^2 s]
k	Conductivity	[W/m K]
k	Rate constant	
k	Turbulent kinetic energy	[m^2/s^2]
K	Proportionality constant (equation (2–11))	
l	Length	[m]
m	Mass	[kg]
MW	Molecular weight	[g/mole]
Nu	Nusselt number: hd/λ	

SYMBOLS

Arabic

p	Pressure	[bar]
p	Probability	
Q	Thermal input	[kW]
Q_{EAS}	Skewness of grid elements	
r	Radius	[m]
r	Radial coordinate	
R	Production by chemical reaction	[kg/s]
R	Universal gas constant: 8.315	[J/mol K]
S	Swirl number: $G_\theta/G_x r$	
S	Source-term	
t	Time	[s]
T	Temperature	K
u	Velocity	[m/s]
V	Volume	[m^3]
x	x-coordinate	
X	Mole fraction measured by OH LIF	
y	y-coordinate	
Y	Mass fraction	
z	z-coordinate	

Greek

α	Inverse effective Prandtl numbers	
β	Exit angle, swirl vanes	°
ε	Emissivity	
ε	Dissipation of turbulent energy	[m^2/s^3]
ϕ	Equivalence ratio	
ϕ	Fluid property	
κ	von Kármán constant: 0.4187	

Greek

λ	Thermal conductivity	[W/m K]
λ	Excess air ratio	
μ	Viscosity	[kg/m s]
θ	Angle	°
ρ	Density	[kg/m^3]
σ	Stefan Boltzmann constant: 5.67x10^{-08}	[W/m^2 K^4]
σ	Turbulent Prandtl number	
τ	Stress tensor	[kg/m s^2]
τ	Fraction of time	[s]

Subscripts

∞	Value for the surroundings
0	Initial state (burner nozzle exit)
1	Reaction number
1	State 1
2	State 2
3	State 3
4	State 4
b	Burnt
eff	Effective
f	Fuel
h	Hub
h	Heat
i	Direction
j	Direction
k	Direction
m	Measured
max	Maximum

Subscripts

min	Minimum
n	Chemical species
o	Oxidizer
p	Products
pr	Prompt NO
r	Radial coordinate
rad	Radiative
scal	Scaled parameter
t	Turbulent
x	Axial coordinate, x-coordinate
y	y-coordinate
z	z-coordinate

Greek sub-scripts

θ	Angular coordinate

Diacritical marks

$\dot{a}$	Indicates rate per time unit	[1/s]
$\bar{a}$	Indicates average value	
a'	Indicates fluctuating value	

Abbreviations

ASM	Algebraic stress model
BAT	Best available technique
BREF	BAT reference document
CAD	Computer Aided Design
CEN	Comité Européen de Normalisation
CFD	Computational fluid dynamics
CRZ	Corner recirculation zone
CSPIM	Catalytically supported PIM
CTRZ	Central toroidal recirculation zone
EDC	Eddy dissipation concept
EI	Emission index
FGR	Flue gas recirculation
FS	Full scale
ICCD	Intensified charge coupled device
IMP	Isolated measurement pod
LIF	Laser induced fluorescence
PDF	Probability density function
PIM	Porous inert media
ppmv	Parts per million volume
RANS	Reynolds averaged Navier-Stokes
RNG	Renormalization group
RSM	Reynolds stress model
SCAQMD	South coast air quality management district
SLS	Selective laser sintering
YAG	Yttrium aluminium garnet

1   Introduction

1.1   Background

"Fire has been man's fierce ally throughout his struggle for existence and ascendency. Fire is now man's slave - rebellious and mysterious - enabling his most daring designs to be constructed and his most bold adventures to be achieved." These are the poetic words of A. C. Egerter (1957), the first general editor of Combustion and Flame, the official journal of The Combustion Institute. Combustion, mankind's oldest technology, still provides more than 95% of the energy consumed throughout the world (Griffiths and Barnard, 1995), and despite the continuous search for alternative energy sources, there is little doubt that combustion will remain important for many years to come. While early combustion research was focused on efficiency of combustion processes, today research on pollutant formation in combustion is becoming increasingly important.

Among fossil fuels, natural gas is the cleanest. Natural gas is primarily composed of methane with very low or no nitrogen or sulphur content. During combustion very small amounts of sulphur dioxide and nitrogen oxides and virtually no ash or particulate matter are released. Coal and oil, on the other hand, have much higher nitrogen and sulphur contents and a higher carbon ratio than natural gas. By combustion of natural gas less carbon dioxide will be produced per energy unit burnt compared to coal and oil.

Natural gas is considered as a clean fuel compared to the other fossil fuels, but formation of unwanted pollutants, such as nitrogen oxides, are still taking place while burning this fuel. Research in the field of natural gas combustion to increase combustion efficiency and abate formation of pollutants emitted to the atmosphere are therefore still of importance.

1.2   Objectives

The objectives of this study are to investigate and develop a novel low NO_x swirl stabilized gas burner experimentally, theoretically and numerically. The aim of the study is to achieve a better understanding of the mechanisms important for formation of nitrogen oxides in this burner. This will be done by:

1. Studying the effects of burner scaling on emissions of nitrogen oxides.

2. Non-intrusive measurements of in-flame OH radicals using laser induced fluorescence (LIF).

3. Numerical computations of fluid flow and combustion.

A review on literature and theory on nitrogen oxides formation and reduction in combustion is presented. Available theory on burner scaling is then given, as well as background theory on the non-intrusive measurement technique used (LIF), and on computational fluid dynamics (CFD) with reacting flow. The numerical calculations presented in this study are made with the commercial CFD code FLUENT from Fluent Inc. (2003).

The experimental work carried out on the 200 kW burner for this study has been presented at the 7th International Conference on Energy for a Clean Environment in Lisbon, Portugal, in July 2003 by Spangelo et al. (2003), and has been accepted for publishing in Clean Air - International Journal on Energy for a Clean Environment.

A part of this study included a twelve month stay at the University of Leeds, Department

of Fuel and Energy in Leeds, U.K., starting in December 2002. The in-flame OH measurements of the burner using LIF and most of the CFD calculations of the burner were carried out during the stay at the University of Leeds.

1.3   Outline of the thesis

The thesis is organized in chapters as follows:

In chapter 2, fundamental theory on flames is first presented, followed by literature and theory used in this study. This includes formation and reduction of nitrogen oxides in burners and current emission regulations for nitrogen oxides. A selection of commercial low NO_x burners available on the market is also presented. Scaling correlations for diffusion flames and confined burners found in literature are given together with the most common scaling criteria for scaling of industrial burners. Background theory on the non-intrusive measurement technique used in this study (LIF) can also be found in this chapter. At last, governing equations for fluid flow and heat transfer applied in computational fluid dynamics (CFD) are presented. Models for computations of turbulent flow and combustion that will be used in this study are also presented here.

In chapter 3, the apparatus that has been used in the experimental work of this study is described. This consists of the burner, the boilers and combustion chamber used, the flue gas analysers and the equipment used for the laser induced fluorescence (LIF) measurements.

In chapter 4, the experimental work for this study can be found. The experiments presented at the 7th International Conference on Energy for a Clean Environment (Spangelo et al., 2003), are first summarized briefly, and the complete paper can be found in appendix A. Scaling of the burner is then presented, followed by descriptions of the experiments carried out with the up-scaled and the down-scaled burners. Investigations made with the down-scaled burner using the non-intrusive measurement technique LIF are then described. These experiments include the calibration of the LIF equipment using a McKenna burner. The experiments described in chapter 4 are followed by analysis and discussion of the experimental results.

In chapter 5, the numerical computations of fluid flow and combustion in the burner using FLUENT (Fluent Inc., 2003) are presented. The setup of the computational model is described, followed by an evaluation of computational models for turbulent flow and combustion. The computational results achieved with the chosen models are then presented and discussed. Computations are compared with measured OH concentrations described in chapter 4 using LIF. An attempt to calculate the NO_x concentrations from the computational results has also been made in chapter 5.

In chapter 6, overall conclusions and recommendations for further work are provided.

1.4   Contribution to original knowledge

The Swirl Burner studied, is a novel low NO_x burner design. The burner design has first been published by Spangelo et al. (2003), which is a part of this thesis (appendix A). This implies that work done with this burner, is new knowledge. The experimental, theoretical and numerical work in this study can be found in chapter 4 and chapter 5. Some of the results from this study are outlined in the following.

The Swirl Burner utilizes internal flue gas recirculation induced by a strong swirling flow. The internal recirculation is a known effect of rotational flow. Taking advantage of this

effect for reduction of NO_x emissions was first done with the first prototype of the Swirl Burner (Røkke, 1994). This study provides further knowledge and insigth into the combustion mechanisms of the Swirl Burner.

NO_x emissions from this burner have been proven to be below 45 ppmv dry corrected to 3% O_2 in the flue gases using propane as fuel. Using methane, which is the main component of natural gas, as fuel, emissions of NO_x have been proven to be below 25 ppmv dry corrected to 3% O_2 in the flue gases. These measurements are described in chapter 4. These emissions are low enough to compete with the most comparable fan burners on the market today, such as the Walter Dreizler ARZ and ARZ Super burners in table 2–4 in chapter 2.

An experimental study of the effect of changing geometrical parameters, such as arrangement of fuel nozzles, variation of the swirl number and positioning of the gas tube relative to the burner exit is provided in appendix A.

In chapter 4, it has been validated that the constant velocity scaling criteria described in chapter 2.3.2 can be successfully used for scaling of the Swirl Burner. It has been found important to keep the fuel to air momentum constant while scaling the burner. Weber (1996) stated that there was no upper limit for the boiler to burner diameter ratio (confinement ratio) for the burners in his scaling study. In the present study, a high confinement ratio was found to cause flame instabilities, possibly due to the increased post-flame heat extraction.

An encouraging result from this study is found in chapter 4.6.1. NO_x emissions from the Swirl Burner were found to scale well with NO_x scaling correlations (Weber, 1996) based on flame volume as the leading-order parameter for the formation of NO_x. These correlations consider the effect of heat extraction on flame volume and emissions of NO_x.

The shape and volume of the 20 kW Swirl Burner have been investigated by non-intrusive measurements of the OH radical in the flame. The measurements, described in chapter 4.5, demonstrated that the emissions of NO_x were reduced with reduced flame height and volume. This supports the conclusions that flame volume is the leading-order parameter for the formation of NO_x in the Swirl Burner.

The recirculation of flue gas in a central toroidal recirculation zone downstream the Swirl Burner exit has been validated by computational fluid dynamic modelling of the burner using FLUENT in chapter 5.

2   *Literature and Theory*

2.1   Flames

The process of combustion couples phenomena of chemistry and physics. In chemistry, combustion begins with a self-supported, exothermic reaction. The physics involved are principally those which pertain to transport of material and energy (Griffiths and Barnard, 1995). Fundamentals of combustion and flames have been the subject of extensive investigation for the last century, and comprehensive studies can be found in many textbooks such as Griffiths and Barnard (1995), Kuo (1986), Warnatz et al. (1999) and Williams (1985).

When entering a flame, the temperature of a cold reactant flow is increased. An element of the gas flow can receive heat by either chemical reactions occurring within it or by heat transport from the hotter gases ahead of it (Griffiths and Barnard, 1995). This process is illustrated by the profiles of temperature and concentration for a one-dimensional premixed flame in figure 2–1. In the preflame zone, the steep temperature increase is caused by heat transport from the hotter gases in the reaction zone. At higher temperatures, the reaction rate has increased sufficiently for a significant amount of heat to be released by chemical reaction, causing a further temperature increase in the reaction zone. The temperature eventually reaches a constant value in the products zone, where all the fuel has been consumed and reaction has ceased. Parallel to the temperature increase, the reactants concentrations are initially reduced by diffusion of fuel into the flame and subsequently consumption by chemical reaction. The products concentrations naturally increase as the reactants are consumed. Due to the relatively short reaction zone residence time, some intermediate species do not reside here for a sufficiently long period of time for thermodynamic equilibrium to establish, and the intermediate species concentration profile are seen to continue into the products zone in figure 2–1.
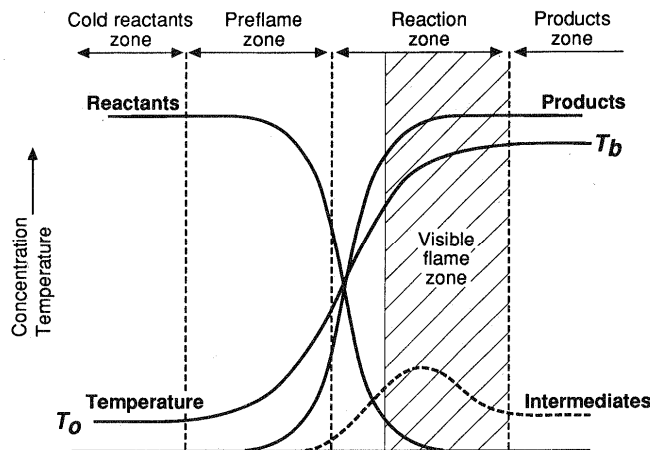
Figure 2–1 Profiles of concentration and temperature in a one-dimensional, premixed, adiabatic flame (Griffiths and Barnard, 1995).

In a premixed flame as described above, fuel and oxidizer are perfectly mixed before the reaction zone. In diffusion flames, the fuel and oxidizer gas flow are separated, and combustion occurs at the interface between the flows. In this case, the burning process depends more on the rate of mixing than on the rate of the chemical processes involved (Griffiths and Barnard, 1995). In the cross-section of a laminar diffusion flame, where the fuel flow is surrounded by oxidizer, it can be found that the fuel concentration has a max-

imum on the axis and falls rapidly at the flame boundary (figure 2–2). The oxygen concentration also decreases close to the flame and falls approximately to zero at the boundary. The concentration of products on the other hand, is at maximum at the boundary, where the major extent of reaction occurs, and falls away both towards the axis and into the surroundings. The flame front defines the surface where the combustion is complete, but since reaction normally is very rapid, it represents the position at which the fuel to oxygen ratio becomes stoichiometric.
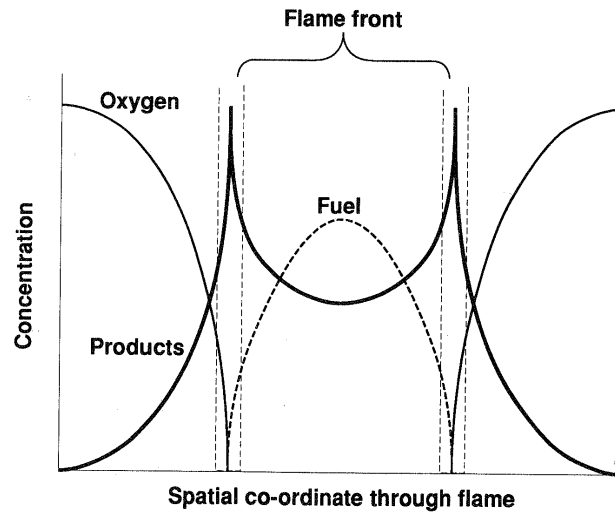
Figure 2–2 Spatial concentration profiles for fuel, oxygen and reaction products through a cross-section of a laminar diffusion flame (Griffiths and Barnard, 1995).

Change in length and shape of a diffusion flame produced by a circular fuel jet into quiescent air with increasing jet velocity, is illustrated in figure 2–3. While studying diffusion flames, Hottel and Hawthorne (1949) observed that the height of a laminar diffusion flame was increasing with increasing port velocity. This is due to molecular diffusion being the controlling mechanism for mixing of fuel and surrounding air. At some critical velocity, in the region of transition from laminar to turbulent flow, the flame breakpoint was observed to start at the flame tip and moved down towards the port rapidly with increasing port velocity. In the turbulent region, molecular diffusion is no more controlling, and turbulent mixing along the flame surface now increases the mass exchange considerably. For fully developed turbulent flow, Hottel and Hawthorne (1949) found the breakpoint height and the flame height to be constant with increasing port velocity. It has been shown by Suris et al. (1977) and later by Sønju and Hustad (1984), that the height of buoyant jet flames can be correlated by the Froude number of the jet to the power of 1/5.
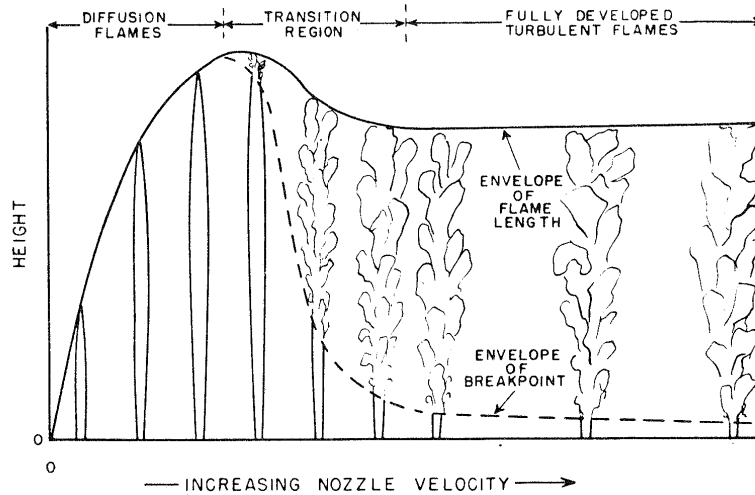
Figure 2–3 Characterization of diffusion flame structures with increase in nozzle velocity (Hottel and Hawthorne, 1949).

2.2 Nitrogen oxides

2.2.1 Introduction

Nitrogen oxide is a main component in the formation of ground-level ozone, but can also react to form nitrate particles and acid aerosols, which together with NO_2 can affect human health by causing respiratory problems. Further, the nitrogen oxides (denoted as NO_x) NO and NO_2 contributes to formation of acid rain, while nitrous oxide which also is considered as NO_x, is a contributor to global warming (U.S. Environmental Protection Agency, 1998). Consequently, reduction of NO_x formation has become a major topic in combustion research. Emission reductions can be achieved by understanding the chemical kinetics producing NO_x and their interaction with fluid dynamics. Four main routes to formation of NO_x are identified so far (Bowman, 1992).

2.2.2 NO_x formation mechanisms

Generally, when using a gaseous fuel, the main pollution components are NO_x, with NO as the dominating component. NO_x in gas combustion is mainly formed by three mechanisms: the thermal NO mechanism originally proposed by Zeldovich (1946), the prompt NO mechanism first postulated by Fenimore (1971) and the nitrous oxide (N_2O) route to NO. The different mechanisms are affected in different ways by temperature, residence time, oxygen concentration and fuel type. Thermal NO and prompt NO are the most important for fan driven gas burners.

Thermal NO is formed by the following elementary reactions (extended Zeldovich mechanism):

$$O + N_2 \leftrightarrow NO + N \qquad (2–1)$$

$$N + O_2 \leftrightarrow NO + O \qquad (2–2)$$

$$N + OH \leftrightarrow NO + H \qquad (2–3)$$
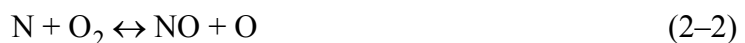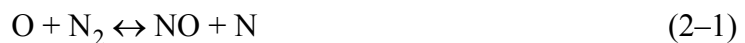
Where equation (2–1) is the rate limiting step because of its high activation energy (Warnatz et al., 1999), requiring high temperatures to give any significant contribution to the total NO formation. From equation (2–1), equation (2–2), equation (2–3) and the assumption that $d[\mathrm{N}]/dt \approx 0$, it can be obtained for the formation of NO that:

$$\frac{d[\mathrm{NO}]}{dt} = 2k_1[\mathrm{O}][\mathrm{N}_2] \tag{2–4}$$

Where [] denotes concentration and k_1, the rate coefficient of the reaction in equation (2–1), is given by (Warnatz et al., 1999):

$$k_1 = 1.8 \times 10^{14} \exp(-318\ \mathrm{kJ} \cdot \mathrm{mol}^{-1}/(RT))\ \ \mathrm{cm}^3/(\mathrm{mol} \cdot \mathrm{s}) \tag{2–5}$$

From equation (2–4) and (2–5), it can be seen that NO formation can be controlled by [O], [N_2], temperature and residence time. Thermal NO formation can, therefore, be minimized by reducing peak temperatures, by reducing oxygen levels especially at peak temperatures and by reducing the time of exposure to peak temperatures. According to Turns (1995), the formation of NO via the thermal NO mechanism can be ignored at temperatures below about 1800 K.

Prompt NO was first identified by Fenimore (1971), who suggested that hydrocarbon radicals reacted with molecular nitrogen in the primary reaction zone, explaining the promptly formation of NO not predicted by the thermal NO mechanism. The prompt NO mechanism involves molecular nitrogen from the combustion air reacting with the CH radical, which is an intermediate at the flame front only, forming hydrocyanic acid (HCN). The prompt NO route is usually given by (Li and Williams, 1999):

$$\mathrm{N}_2 + \mathrm{CH} \leftrightarrow \mathrm{HCN} + \mathrm{N} \tag{2–6}$$

$$\mathrm{HCN} + \mathrm{O} \leftrightarrow \mathrm{NCO} + \mathrm{H} \tag{2–7}$$

From equation (2–6) and equation (2–7) the N, HCN and NCO will react further and ultimately lead to the formation of NO_x. This mechanism together with the thermal mechanism is indicated in the diagram in figure 2–4. Prompt NO is favoured by fuel rich conditions and its formation takes place at lower temperatures (about 1000 K) than thermal NO.
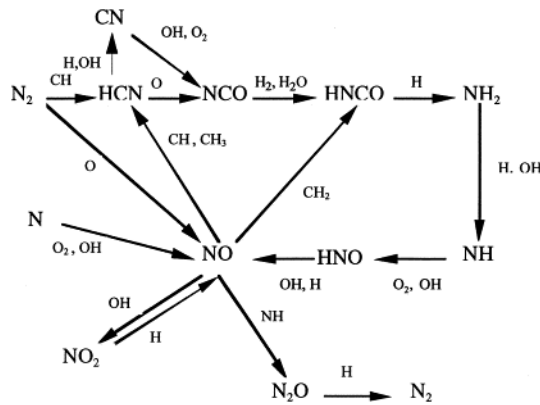
Figure 2–4 Diagram of NO_x mechanism (Xue and Aggarwal, 2003).

NO formation by the nitrous oxide route increases in importance under conditions such as lean mixtures, high pressure and lower combustion temperatures (Bowman, 1992). This route is therefore more important in other applications, e.g. gas turbines, than in the burners considered in this thesis. Another mechanism, not considered to be of importance here, is the conversion of fuel bound nitrogen to NO, which is the case especially for some liquid and solid fuels.

2.2.3 Emission limits and regulations

In 1999, the "Gothenburg Protocol to Abate Acidification, Eutrophication and Ground-level Ozone" was adopted (UNECE, 2004). This protocol sets the emission limits of the four pollutants sulphur, NO_x, VOCs and ammonia. For Europe the consequence of the protocol is a 41% reduction of NO_x emissions compared to 1990. Norway is committed to reduce the emissions of NO_x to 156000 tons by 2010 (SFT, 2002). In 1999 the total Norwegian NO_x emissions were 228000 tons. The historical Norwegian emissions of NO_x are illustrated together with a prognosis of future NO_x emissions in figure 2–5. As seen, there has been no significant reduction of the Norwegian NO_x emissions since 1990, and according to the forecast in figure 2–5, the prospects for Norway to fulfil the commitments by 2010 are rather poor. The Gothenburg protocol also requires the best available techniques (BAT) to be used to keep emissions down for specific emission sources (e.g. combustion plant, electricity production, dry cleaning, cars and lorries).
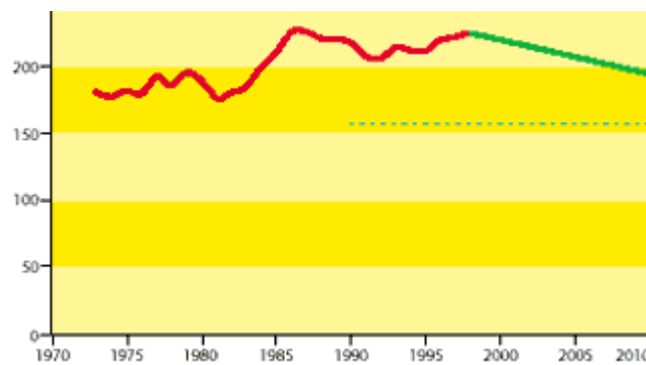
Figure 2–5 NO_x emissions to the atmosphere in Norway (in 1000 tons), historical data (red line) and prognosis (green line). Norway's commitment in the Gothenburg protocol is indicated by the dotted line (SFT, 2002).

To reach the requirements in the Gothenburg protocol, the European Union adopted a directive in 2001 to limit emissions of certain pollutants into the air from large combustion plants (EU Directive 2001/80/EC). This directive sets the emission limits for existing and new large combustion plants (> 50 MWth). The European Union also adopted a directive in 1996 to apply BATs for determining emission limits, the IPPC directive (EU Directive 96/61/EC). Industrial plants covered by the IPPC directive are given individual emission permits based on the BAT which are defined in a BAT Reference document (BREF). For large combustion plants (> 50 MWth), a draft BREF is available from the European Commission (2003). The current NO_x emission limits for large combustion plants (> 50 MWth) set out in the 2001/80/EC EU directive and the proposed BREF for boilers in large combustion plants which will be adopted into the 96/61/EC EU directive are summarized in table 2–1. The suggested BAT to reach the BREF levels for boilers is low-NO_x burners. In addition to the EU legislation mentioned here, each member state might adopt stricter national emission legislation.

In the United States, the most stringent emission limits are found in California in the South Coast Air Quality Management District (SCAQMD). The emissions limits for new or modified combustion equipment in SCAQMD are defined by the BAT. In contrast to the European Union where only large combustion plants (> 50 MWth) are required to meet the limits defined by the BAT, the emission limits in the SCAQMD are required for boilers rated over only 2 MMBtu/hr (585 kW). The emission limits for new boilers in SCAQMD are found in table 2–2. For existing boilers the NO_x emission limit is set to 30 ppm at 3% O_2.

In addition to national emission legislation, there are various environmental labelling programs. The idea of environmental labelling is to use consumers' environmental awareness and competition among manufacturers to promote the environmental quality of consumer goods and products (Müller, 2002). By fulfilling the requirements given by an environmental label standard, manufacturers are allowed to use the label for advertisement and marketing of their products. Such a label is the german Blue Angel which has been in operation since 1977 (Müller, 2002). The Blue angel standards applicable for small boilers and burners fuelled by natural gas are given in table 2–3.

Table 2–1 EU NO_x emission limits for large combustion plants (> 50 MWth) at 3% O_2 in flue using natural gas.

EU Directive	Plant	NO_x [mg/Nm^3]	NO_x [ppm]
2001/80/EC	New, 50 - 300 MWth	150	73
	New, > 300 MWth	100	49
	Existing, 50 - 300 MWth	300	147
	Existing, > 300 MWth	200	98
96/61/EC (Draft Bat Reference)	Boilers, new	< 50	< 24
	Boilers, existing	50 - 80	24 - 43

Table 2–2 SCAQMD NO_x emission limits for new boilers at 3% O_2.

Boiler size	NO_x [ppm]	BAT
< 20 MMBtu/hr (5.9 MWth)	12	Low NO_x burner
> 20 MMBtu/hr (5.9 MWth)	9	Low NO_x burner

Table 2–3 Blue Angel: NO_x emission limits for small heating devices.

Standard	Description	Thermal output [kW]	NO_x [ppm @ 0% O_2]
RAL-UZ 41	Combined Burner- and Boiler Units equipped with Gas Burner and Fan.	> 70	34 (70 mg/kWh)
RAL-UZ 80	Low-Emission Fan-Assisted Gas Burners.	> 120	34 (70 mg/ kWh)
RAL-UZ 61	Low-emission and Energy-saving Gas-fired Calorific-Value Heating Devices.	> 70	29 (60 mg/ kWh)

2.2.4 NO_x reduction techniques

NO_x emissions from combustion processes can be reduced by either modifying the combustion device to minimize the amount of NO_x generated in the first place, often referred to as primary measures, or by secondary measures such as catalytic conversion or ammonia addition in the flue gases to remove the NO_x generated in the combustion. Some well known primary measures to reduce the NO_x formated in burners will be explained here. These techniques are also discussed by Røkke (1994), Warnatz et al. (1999) and Zepter (2003).

As described in chapter 2.2, the formation of NO_x via the thermal NO mechanism is strongly dependent of the combustion temperature. The combustion temperature will be highest at a fuel and air mixture close to stoichiometric ($\lambda = 1$) (Røkke, 1994). At fuel lean ($\lambda > 1$) or fuel rich conditions ($\lambda < 1$), the combustion temperature will be considerably lower than at stoichiometric mixtures. This behaviour is utilized in staged combustion. In staged combustion, which is illustrated in figure 2–6, the excess air ratio (λ) is shifted away from stoichiometric. For air staging (figure 2–6a), the first stage is fuel rich ($\lambda < 1$) with secondary air supplied in the next stage to ensure that the overall excess air ratio is maintained in the burner. In between the stages the combustion are cooled to keep the combustion temperatures low. Fuel staging (figure 2–6b) is the opposite of air staging. The first stage is now fuel lean and secondary fuel is added in the next stage until the excess air ratio matches the desired overall burner ratio ($\lambda = 1.15$ for 3% O_2 in flue gases). Both air and fuel staging can be applied in more than two stages as long as the overall excess air ratio for the combustion system is kept constant.
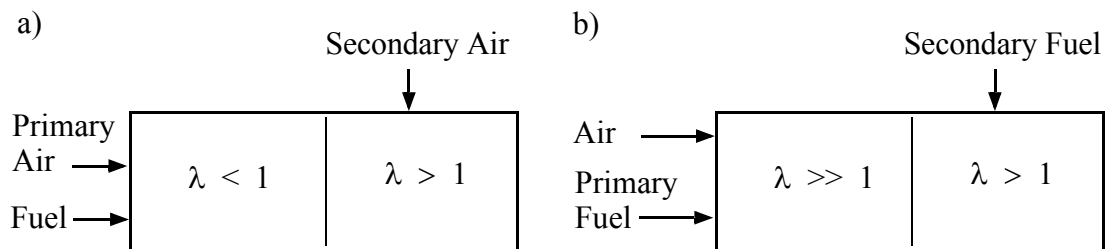
Figure 2–6 Schematic drawing of (a) air staging, and (b) fuel staging.

Premixing in combustion means that the fuel and air is perfectly molecular mixed before the ignition takes place. For the control of NO_x formation in combustion this technique is advantageous because it enables full control over the air and fuel ratio throughout the

combustion and thus control of the combustion temperature. By making the combustion fuel lean the temperatures are kept low and hence formation of NO_x via the thermal NO mechanism can be reduced. The perfect mixing of fuel and air also prevents unwanted non-uniformity of the excess air ratio in the combustion which would cause less control of the NO_x formation (Røkke, 1994). A limitation to the use of premixing in industrial burners is related to safety. The premixed fuel-air mixture is highly combustible and might cause flashbacks in the burner. A diagram of a premix burner is shown in figure 2–7. Fuel and air is mixed before a flame-arrestor that prohibits the flame to propagate into the mixing chamber. The premixed flame is stabilized in the wake of the bluff body. The disadvantages of premixing can be solved by utilizing partial premixing in staged combustion. The first stage can then be premixed fuel lean or fuel rich and the second stage will be a non-premixed stream of fuel or air respectively (Røkke, 1994). The first stage then have the advantage of being uniformly mixed and flashbacks can be avoided by premixing fuel and air below or above the flammability limit. According to Røkke (1994), premixed and partially premixed burners have a high reduction potential of NO_x, in some cases as high as 85 - 90% compared with non-premixed burners. A disadvantage of this NO_x reduction technique is the high excess air levels. For use in boilers this will reduce the boiler efficiency due to increased flue gas losses.
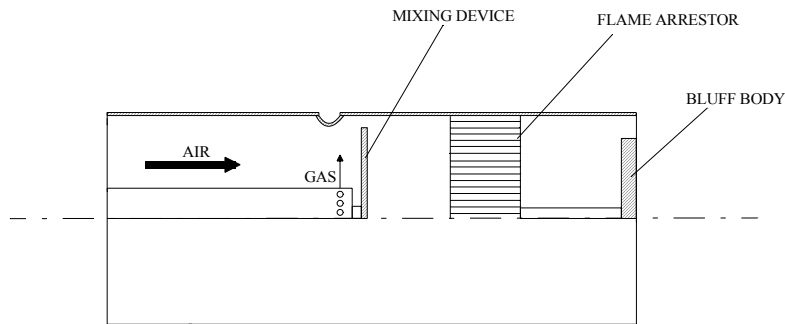
Figure 2–7 Premixed bluff-body burner (Røkke, 1994).

The peak flame temperatures can be reduced by adding an inert gas to the combustion gases (Røkke, 1994). The inert gas will require heat and hence lower the flame temperatures. By recirculating combustion products from the flue gas into the combustion gases, the formation of NO_x will be reduced due to the reduced temperatures. The recirculated combustion products will also lower the partial pressure of O_2 in the combustion and hence the reaction of oxygen and nitrogen to NO via the thermal NO mechanism is reduced. Flue gas recirculation (FGR) is in principle utilized in two ways, either by external or internal FGR. For external FGR, flue gases are extracted from the boiler outlet and are introduced into the combustion gases via external ducting. The principle of external FGR applied on a boiler is shown in figure 2–8. According to Røkke (1994), 70% reduction of NO_x can be achieved by applying external FGR.
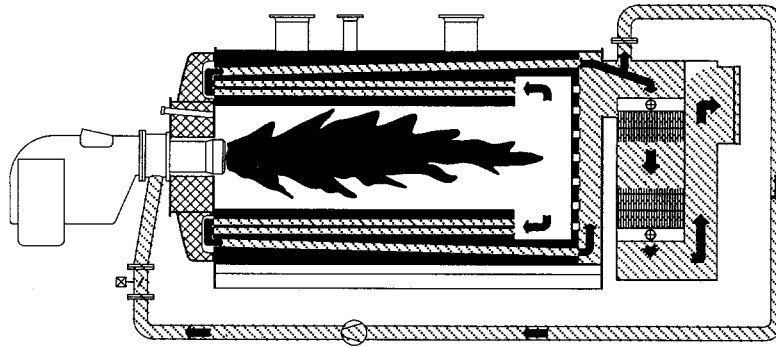
Figure 2–8 External flue gas recirculation system (Røkke, 1994).

An alternative to external FGR is internal FGR. For internal FGR, the flue gases are recirculated back to the combustion due to burner aerodynamics. Internal FGR might be induced by flue gases entraining a high velocity jet flame or by recirculation set up by the rotating flow in a swirl burner (Røkke, 1994). By using a recirculation cup on the burner head (figure 2–9a) flue gases are drawn back into the flame due to the pressure difference set up by the high velocity gas stream. In figure 2–9(b) flue gas entrainment into a high velocity jet is illustrated.

Figure 2–9 Internal recirculation: (a) recirculation cup, (b) jet-flow induced (Røkke, 1994)

By the use of swirl vanes or a tangential flow entry to create a tangential velocity component of the flow, the rotation that is characteristic for a swirling flow can be generated. The degree of swirl or rotation can be described by the non-dimensional swirl number, *S*. The swirl number is defined as follows (Gupta et al., 1984):

$$S = \frac{G_\theta}{G_x r} \qquad (2–8)$$

Where G_θ is the axial flux of swirl (angular) momentum, G_x is the axial flux of axial momentum and r is a characteristic radius such as the burner radius or the swirler radius. When the swirl number exceeds the critical value of 0.6, the flow possess sufficient radial and axial pressure gradients to cause flow reversal and a central toroidal recirculation zone (CTRZ) can be observed (Gupta et al., 1984). The recirculation of hot combustion gases into the CTRZ close to the burner throat will ensure continuous ignition of the colder unburned combustion gases and a reduction of the NO_x formation by reduced flame temperatures and by reduction of the O_2 partial pressure. Typical profiles of axial and swirl (tangential) velocity components for a strong swirling flow are shown in figure 2–10. The subject of swirling flows are thoroughly reviewed in the textbook by Gupta et al. (1984) which can be recommended for a further in-depth study of swirling flows.
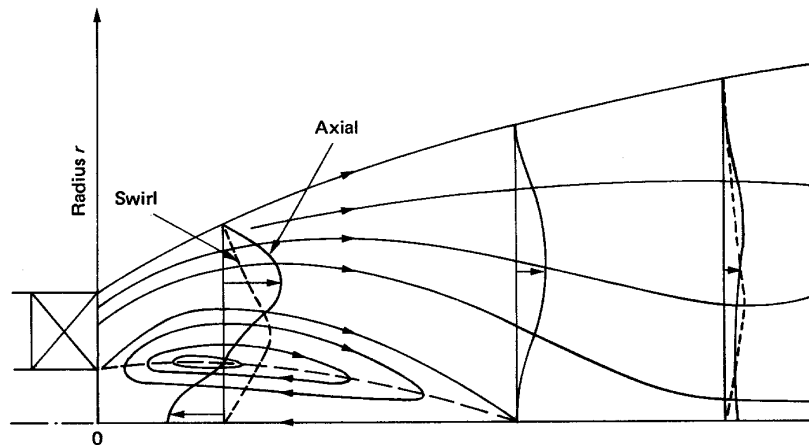
Figure 2–10 Flow recirculation in a strong swirling flow (Lefebvre, 1983).

A technique to reduce combustion temperatures and hence the amount of NO_x formated via the thermal NO mechanism is to increase the heat transported away from the combustion. Burners with enhanced heat transfer are described by Zepter (2003). By using a porous inert media (PIM) insert in the burner where the reaction takes place, the heat transfer by radiation and conduction from the burner to the surroundings is increased. Zepter (2003) measured NO_x emissions in the range 5-20 ppm at combustion temperatures below 1327 K (1600 °C) using the PIM-burner shown in figure 2–11. Premixed air and fuel enters the PIM-burner from below, where a porous material with a smaller pore size is used for the inlet region to avoid flashback. A drawback with the PIM-burner which is a lean premix burner, is the high excess air ratio used ($\lambda = 1.3 - 1.6$) which will lead to increased flue gas losses and reduced boiler efficiency. According to Zepter (2003), the temperatures can be kept low by using external flue gas recirculation for dilution instead of air to keep the temperatures low. This will also reduce the NO_x formation via the prompt NO mechanism since increased concentrations of H_2O and CO_2 will increase the consumption of CH present (Zepter, 2003).

The PIM-burner can also be used in conjunction with a catalytic material in the inlet region as described by Rørtveit et al. (2002). In catalytic combustion, fuel and air are oxidized on the catalyst surface through a sequence of low activation energy reactions. The reactions can then take place at lower temperatures than in homogenous combustion. The surface reactions that take place on the catalyst do not produce NO, hence the NO_x emissions from catalytic combustion can be as low as 1 ppm (Warnatz et al., 1999 p. 251-252). A disadvantage with catalytic combustion is that the active surface (usually Pt or Pd) must be kept at low temperatures to avoid oxidation and vaporization. This can be achieved by using high excess air ratios and enhancing the heat transfer from the burner. The catalytically supported PIM (CSPIM) burner described by Rørtveit et al. (2002) combines catalytic combustion with the enhanced heat transfer achieved in the PIM burner by using a catalytic material in the inlet region of the burner (figure 2–11). The heat released by the catalytic combustion ignites the remaining reactants in the PIM, which are diluted by products from the catalytic combustion (Zepter, 2003).
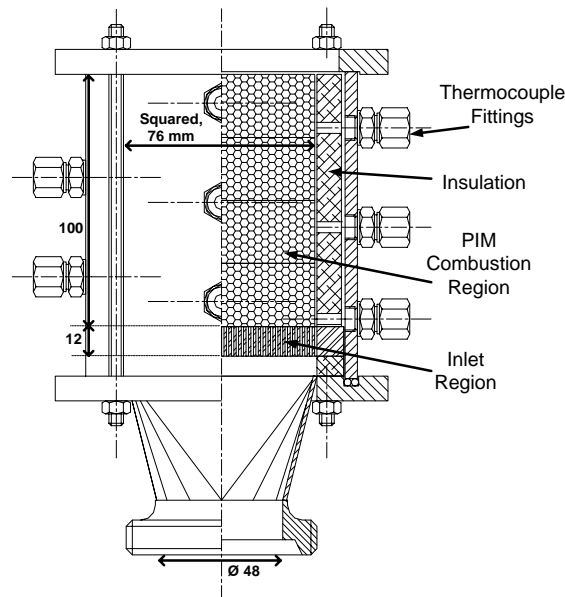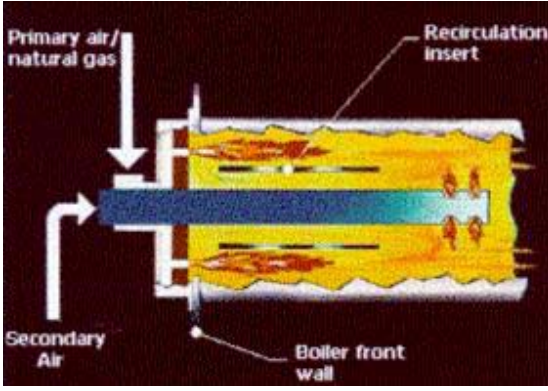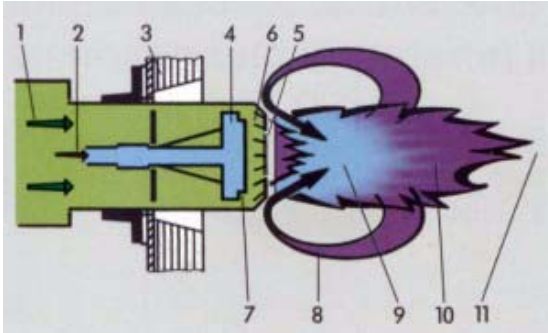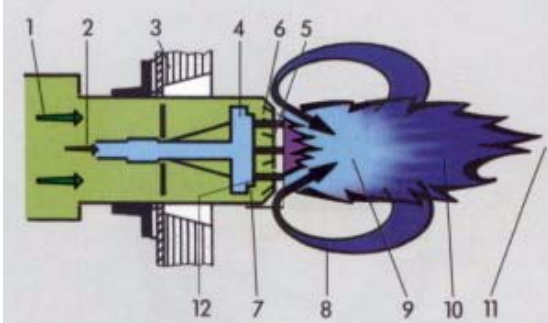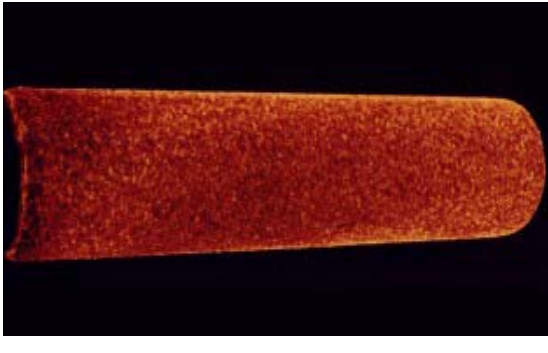
Figure 2–11 PIM burner (Zepter, 2003).

2.2.5 Low NO$_x$ burners

Low NO$_x$ burner design differs depending on the size and application of the burner. The complexity of the burner design tends to increase with increasing size. In smaller units such as domestic heaters and boilers (< 100 kW), the burner design is kept simple and the burners are typically based on premixing to achieve low NO$_x$ emissions. In large combustion plants (> 50 MW), the burners installed are much more complex in design and a combination of various NO$_x$ reduction techniques such as staged combustion, partial premixing, external and internal flue gas recirculation, are applied to keep the NO$_x$ emissions low. External flue gas recirculation which is very efficient in reducing formation of NO$_x$ requires additional installation of heat resistant pipes and fans which considerably increases investment costs and operating costs of the burner installation.
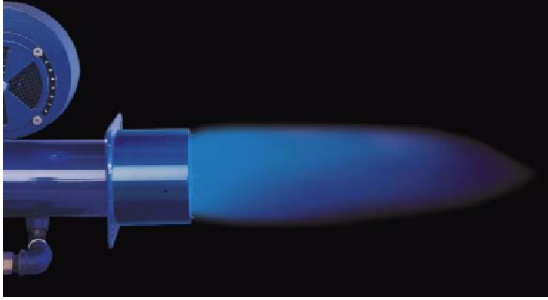
For medium to large burners (0.1 - 10 MW) the geometry might be complex, but external FGR is often avoided due to the additional costs. It is also common that burners in this range used for boilers and heat exchangers are equipped with an air blowing fan. By avoiding external FGR, the burners are made more attractive for retrofit into old boiler installations where NO$_x$ emissions must be reduced to meet new regulations. To illustrate the use of various NO$_x$ reduction techniques in this kind of burners, some commercially available low NO$_x$ burner concepts for natural gas, and the NO$_x$ reduction technique applied, are summarized in table 2–4. The burners and manufacturers presented represent only a small selection of available concepts and are chosen for the sake of illustration only. The burner concepts in table 2–4 should not by any means be considered as the author's recommendation for any low NO$_x$ burner installations. The ceramic and metallic porous mesh burners shown are equipped with an additional combustion air filter on the fan inlet.

Table 2–4 Various commercially available low NO_x fan burners for natural gas.

	Description
	Johnston Boiler and GTI: FIR Burner • Premixed • Staged Air • Internal FGR • Interstage heat removal • NO_x emission < 10 ppm • Turn down ratio: 1:4 • Capacity: 0.5 - 10 MW • Fuel pressure: 0.345 bar http://www.johnstonboiler.com/
	Walter Dreizler GmbH: ARZ burner • Internal FGR (8) • 2 combustion zones (7 and 9) • NO_x emission < 40 ppm (80 mg/kWh) • Turn down ratio: 1:10 • Capacity: 0.025 - 15 MW http://www.dreizler.com/
	Walter Dreizler GmbH: ARZ Super burner • Internal FGR (8) • 2 combustion zones (7 and 9) • Additional fuel staging (12) • NO_x emission < 30 ppm (60 mg/kWh) • Turn down ratio: 1:10 • Capacity: 0.025 - 15 MW http://www.dreizler.com/
	Walter Dreizler GmbH: MAGMA burner • Enhanced radiative heat transfer by use of ceramic burner (infrared-combustion) • Surface temperature of 700 to 900 °C. • NO_x emission 5 - 18 ppm (10 - 35 mg/kWh) • Capacity: 0.01 - 5 MW http://www.dreizler.com/

Table 2–4 Various commercially available low NO$_x$ fan burners for natural gas.

	Power Flame: NOVA Plus burner • Premixed • Enhanced radiative heat transfer by use of metallic porous mesh burner head • Flame stabilized on surface of porous mesh • NO$_x$ emission < 9 ppm • Capacity: 0.6 - 4.3 MW • Fuel supply pressure: 0.045 - 0.070 bar http://www.powerflame.com/
	Power Flame: NOVA premix burner • Premixed • Swirl stabilized flame • NO$_x$ emission < 30 ppm • Further reduction of NO$_x$ (< 20 ppm) by increasing excess air • Capacity: 120 - 650 kW • Fuel supply pressure: 0.017 - 0.029 bar http://www.powerflame.com/

2.3   Scaling of burners

2.3.1   Introduction

When developing low NO$_x$ burners, experiments are usually carried out on laboratory scale burners, and scaling criteria are therefore needed to apply the results to an industrial scale. A correlation for scaling of NO$_x$ emissions from buoyancy-dominated hydrocarbon diffusion flames has been presented by Røkke et al. (1992):

$$EI_{NOx}\rho_0 u_0 / d_0 \approx 44 Fr^{3/5} \approx 11 u_0^{1.2} / d_0^{0.6} \tag{2–9}$$

Where EI_{NOx} is the emission index of NO$_x$ in grams per kg fuel, represented as NO$_2$ by assuming all NO are reacted to NO$_2$. ρ_0, u_0 and d_0 are the fuel density, average velocity at the exit and exit diameter respectively. The agreement between experimental results and the correlation in equation (2–9) was found to be much better than a factor of two, which was the best accuracy claimed from the derivation of the correlation (Røkke et al., 1992). The correlation was expanded by Weber (1996) to make it applicable for various heat extractions from the flame, which then made it possible to apply the NO$_x$-scaling to flames in furnaces. Al-Fawaz et al. (1994) applied the NO$_x$-scaling correlation for an industrial burner without any corrections for furnace conditions. They adopted an equivalent-area-diameter single-jet similarity for the fuel nozzles to calculate the Froude number (*Fr*) in equation (2–9). The correlation for diffusion flames in equation (2–9) was further developed by Røkke et al. (1994) for partially premixed flames. The following correlation takes the fuel mass fraction (Y_f) in the fuel supply into consideration as well when scaling the emissions of NO$_x$ from partially premixed flames:

$$EI_{NOx}\rho_0 u_0 / d_0^{0.55} = 8 Fr^{3/5} Y_f^{-1/5} \tag{2–10}$$

The correlations presented by Røkke et al. (1992, 1994) were derived for buoyant diffusion flames and, as mentioned, they have been applied to some industrial burners.

For scaling of a laboratory burner prototype, scaling criteria must be considered. A scaling based on keeping the dimensionless numbers such as the Reynolds, Froude or Damkhöler numbers constant leads to conflicting requirements (Weber, 1996), and only a few of the scaling rules are obeyed in practice, leading to a so-called partial scaling. The most frequently applied criteria for scaling of industrial burners are the constant velocity and the constant residence time approaches, while the constant Reynolds number criteria seldom is used due to industrial burners typically operate at Reynolds number higher than 10^5 (Weber, 1996).

An elaborate study of industrial burner scaling called the "Scaling 400 project", has been carried out at the IFRF (Weber, 1996). Five furnaces with thermal input in the range from 30 kW to 12 MW were investigated. The constant velocity scaling principle combined with the geometrical and thermal similarities were applied when designing the burners used experimentally in this study (Bollettini at al., 2000). The constant residence time criterion was investigated in the same study by mathematical modelling (Bollettini at al., 2000). According to Weber (1996), the primary conclusions from the "Scaling 400 project" were that to achieve the burner flow pattern similarity, the fuel-to-air momentum had to be maintained, the geometrical similarities should be maintained and the effect of the confinement (ratio of furnace diameter to burner throat diameter) was secondary for confinements larger than 3. The heat extraction in the furnace should also be similar, and in the "Scaling 400 project" thermal similarity was obtained by having identical furnace exit temperatures (Bollettini et al., 2000).

2.3.2 Constant velocity scaling

The burner thermal input (Q) can be expressed by the following equation:

$$Q = K\rho_0 u_0 d_0^2 \qquad (2\text{--}11)$$

Where ρ_0, u_0 and d_0 are the burner exit fluid density, the characteristic burner exit velocity and the characteristic burner exit diameter. K is a proportionality constant. The constant velocity scaling criteria is based on maintaining the combustion air and fuel velocities constant when scaling a burner to a different thermal input. By introducing u_0 as a constant in equation (2–11), the characteristic diameter can be evaluated as (Bollettini et al., 2000):

$$d_{scal} = d_0 \left(\frac{Q_{scal}}{Q_0} \right)^{0.5} \qquad (2\text{--}12)$$

All other geometrical burner dimensions can now be calculated from the characteristic diameter since the geometrical similarity is maintained.

2.3.3 Constant residence time scaling

The principle of the constant residence time scaling criterion is to maintain the d_0/u_0 ratio constant while changing the burner thermal input (Bollettini et al., 2000). The d_0/u_0 ratio represents the inertial time scale of the flow, often called the convective time scale. At high Reynolds numbers, all time measures in the flow, except those associated with the final molecular dissipation processes, are proportional to this ratio (Weber, 1996). Intro-

ducing this ratio into equation (2–11) in a similar way as for the constant velocity scaling criteria, the characteristic burner diameter can now be evaluated as follows:

$$d_{scal} = d_0 \left(\frac{Q_{scal}}{Q_0} \right)^{0.33} \qquad (2\text{–}13)$$

As for the constant velocity scaling criteria, all burner dimensions can be calculated from this characteristic burner diameter. The constant residence time approach is seldom used by burner manufacturers because it leads to very low windbox pressures for small-scale burners and excessive pressures for full-scale burners (Weber, 1996).

2.4 Non-intrusive measurement techniques using laser

2.4.1 Background

Developments in laser technology have resulted in a whole range of new opportunities in combustion research. Laser based measurement techniques have the advantage, over traditional probing techniques, of being non-intrusive. When investigating in hostile or delicate combustion environments, a physical probe can disturb the very process under investigation and lead to quite significant inaccuracies. Laser techniques on the other hand, do not affect the flow field or influence the chemical reactions in the domain being investigated. In addition to this, laser light can be focused to a high spatial and temporal resolution. Another drawback of physical probing is the material limitations of the probe which can be break down due to the high temperatures in the measurement area.

However, complications are associated with the use of laser techniques as well. No matter how sophisticated the laser being used, it is useless without a proper optical access to the test volume. This can be a practical challenge if the test volume is enclosed in an engine cylinder or a combustion chamber. Design of the test rig must therefore be dedicated to provide good optical access for laser beams and signal collection for the particular experiment to succeed.

The principles behind laser technology can be found described in most physics textbooks such as Serway (1996). The word *laser* is an acronym for Light Amplification by Stimulated Emission of Radiation. An atom has more than one allowed energy states, often labelled E_1, E_2 and E_3 and so on. At ordinary temperatures, most atoms in a sample are in the ground state, E_1. When light is incident on an atom, the photons whose energy hf matches the energy difference ΔE between two energy levels, can be absorbed by the atom (h - Planck's constant, f - frequency of the photon). By this process called stimulated absorption, the atom is exited to a higher energy level. In figure 2–12(a), stimulated absorption of a photon of energy $hf = E_2 - E_1$ by an atom, is illustrated. There is a certain probability that an excited atom will return to its ground state, a process in which a new photon will be emitted. This is called spontaneous emission and is illustrated in the energy level diagram in figure 2–12(b). An atom exists in the exited state for a very short period of time (typically about 10^{-8} s). If a photon is incident on an atom that already is in an excited state, the incoming photon increases the probability that the atom will return to its ground state while emitting a second photon. This is called stimulated emission, an important process in lasers, and is illustrated in figure 2–12(c). For stimulated emission to occur, the atom must be in a metastable excited state having a lifetime longer than 10^{-8} s. The incident photon and the emitted photon in stimulated emission are in phase with each other, and both photons can in turn stimulate other atoms in the excited state to emit pho-

tons in a chain of similar processes. The photons produced in such a chain reaction of stimulated emissions are the source of the intense, coherent light in a laser.
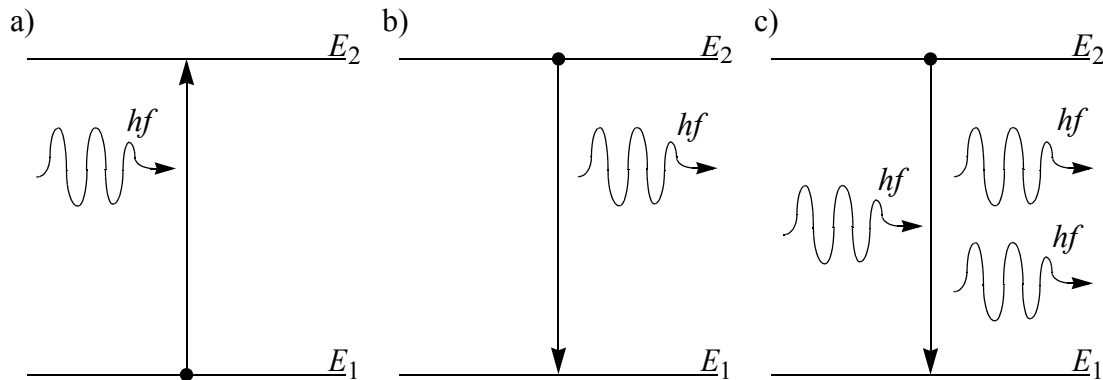
Figure 2–12 Energy level diagrams showing (a) stimulated absorption of a photon; (b) spontaneous emission of a photon; (c) stimulated emission of a photon by another incoming photon.

2.4.2 The Nd:YAG laser

A commonly used laser source in combustion research is the Nd:YAG laser (Daily, 1997). In this laser, lasing occurs in trivalent neodymium ions, Nd^{3+} housed in a yttrium aluminium garnet ($Y_3Al_5O_{12}$) crystalline host material (Eckbreth, 1996 p 113). Excitation is provided by a flashlamp or a diode laser, but most common in high energy applications is the flashlamp, due to the price and power of the diode lasers.

In the YAG host, the lasing occurs in the Nd ions which are four level systems. An energy diagram for such a four level system is shown in figure 2–13. An Nd ion is pumped to the upper energy level E_4 from the ground state E_1, by a photon with frequency f_1 from a flashlamp or a diode laser. E_4 is unstable, and the ion will almost instantaneously drop to a lower energy level. For Nd ions, the probability of the E_4 to E_3 transition is greater than the E_4 to E_1 transition. Since E_3 is a metastable state, the population of the E_3 state will increase. A new photon of frequency f_2 is emitted from the Nd ion during the E_3 to E_2 transition. Because E_2 is unstable as well, the ions in this state will quickly decay to the ground state, E_1. The emitted photon of frequency f_2 from the Nd ion will now stimulate neighbouring Nd ions in the metastable state E_3, resulting in the production of coherent light at a wavelength of 1064 nm.
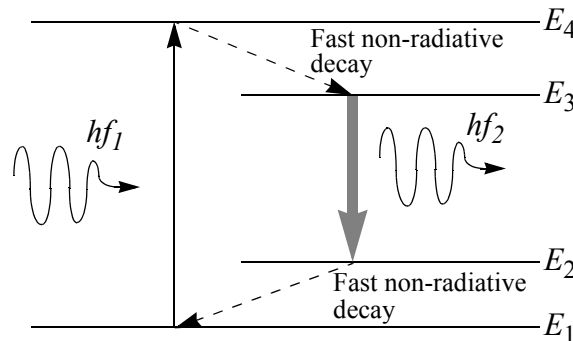
Figure 2–13 Four-level energy diagram used by the Nd:YAG laser. The 1064 nm laser light arise from the photons emitted by the transition E_3 to E_2.

2.4.3 Laser Induced Fluorescence

Laser Induced Fluorescence (LIF) is a laser technique that can be used in combustion diagnostics for measurements of species concentrations and temperatures. Combustion species concentrations can be measured on a ppmv or even sub-ppmv basis. Species that are detected using LIF consists of about 30 various combinations of O, N, H, C and S (Eckbreth, 1996). This measurement method has been the subject of extensive research and in the reviews by Kohse-Höinghaus (1994) and Daily (1997) comprehensive compilations on the LIF technique are given. A thorough investigation of this topic can also be found in the textbook by Eckbreth (1996).

Fluorescence is understood as an absorption process followed by light emission (Kohse-Höinghaus, 1994). In LIF, the atoms or molecules under investigation are excited to an upper energy level by incident laser radiation (Daily, 1997). The intensity of the resulting fluorescence provides information on the concentration of the emitting species (Kohse-Höinghaus, 1994).

The four level energy diagram in figure 2–14 summarizes the various transitions in an OH radical. By absorption of a photon of suitable energy, an excited energy level is populated, and light is emitted at the same and different wavelengths depending on the energy level decay path of the excited radical. Spontaneous emission competes with stimulated emission and collision processes (Kohse-Höinghaus, 1994). In figure 2–14 the upward arrow (1) represents the excitation in the (1,0) transition of the A-X system by the absorption of a suitable photon. The relevant depopulation processes are represented by the downward arrows. The same photons that excites the radical in the first place, can also result in stimulated emission and decay to the ground state again (2).

Transitions between rotational energy levels (light lines) are indicated by bidirectional arrows (3) while transitions between vibrational energy levels (heavy lines) are shown by the short arrows (4). Electronic quenching is represented by the long arrow (5). Rotational and vibrational energy transfer and electronic quenching arise when the internal energy of the system is altered through inelastic molecular collisions referred to as quenching. Transitions from an upper electronic state to a new set of energy levels via spontaneous emission are represented by the hatched arrows (6). The transition to a lower energy level which is not involved in the initial absorption process produces a new photon with a different wavelength than the first photon produced by the stimulated emission. This will reduce the interference between the incident laser light and the fluorescence detected for the OH concentration measurements.

For detection of radicals using LIF, a prerequisite is that the radical has a known absorption and emission spectrum, and that this spectrum is in a wavelength range conveniently accessible by a tunable laser (Kohse-Höinghaus, 1994). The OH radical fits into these requirements, and a large number of combustion studies have been reported with OH LIF. There is a wide range of work reported on the OH radical, a large database is available on its collisional behaviour, and the OH spectroscopy is well known. LIF measurements of the OH radical are therefore somewhat easier achieved than for most other combustion radicals (Kohse-Höinghaus, 1994). In hydrocarbon oxidation, the OH radical is an important intermediate and in most flames it is present in relatively large concentrations. OH LIF measurement has therefore become an important and popular technique in combustion studies. Formation of OH radicals takes place in the flame front, and OH is found both there and in the hot burnt gases due to equilibrium reactions (Arnold et al., 1997). The OH radical is together with the CH radical a typical marker of the flame front (Bombach and Käppeli, 1999).
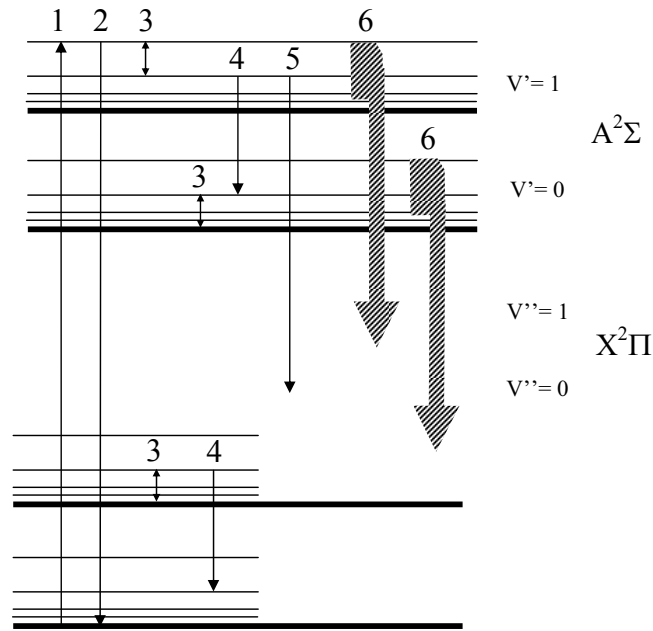
Figure 2–14 Energy level diagram for the OH radical.

2.5 Computational fluid dynamics

2.5.1 Governing equations of fluid flow and heat transfer

To solve a fluid flow problem using Computational Fluid Dynamics (CFD), a set of mathematical equations are solved. These are conservation equations for mass, species mass, momentum and energy. In this section these mathematical descriptions of fluid flow will be presented briefly. A more complete introduction into this topic can be found in most CFD textbooks, such as the book by Ferziger and Peric (2002).

Conservation of mass

In fluid mechanics, a basic principle is that mass can neither be created nor destroyed. This principle can be used to derive the continuity equation for a small element of volume $V = dxdydz$ (figure 2–15). In the x-direction the rate of mass flow from the left hand side is given by:

$$\dot{m}_x = \rho u_x dydz \tag{2–14}$$

If both the velocity (u_x) and the density (ρ) changes in the x-direction, by using Taylor's theorem, the mass flow out of the volume on the right hand side will be:

$$\dot{m}_{x+dx} = \left[\rho u_x + \frac{\partial(\rho u_x)}{\partial x} dx \right] dydz \tag{2–15}$$
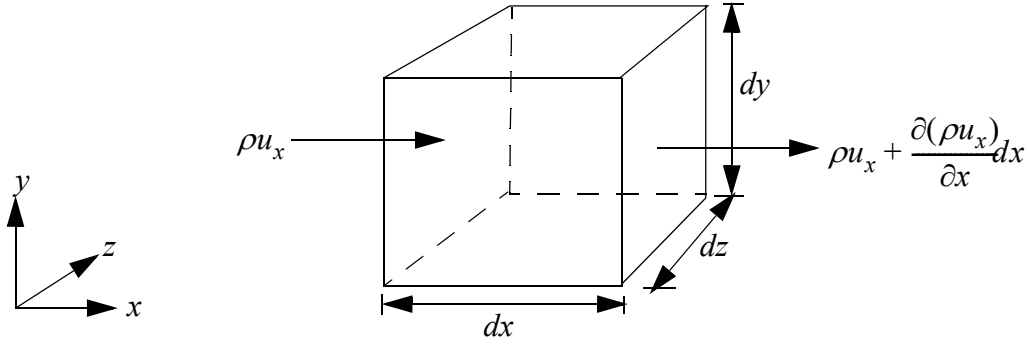
Figure 2–15 Small element of volume V = dxdydz.

By subtracting equation (2–14) from equation (2–15), the net rate of mass flow from the volume in the x-direction can be expressed by equation (2–16):

$$\Delta \dot{m}_x = \left[\frac{\partial(\rho u_x)}{\partial x} \right] dx dy dz \qquad (2\text{–}16)$$

Similarly, it can be found for the y- and z-directions:

$$\Delta \dot{m}_y = \left[\frac{\partial(\rho u_y)}{\partial y} \right] dx dy dz \qquad (2\text{–}17)$$

$$\Delta \dot{m}_z = \left[\frac{\partial(\rho u_z)}{\partial z} \right] dx dy dz \qquad (2\text{–}18)$$

Where u_y and u_z is the velocity in y- and z-direction, respectively. The net mass flow out of the control volume is now given by summing up equation (2–16), (2–17) and (2–18):

$$\Delta \dot{m}_{net} = \left[\frac{\partial(\rho u_x)}{\partial x} + \frac{\partial(\rho u_y)}{\partial y} + \frac{\partial(\rho u_z)}{\partial z} \right] dx dy dz \qquad (2\text{–}19)$$

The time rate of mass increase inside the volume is given by:

$$\Delta \dot{m}_{net} = -\frac{\partial \rho}{\partial t} dx dy dz \qquad (2\text{–}20)$$

Equating equation (2–19) and (2–20) gives the differential form of the continuity equation:

$$\frac{\partial(\rho u_x)}{\partial x} + \frac{\partial(\rho u_y)}{\partial y} + \frac{\partial(\rho u_z)}{\partial z} = -\frac{\partial \rho}{\partial t} \tag{2–21}$$

In the case of steady flow, $\frac{\partial \rho}{\partial t} = 0$ and because $\frac{\partial(\rho u_x)}{\partial x} = \rho \frac{\partial u_x}{\partial x} + u_x \frac{\partial \rho}{\partial x}$, equation (2–21) can be rewritten as follows:

$$u_x \frac{\partial \rho}{\partial x} + u_y \frac{\partial \rho}{\partial y} + u_z \frac{\partial \rho}{\partial z} + \rho\left(\frac{\partial u_x}{\partial x} + \frac{\partial u_y}{\partial y} + \frac{\partial u_z}{\partial z}\right) = 0 \tag{2–22}$$

If the flow is incompressible, i.e. the density is constant, the continuity equation becomes:

$$\frac{\partial u_x}{\partial x} + \frac{\partial u_y}{\partial y} + \frac{\partial u_z}{dz} = 0 \tag{2–23}$$

Which can be written in vector form:

$$\frac{\partial u_i}{\partial x_i} = 0 \tag{2–24}$$

Conservation of species mass

For flows where the fluid consists of a number of chemical species in the same phase, a continuity equation can be written for each of them. For each chemical species n of local mass fraction Y_n the following equation is solved:

$$\frac{\partial}{\partial t}(\rho Y_n) + \frac{\partial}{\partial x_i}(\rho u_i Y_n) = -\frac{\partial J_{n,i}}{\partial x_i} + R_n \tag{2–25}$$

Where R_n is the production rate of species n by chemical reaction and $J_{n,i}$ is the diffusion flux of species n which arises due to gradients in the species concentration. In laminar flows $J_{n,i}$ can be solved by using Fick's law:

$$-J_{n,i} = \rho D_n \frac{\partial Y_n}{\partial x_i} \tag{2–26}$$

Where D_n is the diffusion coefficient for species n in the mixture.

Conservation of momentum

Conservation of momentum is a result of Newton's second law, stating that "The net force acting on a body is equal to the rate of change of momentum of the body". The momentum equation for an incompressible fluid in the i direction can be written as follows:

$$\frac{\partial}{\partial t}(\rho u_i) + \frac{\partial}{\partial x_j}(\rho u_i u_j) = -\frac{\partial p}{\partial x_i} + \frac{\partial \tau_{ij}}{\partial x_j} + \rho g_i + F_i \qquad (2\text{–}27)$$

Where p is the static pressure, ρg_i is the gravitational body force in the i direction, F_i is the external body force in the i direction and τ_{ij} is the stress tensor given by equation (2–28).

$$\tau_{ij} = \mu\left(\frac{\partial u_i}{\partial x_j} + \frac{\partial u_j}{\partial x_i}\right) - \frac{2}{3}\mu\frac{\partial u_k}{\partial x_k}\delta_{ij} \qquad (2\text{–}28)$$

Where μ is the molecular viscosity.

Equation (2–27) and equation (2–28) are often referred to as the Navier-Stokes equation of the conservation of momentum.

Conservation of energy

The conservation of energy can be described by equation (2–29).

$$\frac{\partial}{\partial t}(\rho E) + \frac{\partial}{\partial x_i}(u_i(\rho E + p)) = \frac{\partial}{\partial x_i}\left(k_{eff}\frac{\partial T}{\partial x_i} - \sum_k h_n J_n + u_j(\tau_{ij})_{eff}\right) + S_h \qquad (2\text{–}29)$$

Where k_{eff} is the effective conductivity, $k_{eff} = k + k_t$, the sum of conductivity (k) and turbulent conductivity (k_t) of the fluid. J_n is the diffusion of species n, $(\tau_{ij})_{eff}$ is the effective stress tensor defined in the same way as the effective conductivity. The first three terms on the right hand side of equation (2–29) represent energy transfer due to conduction, species diffusion and viscous dissipation. S_h includes the heat of chemical reaction and any other heat sources present. For the energy, E:

$$E = h - \frac{p}{\rho} + \frac{u_i^2}{2} \qquad (2\text{–}30)$$

Where the enthalpy *(h)* is defined for an ideal gas as:

$$h = \sum_n Y_n h_n \qquad (2\text{–}31)$$

In equation (2–31) Y_n is the mass fraction of species n, and h_n is given by:

$$h_n = \int_{T_{ref}}^{T} c_{p,k} dt \tag{2–32}$$

In equation (2–32) T_{ref} is 298.15 K.

2.5.2 Computation of turbulent flow

Turbulence is an extremely complex subject, which will be described only briefly in this thesis. Some basic background on how turbulent flow can be described mathematically will be given together with a description of the turbulence models that will be used in this thesis. For a further in-depth study of turbulent flows and modelling of turbulent flows, the textbooks by Mathieu and Scott (2000), Ferziger and Peric (2002) or the recent review by Hanjalic (2002) can be recommended, also the textbook by Peters (2000) and the reviews by Spalding (1976), Correa and Shyy (1987) and Borghi (1988), which specifically treats the subject of turbulent flow with combustion, can be recommended.

Turbulent flow can be characterised as highly unsteady with fluctuating and apparently random velocity fields that has a wide range of different length and time scales. Turbulence ensures mixing of the conserved quantities such as momentum, energy and species concentrations through the flow field. The instantaneous turbulent flow can be described exactly by the unsteady Navier-Stokes conservation equations of continuity, momentum and energy (equation (2–21), equation (2–27) and equation (2–29) respectively). However, a Direct Numerical Simulation (DNS) of most applications is too computational demanding to be feasible using the computer technology available today. Therefore, instead of solving for the exact fluid flow, overall turbulence features can be modelled by treating it as a random process and adopting averaging techniques to account for deviations from mean values.

Reynolds Averaged Navier-Stokes (RANS)

Fluid properties (ϕ) of a turbulent flow such as velocity, pressure, energy or species concentration, can be decomposed into mean ($\bar{\phi}$) and fluctuating (ϕ') components:

$$\phi_i = \bar{\phi}_i + \phi_i' \tag{2–33}$$

By assuming the time averaged density to be constant and substituting equation (2–33) for the velocity (u_i) into equation (2–21) and equation (2–27), the continuity and the momentum equation respectively, the Reynolds Averaged Navier-Stokes (RANS) equations can be found:

$$\frac{\partial \rho}{\partial t} + \frac{\partial}{\partial x_i}(\rho \bar{u}_i) = 0 \tag{2–34}$$

$$\frac{\partial}{\partial t}(\rho \bar{u}_i) + \frac{\partial}{\partial x_j}(\rho \bar{u}_i \bar{u}_j) = -\frac{\partial \bar{p}}{\partial x_i} + \frac{\partial}{\partial x_j}(\bar{\tau}_{ij} - \rho \overline{u_i' u_j'}) \tag{2–35}$$

In cases with large density variations, such as in turbulent combustion, density-weighted averaging, or Favre averaging, are often used instead of time averaging (Warnatz, 1999).

Apart from the velocities being represented by averages and the last term on the right hand side of equation (2–35), the Reynolds Stress term $(-\rho\overline{u_i'u_j'})$, equation (2–34) and equation (2–35) can be seen to have a noticeable similarity with equation (2–21) and equation (2–27). When solving the RANS equations the Reynolds Stress term, which arise as a result of turbulence, causes a problem because the number of unknowns are now being higher than the number of equations to solve. This problem is known as the closure problem and can only be resolved by adopting some kind of model to represent the Reynolds stresses.

In CFD, there are two basic levels of modelling currently used (Hanjalic, 2002). The first are Eddy Viscosity/Diffusivity Models, also known as first-order models. Then there are Second-Moment Closure Models, also known as Reynolds stress or second-order models. There are numerous variants of these models developed for different kinds of turbulent flows, and a lot of references can be found on this topic. The review by Hanjalic (2002) and the textbooks by Mathieu and Scott (2000) and Ferziger and Peric (2002) are just a small sample of the selection available. The models that will be used in this thesis are two first-order models, namely the standard k-ε model and the RNG k-ε model and a second-order Reynolds Stress Model. These models are closer described in the following.

The Standard k-ε Model

The first-order k-ε model, first introduced by Jones and Launder (1972), is the most widely used turbulence model, especially for industrial applications, and has been implemented into most commercial CFD codes (Hanjalic, 2002). It is numerically robust and has been tested for a wide range of turbulent flows. The Eddy Viscosity/Diffusivity Models, including the k-ε model, are based on the assumption that the Reynolds Stress terms can be related to the mean velocity gradients by using a turbulent/eddy viscosity (μ_t) as in the following expression:

$$-\rho\overline{u_i'u_j'} \;=\; \mu_t\left(\frac{\partial\overline{u}_i}{\partial x_j} + \frac{\partial\overline{u}_j}{\partial x_i}\right) - \frac{2}{3}\left(\rho k + \mu_t\frac{\partial u_i}{\partial x_i}\right)\delta_{ij} \tag{2–36}$$

Where k is the turbulent kinetic energy:

$$k \;=\; \frac{1}{2}\overline{u_i'u_i'} \tag{2–37}$$

The k-ε model solves two transport equations, one for the turbulent kinetic energy and one for its rate of dissipation, ε:

$$\rho\frac{Dk}{Dt} \;=\; \frac{\partial}{\partial x_i}\left[\left(\mu + \frac{\mu_t}{\sigma_k}\right)\frac{\partial k}{\partial x_i}\right] + G_k - \rho\varepsilon \tag{2–38}$$

$$\rho\frac{D\varepsilon}{Dt} \;=\; \frac{\partial}{\partial x_i}\left[\left(\mu + \frac{\mu_t}{\sigma_\varepsilon}\right)\frac{\partial\varepsilon}{\partial x_i}\right] + \frac{\varepsilon}{k}(C_{1\varepsilon}G_k - C_{2\varepsilon}\rho\varepsilon) \tag{2–39}$$

Where G_k represents the generation of turbulence kinetic energy due to the mean velocity gradients, $C_{1\varepsilon}$ and $C_{2\varepsilon}$ are empirically defined constants, σ_k and σ_ε are the turbulent Prandtl numbers for k and ε respectively which also are found empirically. The turbulent viscosity (μ_t) is computed from the values of k and ε as follows:

$$\mu_t = \rho C_\mu \frac{k^2}{\varepsilon} \tag{2–40}$$

Where also C_μ is an empirically defined constant. The constants used in the standard k-ε model are given by Launder and Spalding (1974) and can be found quoted in table 2–5.

Table 2–5 Constants in the k-ε model (Launder and Spalding, 1974).

C_μ	$C_{1\varepsilon}$	$C_{2\varepsilon}$	σ_k	σ_ε
0.09	1.44	1.92	1.0	1.3

The robustness and economy of use of the k-ε model make it an attractive tool in CFD, but for some flows the k-ε model does not perform satisfactory. The fact that turbulence is treated as isotropic makes it not suitable for complex flows such as swirling and rotating flows, flows with strong streamline curvature, flows in rotational systems or flows with three-dimensionally effect such as strong cross flows (Hanjalic, 2002). Despite these shortcomings, the k-ε model gives reasonably realistic results for the mean flow in most cases, and can in any case give a quick preliminary estimation for the flow field.

The RNG k-ε Model

Many of the limitations of the standard k-ε model for complex turbulent flows can be overcome without sacrificing its robustness and efficiency by applying the RNG-based k-ε model proposed by Yakhot et al. (1992). The RNG k-ε model is derived from the instantaneous Navier-Stokes equations, using a mathematical technique called "renormalization group" (RNG) methods. The model assumes that at small eddies, the length scales are approximated by the Kolmogorov energy spectrum. The model constants can then be determined directly from the renormalization analysis instead of empirical as in the standard k-ε model (Jaw and Chen, 1998). The analytical derivation also results in some additional terms and functions in the transport equations for k and ε compared with the standard k-ε model. The model and its constants will be presented in the following, but a more comprehensive description of RNG theory and its application to complex turbulent flow can be found in Choudhury (1993).

As the standard k-ε model, the RNG k-ε model consists of two transport equations to be solved for k and ε:

$$\rho \frac{Dk}{Dt} = \frac{\partial}{\partial x_i}\left[\alpha_k \mu_{eff} \frac{\partial k}{\partial x_i}\right] + G_k - \rho\varepsilon \tag{2–41}$$

$$\rho \frac{D\varepsilon}{Dt} = \frac{\partial}{\partial x_i}\left[\alpha_\varepsilon \mu_{eff} \frac{\partial \varepsilon}{\partial x_i}\right] + \frac{\varepsilon}{k}(C_{1\varepsilon}G_k - C_{2\varepsilon}\rho\varepsilon) - R_\varepsilon \tag{2–42}$$

Where α_k and α_ε are the inverse effective Prandtl numbers for k and ε, computed by the following equation:

$$\left|\frac{\alpha - 1.3929}{-0.3929}\right|^{0.6321}\left|\frac{\alpha + 2.3929}{3.3929}\right|^{0.3679} = \frac{\mu}{\mu_{eff}} \tag{2–43}$$

The effective viscosity (μ_{eff}) is a combination of the molecular viscosity (μ) and the turbulent viscosity (μ_t):

$$\mu_{eff} = \mu + \mu_t \tag{2–44}$$

The turbulent viscosity is calculated by equation (2–40) as in the standard k-ε model.

The main difference between the RNG and the standard k-ε models, lies in the additional term for rate of strain in the ε-equation, R_ε, given by:

$$R_\varepsilon = \frac{C_\mu \rho \eta^3 (1 - \eta/\eta_0) \varepsilon^2}{1 + \beta \eta^3}\frac{\varepsilon^2}{k} \tag{2–45}$$

$$\eta = Sk/\varepsilon \tag{2–46}$$

Where $\eta_0 = 4.38$ and $\beta = 0.012$ and S is defined by:

$$S = (2S_{ij}S_{ij})^{1/2} \tag{2–47}$$

The mean strain, S_{ij}, is found by:

$$S_{ij} = 1/2\left(\frac{\partial \bar{u}_i}{\partial x_j} + \frac{\partial \bar{u}_j}{\partial x_i}\right) \tag{2–48}$$

The RNG k-ε model used here has the option to account for the effects of swirl or rotation in the flow by modifying the turbulent viscosity (Fluent Inc., 2003). This modification takes the following functional form:

$$\mu_t = \mu_{t0}f\left(\alpha_s, \Omega, \frac{k}{\varepsilon}\right) \tag{2–49}$$

Where μ_{t0} is the is the turbulent viscosity calculated without the swirl modification using equation (2–40), Ω is a characteristic swirl number evaluated within the CFD code (Fluent

Inc., 2003) and α_s is a swirl constant that assumes different values depending whether the flow is swirl-dominated or only mildly swirling.

The constants used in the RNG k-ε model, which is analytically derived using the renormalization group theory (Yakhot et al. 1992), are quoted in table 2–6.

Table 2–6 Constants in the RNG k-e model (Yakhot et al., 1992).

C_μ	C_1	C_2	η_0	β
0.0845	1.42	1.68	4.38	0.012

The Reynolds Stress Model

A main weakness of two equation turbulence models such as the k-ε model is the treatment of turbulence as being isotropic (Hanjalic, 2002). This assumption is shown inappropriate for flow with significant mean rates of strain (Durbin and Speziale, 1991) which is present i.a. in flows with streamline curvature, flow skewing or rotation. The Reynolds stress model (RSM), first proposed by Launder et al. (1975), on the other hand, is a more elaborate turbulence model which does not consider the turbulence as being isotropic. The RSM involves calculation of each of the individual Reynolds stresses, $\rho \overline{u_i' u_j'}$, using differential transport equations.

An abbreviated form of the exact transport equations for the Reynolds stresses is presented in equation (2–50).

$$\frac{D(\overline{u_i' u_j'})}{Dt} = P_{ij} + D_{ij} + \varepsilon_{ij} + \Pi_{ij} + \Omega_{ij} \qquad (2\text{–}50)$$

In equation (2–50) P_{ij} represents the production term, D_{ij} the diffusion term, ε_{ij} the dissipation term, Π_{ij} the turbulence pressure-strain interaction term and Ω_{ij} the rotational term. A full description of the right hand side terms in equation (2–50) can among others be found in Launder et al. (1975), Launder (1989), Jones (1994) or Hanjalic (2002). Of the terms on the right hand side in equation (2–50), D_{ij}, ε_{ij} and Π_{ij} cannot be solved directly and have to be modelled to close these equations.

The diffusion term, D_{ij}, can be divided into molecular diffusion, $D_{ij,L}$, which can be solved without modelling, and turbulent diffusion, $D_{ij,T}$, which is modelled by applying equation (2–51):

$$D_{ij,T} = \frac{\partial}{\partial x_k}\left(\frac{\mu_t}{\sigma_k}\frac{\partial \overline{u_i' u_j'}}{\partial x_k}\right) \qquad (2\text{–}51)$$

Where the turbulent viscosity (μ_t) is defined by equation (2–40) and the turbulent prandtl number for k is set to 1.

The dissipation term (ε_{ij}) is modelled by the following expression:

$$\varepsilon_{ij} = \frac{2}{3}\delta_{ij}\rho\varepsilon \qquad (2\text{--}52)$$

In addition to equation (2–50), the RSM solves a modelled transport equation for the turbulence dissipation rate, ε, to be used in equation (2–52). This equation is the same as in the standard k-ε model, namely equation (2–39). To solve the equation for ε, the turbulent kinetic energy, k, is modelled using equation (2–37).

The pressure-strain term (Π_{ij}) is modelled by the following decomposing:

$$\Pi_{ij} = \Pi_{ij,1} + \Pi_{ij,2} + \Pi_{ij,w} \qquad (2\text{--}53)$$

Where $\Pi_{ij,1}$ is the slow pressure-strain term, also called return-to-isotropy term, $\Pi_{ij,2}$ is called rapid pressure-strain term and $\Pi_{ij,w}$ is a wall-reflection term. The slow pressure-strain term is modelled by:

$$\Pi_{ij,1} = C_1\rho\frac{\varepsilon}{k}\left[\overline{u_i'u_j'} - \frac{2}{3}\delta_{ij}k\right] \qquad (2\text{--}54)$$

The rapid pressure-strain term, $\Pi_{ij,2}$, is modelled as follows:

$$\Pi_{ij,2} = -C_2\left[(P_{ij} + \Omega_{ij} - C_{ij}) - \frac{2}{3}\delta_{ij}(P - C)\right] \qquad (2\text{--}55)$$

Where P_{ij} and Ω_{ij} are the same terms as in equation (2–50), $C_{ij} = \frac{\partial}{\partial x_k}(\rho u_k\overline{u_i'u_j'})$, $P = \frac{1}{2}P_{kk}$ and $C = \frac{1}{2}C_{kk}$.

The wall-reflection term, $\Pi_{ij,w}$, is modelled as:

$$\Pi_{ij,w} = C_{1w}\frac{\varepsilon}{k}\left(\overline{u_k'u_k'}n_kn_m\delta_{ij} - \frac{3}{2}\overline{u_i'u_k'}n_jn_k - \frac{3}{2}\overline{u_j'u_k'}n_in_k\right)\frac{k^{3/2}}{C_l\varepsilon d} \qquad (2\text{--}56)$$

$$+ C_{2w}\left(\Pi_{km,2}n_kn_m\delta_{ij} - \frac{3}{2}\Pi_{ik,2}n_jn_k - \frac{3}{2}\Pi_{jk,2}n_in_k\right)\frac{k^{3/2}}{C_l\varepsilon d}$$

In equation (2–56) n_i is the unit vector normal to the wall, d is the normal distance to the wall and $C_l = C_\mu^{3/4}/\kappa$, where the von Kármán constant $\kappa = 0.4187$. The constants used in equation (2–50) to equation (2–56), C_μ, C_1, C_2, C_{1w}, C_{2w}, $C_{1\varepsilon}$ and $C_{1\varepsilon}$ are quoted in table 2–7.

Table 2–7 Constants in the RSM model (Fluent Inc., 2003).

C_μ	C_1	C_2	C_{1w}	C_{2w}	$C_{1\varepsilon}$	$C_{2\varepsilon}$
0.09	1.8	0.6	0.5	0.3	1.44	1.92

Modelling of swirl flow

Two of the turbulence models presented here, namely the standard k-ε and the RNG k-ε models, are based on the assumption that the turbulence is isotropic, i.e. turbulence is independent of spatial directions. When it comes to swirling flows, this assumption is incorrect (Gupta et al., 1984). Other shortcomings of two equation models are the inability to account for extra strain and a poor prediction of flows with high pressure gradients and in reattachment regions (Hanjalic, 2002).

Nevertheless, some workers have had some success in predicting swirling flows by applying various two equation turbulence models. Both Widman et al. (2000) and Verboven et al. (2000) found agreement between experimental data for a swirling flow and computations using the RNG k-ε model. For the standard k-ε model, Widman et al. (2000) concluded that there was no agreement with their experiments. Engdar and Klingmann (2002) investigated six various two equation models for a 2D swirling flow and found some agreement for moderate swirl with no internal recirculation ($S = 0.33$), but at strong swirl with a central recirculation zone all the two equation models failed to predict the flow. Benim (1990) investigated the difference between a standard k-ε model and an algebraic stress model (ASM) in comparison with experimental measurements in a swirling flow. The ASM performed significantly better than the k-ε model, especially the internal recirculation zone was predicted more accurate using the ASM. Nikjooy and Mongia (1991) compared the performance of the ASM and a RSM in a strong swirling flow. Their study found the ASM unsuitable to predict the central recirculation zone and recommended the RSM for modelling of strong swirling flows. A similar comparison of turbulence models was carried out by Sharif and Wong (1995) for strong swirling flows. In their study, a swirling flow with swirl number 2.25 was modelled using a RSM, an ASM and a nonlinear k-ε model. This study concluded that there was a marginal improvement from the ASM to the RSM which both predicted the flow fields reasonably good. The nonlinear k-ε model on the other hand failed to predict the recirculation zone satisfactory compared to the experimental data. Most recently Xia et al. (1998) carried out a numerical and experimental investigation of a strong swirling flow ($S = 1.68$) in a water model. The turbulence models considered were the standard k-ε model, the RNG k-ε model and the RSM. This investigation emphasises the superiority of the RSM: the shape and size of all the recirculation zones were predicted correctly, whereas the two equation k-ε models did not reveal all the recirculation zones and failed to predict the size and strength of them. Both the standard k-ε and the RNG k-ε model predicted the swirling flow to evolve into a solid-body type of rotation, which were found by Sharif and Wong (1995) as well. This indicates that the k-ε models are unable to account for the interaction between swirl and turbulence and to reproduce the combined free-forced vortex character of the swirling flow as the RSM does (Xia et al., 1998).

When modelling swirling flow, by assuming the flow geometry to be axisymmetric and that there are no circumferential gradients in the flow, the computation can be done in 2D

(Fluent Inc., 2003). This will simplify the computation, and reduce the computational time to solve the governing equations for turbulent flow. For a 2D swirling flow, the tangential momentum equation can be written in cylindrical coordinates as follows (Fluent Inc., 2003):

$$\frac{\partial}{\partial t}(\rho u_\theta) + \frac{1}{r}\frac{\partial}{\partial x}(r\rho u_x u_\theta) + \frac{1}{r}\frac{\partial}{\partial r}(r\rho u_r u_\theta)$$

$$= \frac{1}{r}\frac{\partial}{\partial x}\left[r\mu\frac{\partial u_\theta}{\partial x}\right] + \frac{1}{r^2}\frac{\partial}{\partial r}\left[r^3\mu\frac{\partial}{\partial r}\left(\frac{u_\theta}{r}\right)\right] - \rho\frac{u_r u_\theta}{r}$$

(2–57)

Where x is the axial coordinate, r is the radial coordinate, u_x is the axial velocity, u_r is the radial velocity and u_θ is the swirl velocity.

2.5.3   Modelling reacting flow

The introduction of chemical species reactions into the modelling of turbulent fluid flow further complicates the solution process. Even the simplest hydrocarbon reactions mechanisms might consist of hundreds of elementary reactions (Simmie, 2003). However, with the introduction of some simplifying assumptions, a reasonable prediction can be made for these flows.

Eddy Dissipation Model

The conservation of chemical species mass is described by equation (2–25). Closing of this equation requires modelling of the production rate term. A model for this chemical source term was proposed by Magnussen and Hjertager (1976). They assumed that the chemical reactions in turbulent flow were very fast compared to the rate of turbulent mixing and that the reaction rate was controlled by this. Since the reaction of fuel and oxidizer requires both fuel and oxidizer to be present on a molecular scale together with hot combustion products for ignition, the reaction rate will be limited by the quantity of smallest local concentration. The rate of combustion of fuel could then be modelled by equation (2–58) where $\bar{Y}_f$, $\bar{Y}_o$ and $\bar{Y}_p$ are local mean mass fractions of fuel, oxidizer and products respectively.

$$R_f = A\rho\frac{\varepsilon}{k}min\left(\bar{Y}_F, \frac{1}{v}\bar{Y}_o, B\frac{1}{1+v}\bar{Y}_p\right)$$

(2–58)

A and B are empirical constants equal to 4.0 and 0.5 respectively and v is the stoichiometric oxidizer to fuel mass ratio.

Mixture fraction: equilibrium model and flamelet model

When modelling turbulent reacting flow, the solution of one transport equation for each chemical species taking part in the reaction mechanism might be precluded by applying a mixture fraction approach. The mixture fraction, f, is a conserved scalar and is defined by (Jones and Whitelaw, 1982):

$$f = \frac{Y_i - Y_{i,o}}{Y_{i,f} - Y_{i,o}} \tag{2-59}$$

Where Y_i is the mass fraction of element i. The subscript f and o denotes the mass fraction values in the fuel and oxidizer stream respectively. The thermochemical state of the fluid (i.e. the density, temperature and species concentration) can then be predicted from the mixture fraction distribution. The reacting system can now be treated with a model for infinitely fast chemistry (mixed is burnt), a chemical equilibrium model or a non-equilibrium flamelet model which can incorporate detailed chemical kinetics (Fluent Inc., 2003).

The transport equations for the mean mixture fraction ($\overline{f}$) and its variance ($\overline{f'^2}$) in a turbulent flow are given by Jones and Whitelaw (1982):

$$\frac{\partial}{\partial t}(\rho \overline{f}) + \frac{\partial}{\partial x_i}(\rho u_i \overline{f}) = \frac{\partial}{\partial x_i}\left(\frac{\mu_t}{\sigma_t}\frac{\partial}{\partial x_i}\overline{f}\right) \tag{2-60}$$

$$\frac{\partial}{\partial t}(\rho \overline{f'^2}) + \frac{\partial}{\partial x_i}(\rho u_i \overline{f'^2}) = \frac{\partial}{\partial x_i}\left(\frac{\mu_t}{\sigma_t}\frac{\partial}{\partial x_i}\overline{f'^2}\right) + C_g \mu_t \left(\frac{\partial}{\partial x_i}\overline{f}\right)^2 - C_d \rho \frac{\varepsilon}{k}\overline{f'^2} \tag{2-61}$$

Where σ_t, C_g and C_d are constant equal to 0.7, 2.86 and 2.0, respectively.

The transport equations, equation (2–60) and equation (2–61), predict the mean mixture fraction and its variance in a turbulent flow. These time-averaged values can be linked to the instantaneous mixture fraction using a probability density function (PDF) (Fluent Inc., 2003). The PDF, written as $p(f)$, is the probability that the fluid exists at the state f. This is illustrated for a turbulent flow in figure 2–16. The value of f fluctuates with time, t, as plotted in the right side of the figure, and spends a certain amount of time in the range denoted as Δf. $p(f)$ plotted in the left side of the figure takes the value such that the area under its curve in the band Δf is equal to the fraction of time f spends in this range. Mathematically this can be written:

$$p(f)\Delta f = \lim_{t \to \infty}\frac{1}{t}\sum_i \tau_i \tag{2-62}$$

Where τ_i is the fraction of time that f spends in the Δf band.
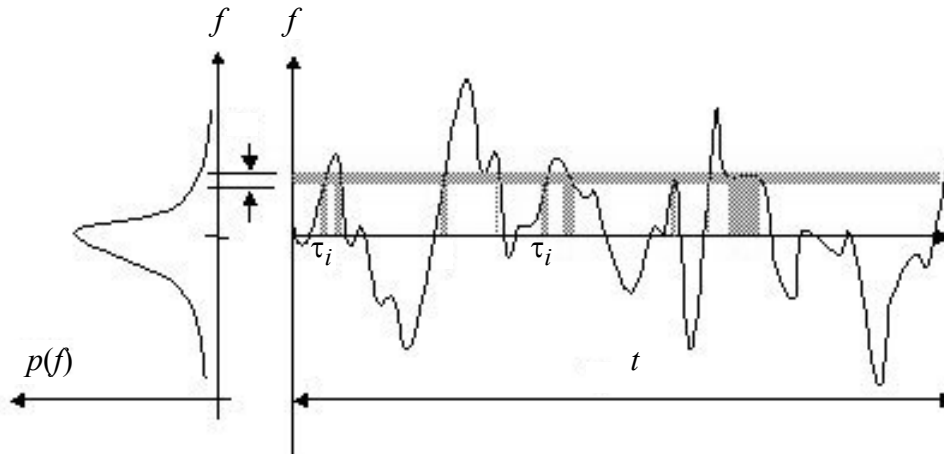
Figure 2–16 Graphical description of the probability density function (Fluent Inc., 2003).

From *p(f)* the averaged values, $\overline{\phi}_i$, of the species mole fractions and temperature can be determined as follows (Jones and Whitelaw, 1982):

$$\overline{\phi}_i = \int_0^1 p(f)\phi_i(f)df \qquad (2\text{–}63)$$

In the case of non-adiabatic systems, a transport equation must be solved for the enthalpy and included into equation (2–63) as well. To simplify the computation of *p(f)*, an assumed PDF which calculates the value of *p(f)* from the value of the mean mixture fraction and its variance as found from the transport equations above, equation (2–60) and equation (2–61), can be applied. Various assumed shapes can be found for the PDF in literature (Jones and Whitelaw, 1982); the rectangular wave function, the double delta function, the clipped Gaussian distribution and the β-function.

From equation (2–63), the chemical state of the system can be determined. This can be done by using an equilibrium model which assumes that the chemistry is rapid enough for chemical equilibrium to always exist at the molecular level. An algorithm based on the minimization of Gibbs free energy (Kuo, 1986 p101-104) is used to compute species mole fractions from *f*. These equilibrium calculations can be precalculated and stored in a look-up table before modelling the turbulent flow field where the interaction of turbulence and chemistry is accounted for with the PDF. The advantage of this model is that it can predict the formation of intermediate species without requiring the knowledge of detailed chemical kinetic rate data (Fluent Inc., 2003). Instead of defining a specific multi-step reaction mechanism, only the important chemical species present in the system are defined. The mole fraction of each species based on chemical equilibrium is then predicted.

The flamelet model is a non-equilibrium model that can be used in conjunction with the mixture fraction to account for chemical reactions in turbulent flow. In many cases, such as modelling of the rich fuel side of hydrocarbon flames, predicting the intermediate species that govern the formation of NO_x and modelling flame extinction that occurs when the mixing rate is too fast for the chemical reactions rate to keep pace, the equilibrium model might break down, while the flamelet model might give more realistic results (Flu-

ent Inc., 2003). The flamelet concept models turbulent flames as an ensemble of thin, laminar, locally one-dimensional flames called flamelets (Peters, 1984 and 1986). Each flamelet is assumed to have the same structure as laminar flames in simple configurations, and are obtained either by experiments or calculations. As for the equilibrium model, the chemistry of the flamelets can be precalculated and stored in a look-up table before the modelling of the turbulent reacting flow. In contrast to the equilibrium model, the flamelet model incorporates detailed chemical mechanisms resulting in a more realistic prediction of the turbulent combustion.

3   *Experimental Apparatus*

3.1   Introduction

In this section the Swirl burner and the experimental apparatus used in the experiments with this burner will be described. In general, the apparatus consists of boilers/combustion chambers of various sizes and flue gas analysers used in conjunction with these to measure the flue gas composition of O_2, CO and NO_x. The apparatus used in the LIF experiments at the University of Leeds will also be described here.

3.2   The Swirl Burner

The target for the Swirl Burner design was to achieve a stable flame, rapidly mix the fuel and the air and to induce internal flue gas recirculation (FGR) in a fan driven gas burner. The first prototype was designed with the possibility for air staging (Røkke, 1994). The first Swirl Burner prototype can be seen in figure 3–1. The burner consists of an inner gas tube from where fuel gas is injected into the primary air through gas nozzles which consists of drilled holes in the fuel tube. The primary air flows through the annulus surrounding the gas tube where it is given rotation by a vane swirl generator. The primary air annulus ends in a converging conical section. The secondary air is supplied through the outer annulus seen in figure 3–1. The effect of co-swirling and counter-swirling staged air could be investigated by the adjustable vanes fitted in the staged air supply. Combustion air is supplied by a standard air fan on which the burner head is mounted. The first prototype of the Swirl Burner was tested by Røkke (1994) and the main results of these experiments are summarized in Spangelo et al. (2003) which can be found in appendix A.

1. GAS TUBE
2. EXTERNAL SUPPORT FINS
3. INTERNAL SUPPORT FINS
4. EXTERNAL FLAME TUBE
5. INTERNAL FLAME TUBE
6. INTERNAL BLADES (6 vanes)
7. GAS OUTLET
8. EXTERNAL BLADES (12 vanes)
9. ADJUSTMENT MECHANISM
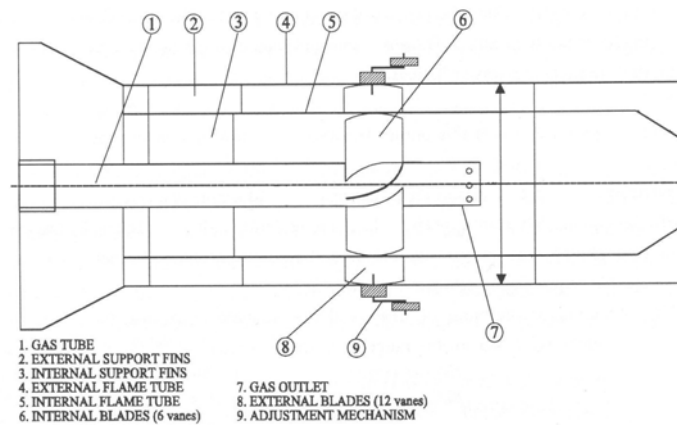
Figure 3–1 Diagram of the first prototype of the Swirl Burner (Røkke, 1994).

Reduction of NO_x formation in burners by internal FGR and how this is achieved by using swirling flows is described in chapter 2.2. When the swirl number (*S*) defined by equation (2–8) exceeds the critical value of 0.6, a central toroidal recirculation zone (CTRZ) is created where internal FGR takes place. Typical profiles of axial and swirl velocity component in the CTRZ in a strong (*S* > 0.6) swirling flow is illustrated in figure 2–10.

When the rotating flow is set up by the use of a vane swirl generator, as in the Swirl Burner, the swirl number given by equation (2–8) in chapter 2.2 can be expressed by the swirl generator hub diameter d_h, the outer swirl generator diameter *d* and the exit angle of the swirl vanes, β, as follows (Gupta et al., 1984):

$$S = \frac{2}{3}\left(\frac{1 - (d_h/d)^3}{1 - (d_h/d)^2}\right)\tan\beta \qquad (3-1)$$

The notations used in equation (3–1), d_h, d and β, are illustrated in figure 3–2. A photograph of the swirl generator which is mounted on the gas tube can be seen in figure 3–3.
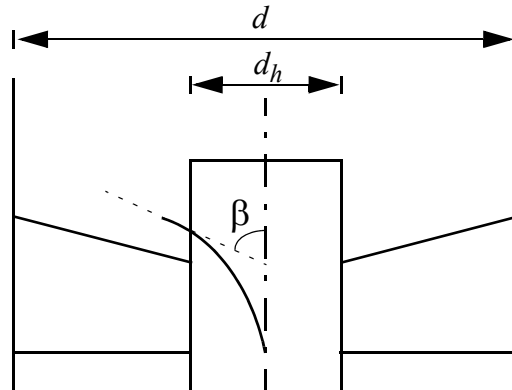
Figure 3–2 Swirl generator diagram indicating d, d_h and β. Flow direction upward on diagram.
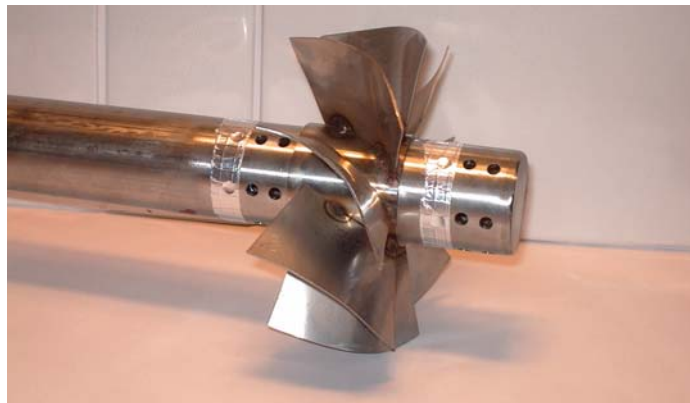
Figure 3–3 Burner insert for Swirl Burner (370 kW) showing swirl vanes and fuel nozzles upstream and downstream of the swirl generator.

With the first prototype of the Swirl Burner experiments were carried out to investigate the effect of staged air. The secondary air supply was given co-swirl, no swirl and counter-swirl, but neither of these were found beneficial with regards to the NO_x emissions compared to no air staging (Røkke, 1994). As a result of the experience with the first Swirl Burner prototype, the design was simplified by removing the staged air supply. The second design is shown schematic in figure 3–4. As seen, the burner now consists of the gas tube surrounded by only the primary air annulus. The fuel nozzles can be positioned on both the upstream and the downstream side of the swirl generator. The second prototype was designed for a nominal thermal throughput of 200 kW. This burner will therefore be referred to as the 200 kW Swirl Burner. The 200 kW Swirl Burner design was optimized for low NO_x emissions by experiments. These experiments are described in appendix A and summarized in chapter 4.1.
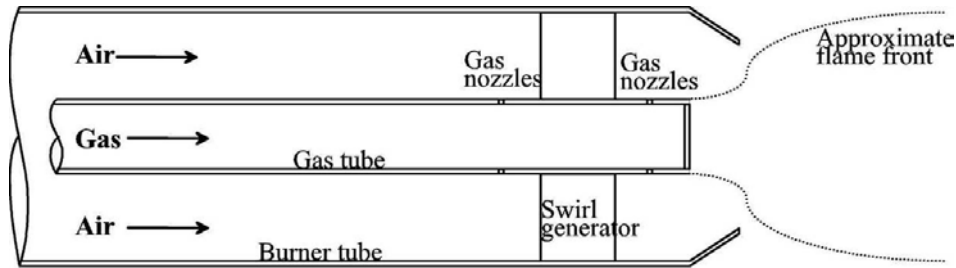
Figure 3–4 Diagram of the second prototype of the Swirl Burner concept

The second Swirl Burner prototype is a patented low NO_x burner concept. As opposed to other fan burners of similar size utilized in boilers where moderate swirl might be used to improve mixing of fuel and combustion air, the Swirl Burner operates with significantly higher swirl intensity to achieve both improved mixing of fuel and air and to induce internal FGR. This NO_x reduction technique can be found in gas turbine burners that operates at higher pressures and in large industrial burners where combustion air is supplied to the burner at higher pressures than available from a standard combustion air fan.

After optimizing the 200 kW Swirl Burner, the burner was scaled to different throughputs to make the Swirl Burner concept applicable to a wider range of applications. The burner was scaled upwards to a nominal throughput of 370 kW and downwards to 20 kW. Both the scaling and the experiments with the scaled burners are described in chapter 4. The burner insert for the 370 kW burner is shown in figure 3–3. In this picture the swirl vanes are mounted on the gas tube. The holes seen in the gas tube in figure 3–3 are the fuel nozzles where the fuel gas is injected into the combustion air. Variation of the nozzle size, number and distribution around the swirl generator as described in chapter 4, was done using an aluminium tape as seen in this photograph or ceramic glue which both were easy to apply and to remove from the nozzles.

The swirl generators have been made by cutting the vane blades from a steel plate before curving them by rolling. The curved swirl vanes were welded to a flange that was fitted on the gas tube. For the smaller 20 kW burner, the swirler did not turn out accurate enough by this way of manufacturing the vanes. A 3D model of the swirler was therefore created using AutoCAD. A drawing of this model can be seen in figure 3–5b). The CAD model was then used to create an accurate swirl generator by a rapid prototyping method called Selective Laser Sintering (SLS) which created a 3D "printout" of the CAD model. SLS is a technique where a 3D solid body is built by sintering a powder in successive layers by a laser beam. A metal powder was used for the swirler. A photograph of the SLS made swirl generator is seen in figure 3–5a). This swirler was much more accurate and symmetric than the previous handmade swirlers. This was an advantage in the laser experiments which are described in chapter 4.5.
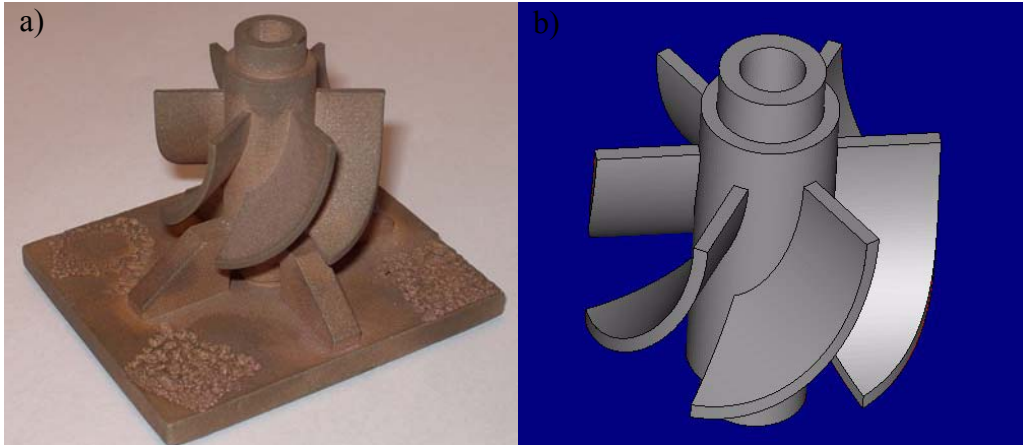
Figure 3–5 20 kW swirl generator, (a) laser sintered (metal); (b) CAD model.

3.3   The CEN boiler

The burner prototypes described in this thesis were first designed to fit in a CEN (Comité Européen de Normalisation) boiler. This is a conventional water-cooled boiler that can be used with either reversed flow or straight through flow, alternatively a combination of these. Due to experience gained by Røkke (1994) regarding a reverse flow type boiler and the Swirl Burner, all experiments described here were done using the straight through flow alternative. The diameter of the boiler was 0.4 m, and the maximum load was 250 kW. A diagram of the CEN boiler is shown in figure 3–6. As seen in the diagram, the length of the combustion chamber could be varied by moving the rear wall. The chamber length was set using equation (3–2) where l is the length in meter and Q is the thermal load in kW. In these experiments the length was set using $Q = 250$ kW which results in a chamber length of 1.15 m.

$$l \ = \ 0.23 \sqrt{\frac{Q}{10}} \qquad\qquad (3–2)$$

A cooling water circuit which the boiler was connected to kept the water temperature in the boiler during experiments around 70 - 80 °C. To avoid dilution of flue gases by air from the surroundings, a positive pressure of about 50 - 60 Pa was maintained in the boiler while in operation.

Fuel gas was supplied from a central propane evaporator and metered in a Fischer & Porter FP 3/4-21-GSVT-54 glass-tube rotameter. Alternatively, methane or natural gas could be supplied from gas bottles connected to the same glass-tube rotameter. The rotameter inaccuracy was ±0.25% of the visual reading plus ±1.0% intrinsic rotameter inaccuracy, in total an error of ±3.75 kW. Combustion air was supplied by the burner fan and adjusted by the O_2 content in the flue gases.
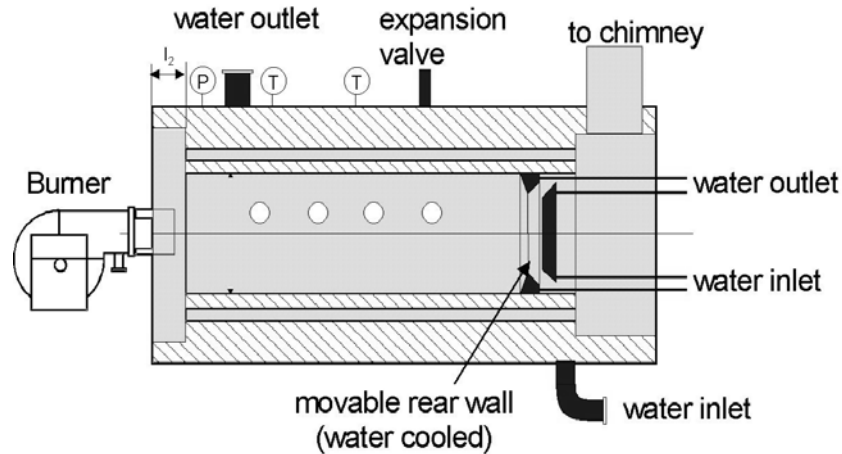
Figure 3–6 The CEN boiler.

3.4 The vertical downdraught boiler

Testing of scaled burners with a higher thermal throughput than the maximum capacity of the CEN boiler was made possible by refurbishment of a vertical downdraught boiler. A diagram of the vertical boiler is shown in figure 3–7 and is described by Røkke (1994). The diameter of the combustion chamber in this boiler is 0.685 m. The back wall can be moved to change the length of the combustion chamber between 1 m and 4.814 m. According to the European Standard EN 303-3:1998 (Comité Européen de Normalisation, 1998), the dimensions of this boiler make it suitable for burners up to a thermal throughput of at least 1 MW (see figure 3–8).

As a part of the refurbishing of this boiler, the cooling system was upgraded. The vertical boiler consists of 9 separate boiler elements, interconnected by a cooling water circuit. The cooling water was supplied directly from tap, which maintains a temperature of about 7 °C, resulting in too much cooling of the combustion chamber and condensation of flue gases on the inside. To avoid this, the cooling circuit was closed using a heat exchanger and a bypass valve regulated by the exit water temperature at the top of the boiler. This temperature was set to 80 °C. The thermal throughput of the vertical boiler was now limited by the capacity of heat exchanger used in the cooling circuit, which was found to be about 550 kW.

Fuel gas was supplied from the same propane evaporator as for the CEN boiler. The mass-flow of propane was metered using a Bronkhorst HI-TEC F-106A-HDD mass-flow meter connected to an IMP and continuously logged on a computer. Specified inaccuracy of the mass-flow meter was ±0.2% of full scale plus ±0.7% of the actual reading, which means an error of ±5.95 kW at 550 kW. Combustion air was supplied by the burner fan and adjusted by the O_2 content in the flue gases. A flame guarding system consisting of a UV lamp and a magnetic valve for immediate shut-down of the fuel gas supply was fitted to ensure safe operation.
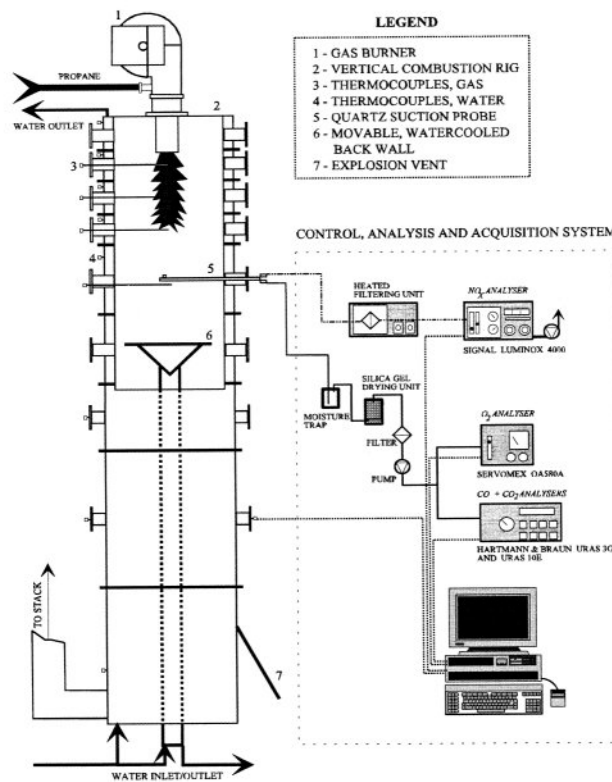
Figure 3–7 Vertical rig and data acquisition system (Røkke, 1994).

3.5   Combustion chamber with optical access

For in-flame measurements using laser techniques, a water-cooled combustion chamber with optical access had to be constructed. According to the European Standard EN 303-3:1998 (Comité Européen de Normalisation, 1998), the minimum dimensions of a combustion chamber as a function of the output is given by the graph in figure 3–8. The combustion chamber was designed for burners with a maximum output of 20 kW, which corresponds to a combustion chamber diameter of 0.20 m according to the CEN standard.

To avoid complications when mounting quartz windows on a curved surface, the combustion chamber was designed with an octagonal cross-section as seen in figure 3–9(a). This cross-section encloses a circle with diameter 0.20 m. To fit a wider window in front of the chamber, the octagonal was stretched to make the front and back section of the chamber 5 mm wider. The hydraulic diameter of the octagonal combustion chamber was 0.213 m, which complies with the minimum specifications in the European Standard (figure 3–8). The height of the combustion chamber was 0.69 m including a 9 cm restriction reducing the chamber cross-section to a 0.1 m diameter exhaust duct. During experiments a back-pressure was introduced into the combustion chamber by restricting the flow in the exhaust duct. The optical access for LIF measurements was through 3 UV quality fused silica windows with a surface flatness of $\lambda/4$ @633 nm. 2 of the windows (20 mm x 400 mm) was mounted on each side of the chamber to let the laser beam pass through the combustion chamber and the flame as indicated in figure 3–13. Fluorescence from the flame is observed perpendicular to the laser beam and picked up through the third quartz window (70mm x 400 mm) mounted in front of the combustion chamber. The combustion chamber was made in stainless steel. A 3D AutoCad-generated drawing of the combustion chamber can be seen figure 3–9(b).
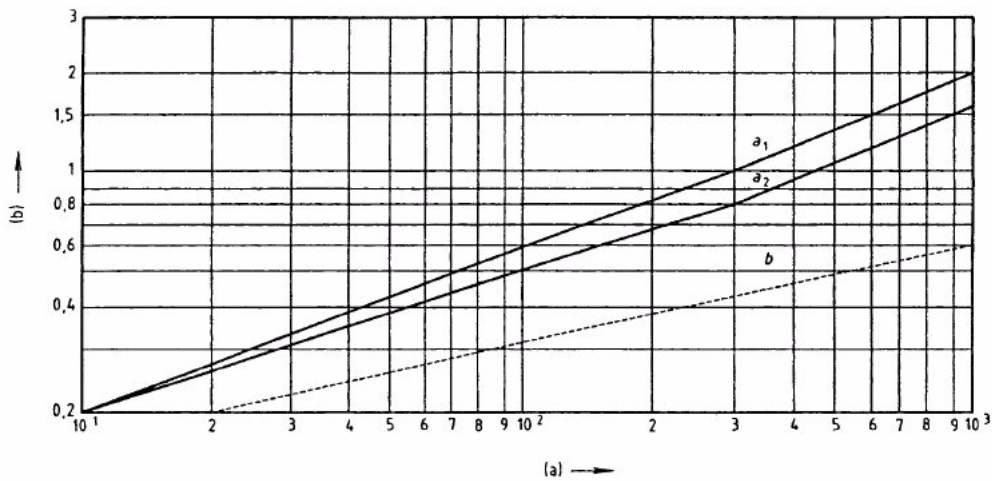
(a) Nominal useful output, P_n, in kW
(b) Diameter and length of the combustion chamber, in m

a: distance from the deflector plate of the burner up to the opposite wall of the combustion chamber
a_1: for combustion chamber with direct flame
a_2: for combustion chamber with flame reversal
b: diameter of the combustion chamber or diameter of the equivalent circular section if the real section is not circular

Figure 3–8 Minimum dimensions to the combustion chamber, European Standard EN 303-3:1998 (Comité Européen de Normalisation, 1998).
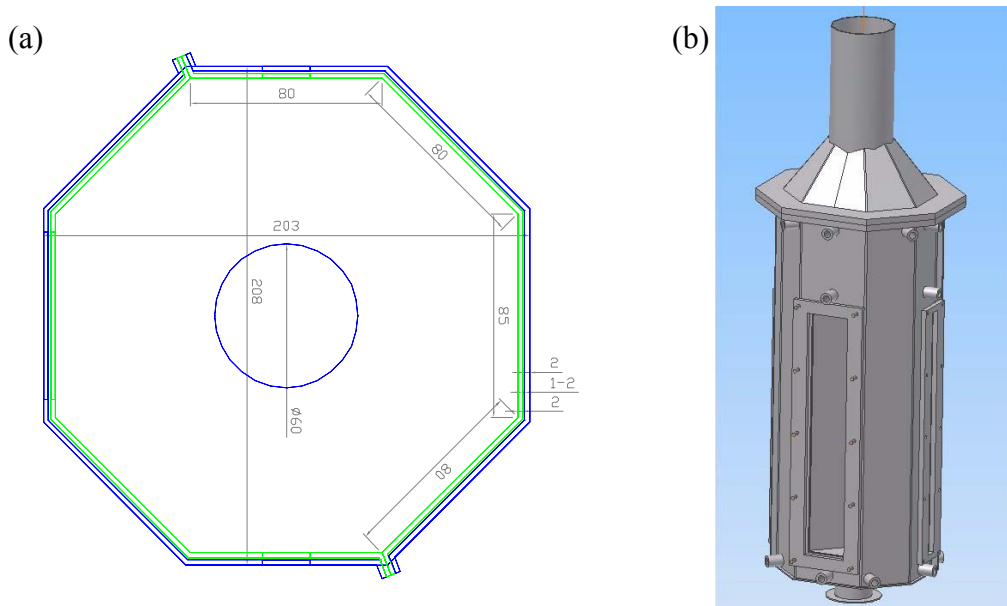
Figure 3–9 LIF Combustion Chamber a) cross-section, dimensions in mm b) assembled.

The combustion chamber was placed on a computer controlled x-y-z traverse with a positioning accuracy of 0.05 mm in each direction. Due to the maximum weight capacity of the traverse being 20 kg, a counterbalance system was used to enable traversing of the combustion chamber that had a weight of about 60 kg. The counterbalance system consisted of a steel frame and pulleys. The combustion chamber was then counterbalanced via a steel wire over the pulleys joining the chamber with weights. The steel frame and the combustion chamber can be seen in the centre of the photograph in figure 3–10.

Fuel gas was supplied from gas bottles and metered in a Solartron Mobrey KDG Series 2000 VA 14X rotameter with a Type A float. The rotameter inaccuracy was ±5% of full scale reading, i.e. an error of ±1.9 kW for propane. Combustion air was supplied from a pressurized air distribution net in the lab and adjusted by the O_2 content in the flue gases. For security reasons a flame guarding system was used. This consisted of a thermocouple positioned close to the flame without disturbing the flow. The thermocouple was connected to a device that closed the fuel gas supply if the flame was extinguished.
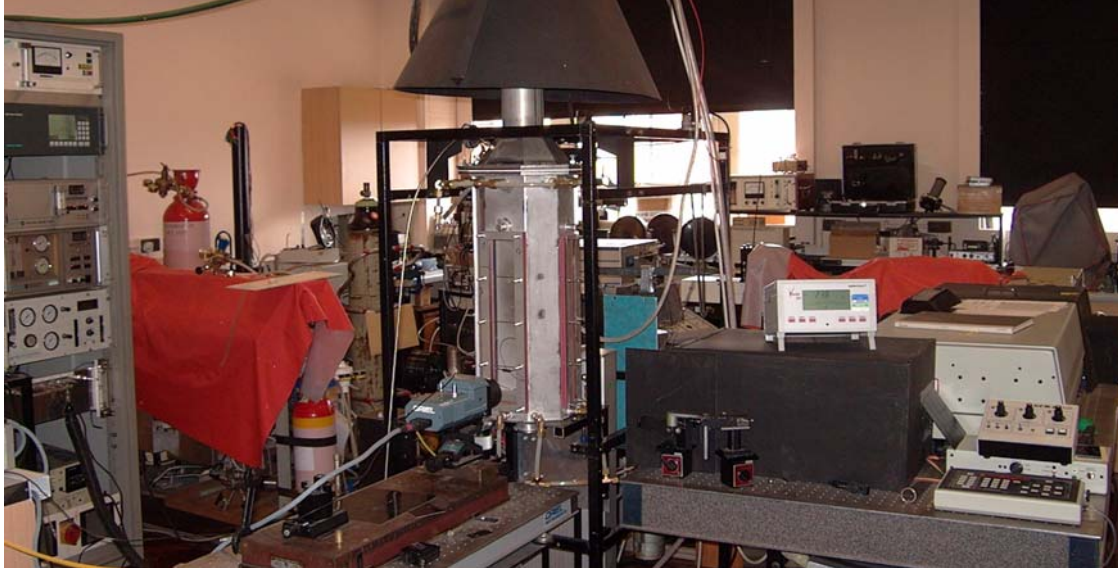
Figure 3–10 LIF Combustion Chamber mounted in lab.

3.6   Gas analysers

In conjunction with burner experiments in the CEN boiler and the Vertical boiler, the flue gas composition was analysed using a Signal Luminox Series 4000 NO_x analyser, a Sybron Taylor Servomex Series 500 O_2 analyser and a Hartmann & Braun Uras 3G CO/CO_2 analyser. The data from the analysers were continuously logged via an IMP connected to a computer. A diagram of the setup for flue gas analysis is shown in figure 3–11. The flue gas was sampled via suction probes positioned in the centre of the stack close to the flue gas exit from the boilers. NO_x was measured on a wet basis. Condensers and moisture traps where NO_2, which is soluble in water, could be separated was then avoided. Measurements are corrected to dry basis before presented here. CO and O_2 were measured on a dry basis. All burner experiments were, if not stated otherwise, run at 3% O_2 in the flue gas. If not, measurements were corrected to 3% O_2. The random error of the analysers is stated in table 3–1. An error due to the manual adjustment of the calibration is assumed to be ±0.25%. Reproduceability of the emission measurements with these analysers was verified by repeating a test series with propane in the CEN boiler at different times during a period of 2 years. These test series will be presented in chapter 4.

Table 3–1 Inaccuracy of gas analysers used in conjunction with the CEN boiler and the Vertical boiler (FS = full scale).

	Analyser	Range used	Accuracy	Calibration gas	Total expected error
O_2	Sybron Taylor Servomex Series 500	0 - 25 vol%	±1% FS	Ambient air	±0.3%
CO	Hartmann & Braun Uras 3G	0-100 ppmv	±0.2 FS	86 ppmv CO	±0.4 ppmv
NO_x	Signal Luminox Series 4000	0 - 100 ppmv	±1.5% FS	87.4 ppmv NO	±1.7 ppmv
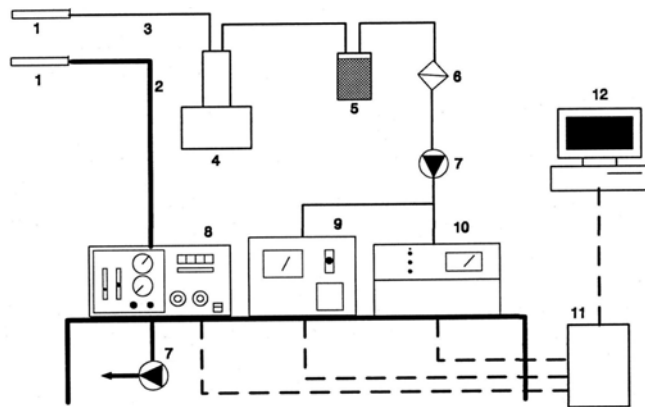
1 Suction probe
2 Heated Sample Line
3 Sample Line
4 Condenser

5 Silica gel
6 Filter
7 Pump
8 NO_x analyser

9 O_2 analyser
10 CO analyser
11 IMP
12 Computer

Figure 3–11 Flue gas sample and analysis system

The flue gas composition was also measured when using the combustion chamber with optical access. The flue gases were sampled trough a probe positioned in the centre of the exhaust flow from the combustion chamber. O_2 was analysed using a Servomex paramagnetic gas analyser. The CO analyser was a Hartmann and Braun Advanced Optima Uras 14 infrared absorption analyser. Before entering the CO and O_2 analysers, the flue gas was dried in a water condenser. NO_x concentrations were measured using a Signal Series 4000 chemiluminescence gas analyser. The NO_x analyser was supplied with flue gas trough a heated line to avoid condensation in the sampling line. A photograph of the flue gas analysers is shown in figure 3–12. The flue gas composition was continuously logged using a data logger connected to a computer with standard logging software. The random error of these analysers is stated in table 3–2. Also here an error of ±0.25% is assumed to be due to the manual adjustment of the calibration.

Table 3–2 Inaccuracy of gas analysers used in conjunction with the combustion chamber with optical access.

	Analyser	Range used	Accuracy	Calibration gas	Total expected error
O_2	Servomex	0-25 vol%	±1% FS	Ambient air	±0.3%
CO	Hartmann and Braun Advanced Optima Uras 14	0-1000 ppmv	±2% FS	920 ppmv	±22.3 ppmv
NO_x	Signal Series 4000	0-100 ppmv	±1% FS	38.2 ppmv	±1.1 ppmv

O_2 Analyser

CO Analyser

CO_2 Analyser (not in use)
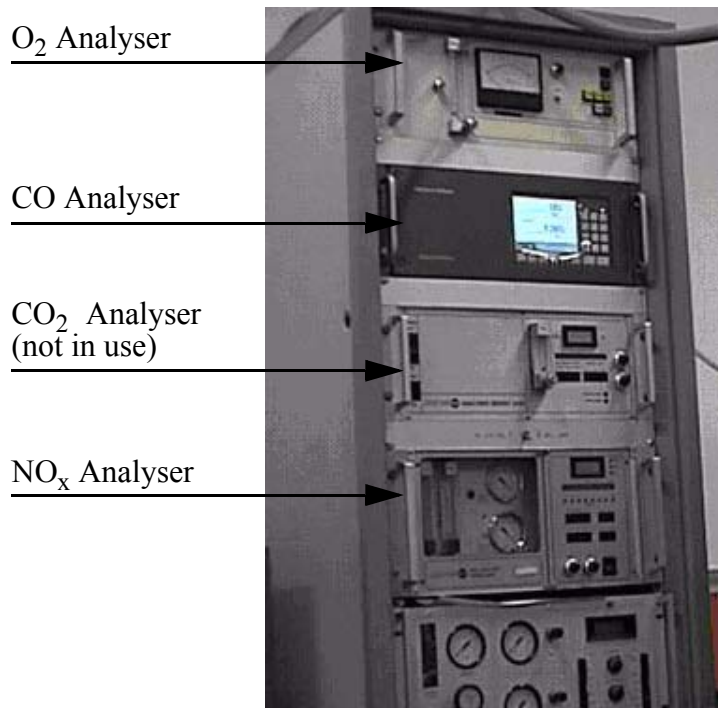
NO_x Analyser

Figure 3–12 Photograph of gas analysers used with the LIF combustion chamber.

3.7   Laser Induced Fluorescence

OH Laser Induced Fluorescence (LIF) measurements were done using a Spectra Physics GCR-11 Nd:YAG laser pumping a Lumonics HD-300 dye laser using Rhodamine 590. This system was set up to generate pulsed laser light at 10 Hz and a wavelength of 283.632 nm in order to excite the $Q_2(7)$ transition of OH $A^2\Sigma^+$ - $X^2\Pi_i$ (1,0). This transition was chosen by investigating the temperature dependence of relevant OH transitions at the expected flame temperatures for this flame using the computer program LIFBASE (Luque and Crosley, 1999). A schematic diagram of the LIF facility used in these experiments is shown in figure 3–13.

To provide a tuneable narrow line-width (0.075cm^{-1}) excitation source, the 1064 nm fundamental beam from the Nd:YAG was frequency doubled using a KDP crystal, and cleaned of any fundamental by the sequential use of two dichroic mirrors prior to the dye laser. The output from the dye laser was frequency doubled, again using a second KDP crystal, and tuned to 283.632 nm and focused into the flame imaging region using a long focal lens. The visible un-doubled beam from the second KDP crystal was separated from the UV beam using a Pelin Broca prism and diverted into a Scientech Detector AC25UV (0.19-0.35 μm) using a mirror. The detector was connected to a Scientech Vector S310 power-meter used to monitor the energy in the beam from the dye laser.

The fluorescence signal was collected perpendicular to the laser beam and focused onto an Intensified Charge Coupled Device (ICCD) 2-D array camera from Oriel (InstaSpec V ICCD), with a 10 nm FWHM band-pass filter centred around 314 nm. The camera's ICCD chip comprised 256 rows and 1024 columns and was used in conjunction with InstaSpec's data acquisition software in quantifying the amount of laser induced fluorescence produced within the swirling propane-air flame.
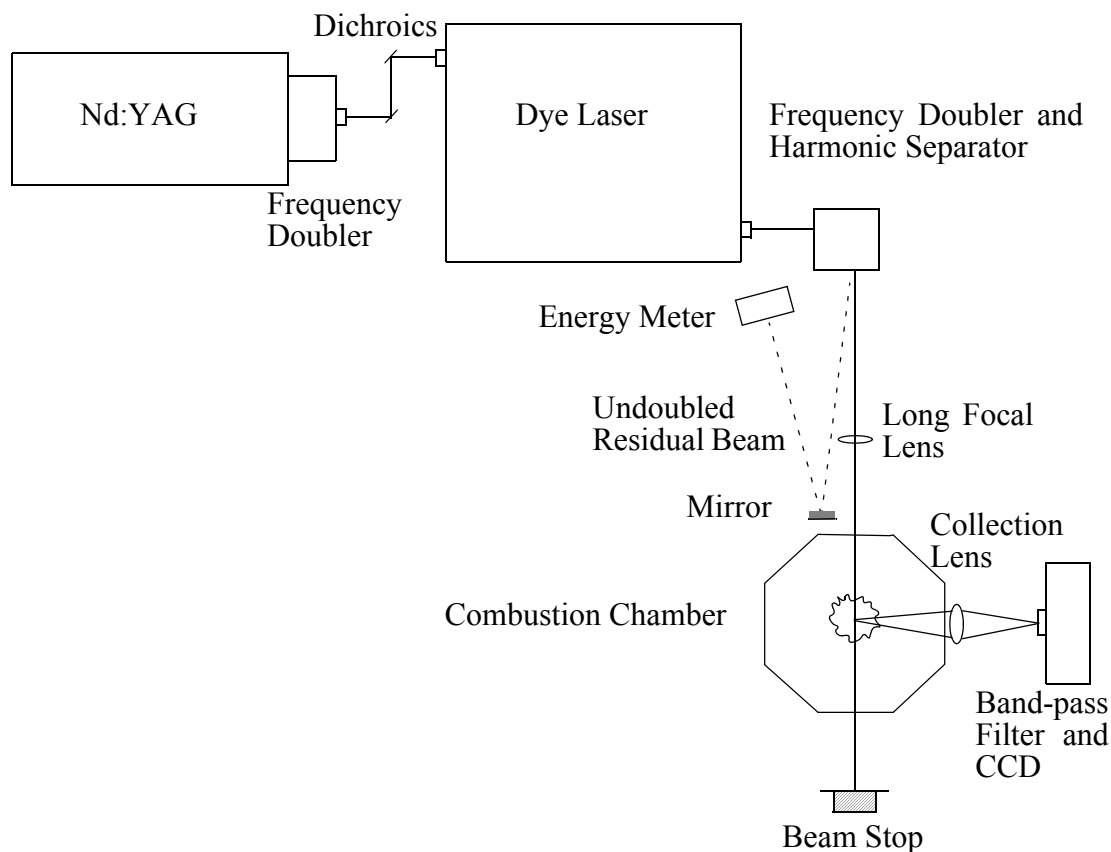
Figure 3–13 Beam path for LIF setup.

The flame was traversed vertically through the laser beam using a computer controlled x-y-z traverse accurate to 0.05 mm in each direction, on which the combustion chamber was placed. At each position the fluorescent signal from the $Q_2(7)$ transition was averaged from 1000 laser pulses to get a representative average of the OH concentrations in the flame. This average was subtracted by a background signal, acquired and averaged in the same way as the $Q_2(7)$ signal at the same positions above the burner, using a laser wavelength where there were no fluorescent signal from the flame. A 2D plot of the averaged OH concentrations was then constructed by post-processing these averages.

Before taking OH measurements, the dye laser wavelength had to be calibrated. This was done by scanning the laser through a range of wavelengths around the $Q_2(7)$ transition and recording the LIF signal from the flame as a function of wavelength. By comparing the recorded spectrum with a known spectrum achieved from LIFBASE (Luque and Crosley, 1999), the dye laser wavelength could then be tuned into the peak of the $Q_2(7)$ transition.

It was observed that the energy in the tuned laser beam was very dependent on the setting of the second KDP crystal. This setting was therefore checked and calibrated before any measurements were taken. The calibration of this crystal was carried out in a similar way as the dye laser calibration; the LIF signal was recorded as a function of the crystal setting while changing this. The crystal was then tuned back to the setting where maximum intensity of the LIF signal was observed from the flame.

In making OH LIF measurements, the laser energy was set to 40% of the maximum energy from the Nd:YAG laser. Experience with this laser setup had shown that the laser line width was lower at reduced energy which would increase the laser resolution and make it easier to resolve the peaks in the OH spectra that were close to each other. The reduced laser power also reduced the possibility of interference from photolysis of other species, such as H_2O_2 (Brownsword et al., 1997) which would increase the OH concentrations in the flame. The Nd:YAG laser energy setting was verified for each experiment by the Scientech Vector S310 power-meter reading which was set up to measure the energy content of the visible un-doubled beam from the second KDP crystal.

To achieve absolute OH concentrations from the LIF experiments with the Swirl burner, the OH LIF signal was calibrated by comparing theoretical OH concentrations with the measured OH LIF signal using a flame with theoretically known OH concentrations. For this procedure a 60 mm diameter McKenna burner was used. This is a premixed flat flame burner where a laminar flame is stabilized on a water cooled porous stainless steel plate. A photograph of the Mckenna burner is displayed in figure 3–14. The calibration was carried out with a slightly lean CH_4-air mixture ($\lambda = 1.439$), chosen because this air-fuel ratio minimized fluctuations in the flame. The OH LIF signal from the premixed laminar flat flame was then compared with a calculated OH profile for the same flame. The calculation was done using the Leeds Methane Oxidation Mechanism v. 1.5 (Hughes et al., 2001), which consists of 351 irreversible reactions of 37 species. This mechanism serves as a database for Premix (Kee et al., 1985), a computer program that utilizes kinetic, thermodynamic and transport property input data to model stable, laminar, one-dimensional, premixed flames. For an accurate calculation of the OH concentrations, a temperature profile was measured in the laminar flame and used as input into the OH computations.

The temperature profile was measured using a B-type thermocouple, with Pt-30%Rh vs. Pt-6%Rh. The thermocouple was coated with a thin layer of 98% hexamethyldisiloxane to prevent radical recombination reactions taking place on the bead surface leading to unrealistically high temperatures (Kaskan, 1957). Corrections were made for radiation heat loses from the thermocouple. This correction is described by the equation:

$$\Delta T_{rad} = \varepsilon \sigma (T_m^A - T_\infty^A)(d/\lambda Nu) \qquad (3\text{–}3)$$

Where σ is the Stefan Boltzmann constant, T_m is the measured temperature and T_∞ is the temperature of she surroundings. A bead emissivity (ε) of 0.22 was used (Kyne, 2001) and the bead diameter (d) including coating was measured to be 0.35 mm. λ is the thermal conductivity of gases at the wire temperature. The Nusselt number (Nu) is based on external flow over a sphere and is calculated from the velocity of the gases across the thermocouple. The inaccuracy of the calibrated B-type thermocouple was ±0.5 K at temperatures above 1073 K. A further error in determining the flame temperature is introduced by the

temperature correction in equation (3–3) where determination of the coated bead emissivity probably represents the largest inaccuracy. This error is difficult to quantify.

The thermocouple was aligned horizontally above the McKenna burner, as seen in figure 3–14. The thermocouple wires were stretched between two ceramic supports. One of the wires had a short section curled to form a spring ensuring horizontally stretch in the thermocouple wires and elasticity to avoid the very fragile thermocouple to break. The thermocouple wires were welded to copper wires and connected to an Iotech data logger. The temperature profile was measured by traversing the Mckenna burner vertically using the computer controlled x-y-z traverse while the thermocouple was fixed in space. Subsequent to measuring the temperature profile, OH LIF measurements were carried out using the same flow conditions in the Mckenna burner. Both temperature and OH LIF measurements were taken at 28 points from 0.0 to 16.0 mm above the burner.

The intensity of the emitted OH LIF signal might be impaired by quenching due to collisions between excited OH molecules and other molecules in the flame. This causes the excited OH molecules to return to their ground state without emitting a photon. The quenching process is composition dependent, and applying a result from a methane flame to a propane flame might therefore cause a systematic error. This error is difficult to quantify without performing further modelling studies where quenching rates caused by the major species present in a methane flame and a propane flame are compared. The measured OH signal will also be dependent on the collection optics and detector setup. These were not changed from the methane calibration experiments to the propane experiments with the Swirl Burner, and will therefore not affect the OH concentrations calculated for the Swirl Burner. The emitted OH LIF signal from the flame is dependent on the energy content of the laser beam. The laser energy was monitored using the power meter as explained above, ensuring that the laser energy was kept the same for all experiments.

Figure 3–14 Photograph of the McKenna burner; thermocouple mounted horizontally above the burner.

4   Burner Experiments and results

4.1   200 kW Swirl Burner

The 200 kW Swirl Burner has been the subject of extensive testing, during which the effect of changing geometrical parameters on the NO_x emissions and burner stability has been investigated. The effect on fuel supply pressure and air supply pressures has also been considered. During tests, the main burner geometry, i.e. the gas tube diameter, burner tube diameter and burner exit diameter, has been kept constant. Geometrical parameters that have been varied are the swirl number, positioning of the gas tube relative to the burner tube and the arrangement of fuel nozzles with regard to size, number and positioning relative to the swirl generator. The burner has been tested with a power output in the range 80 kW to 240 kW and excess air in the range 1% to 5% O_2 in the flue gases. The 200 kW Swirl Burner geometry was optimized using propane as fuel. The burner has also been tested using methane as fuel, but due to laboratory facilities these experiments are not as comprehensive as the propane experiments. An optimized burner geometry with regard to low NO_x emissions and burner stability was found for both fuels. The experiments with the 200 kW Swirl Burner are fully described in Spangelo et al. (2003) which can be found in appendix A. These experiments will be summarized here as well.

As seen from the graph displayed in figure 4–1, the NO_x emissions from the optimized 200 kW Swirl Burner are found to be in the range 32 ppmv to 43 ppmv corrected to dry conditions using propane as fuel. This graph consists of data from various test series carried out at different times over a period of 2 years, all with the same burner configuration and propane as fuel. The measured emission values are within the limits of error presented in chapter 3.6, hence indicating a good reproduceability of the emission measurements made with the gas analysers in these and the following experiments.

The graph in figure 4–2 shows how the NO_x emissions from the Swirl Burner are affected by variations in the excess air level by changing it from 3% O_2 in the flue gases to 1% and 5% in the flue gases. It is seen that at 1% O_2 the NO_x emissions are increasing with increased thermal throughput, but by increasing the excess air to 3% O_2 and 5% O_2, this trend flattens off and at 5% O_2 it is almost level within the experimental error of the gas analysers. The burner has good stability using propane as fuel at all conditions presented here and the CO emissions were found to be around 10 ppmv dry or lower during all tests.
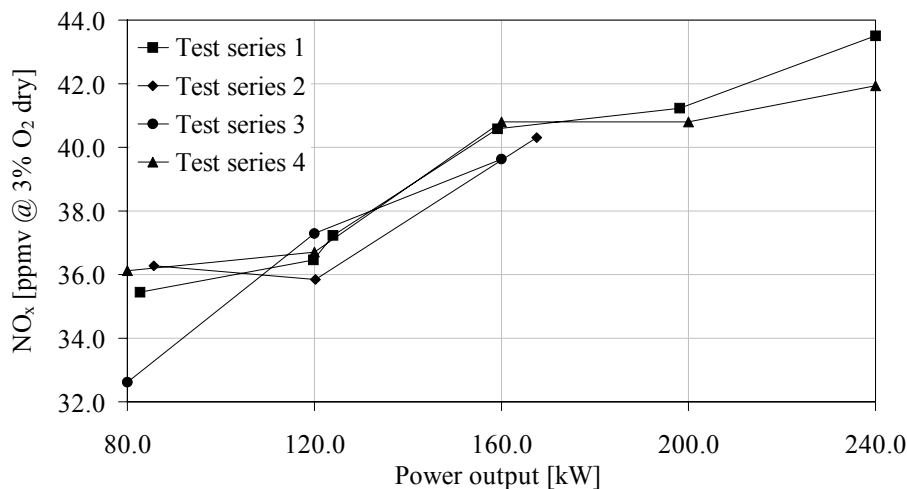
Figure 4–1 NO_x emissions for propane as a function of power output, various test series carried out with 3% O_2 in the flue gases.
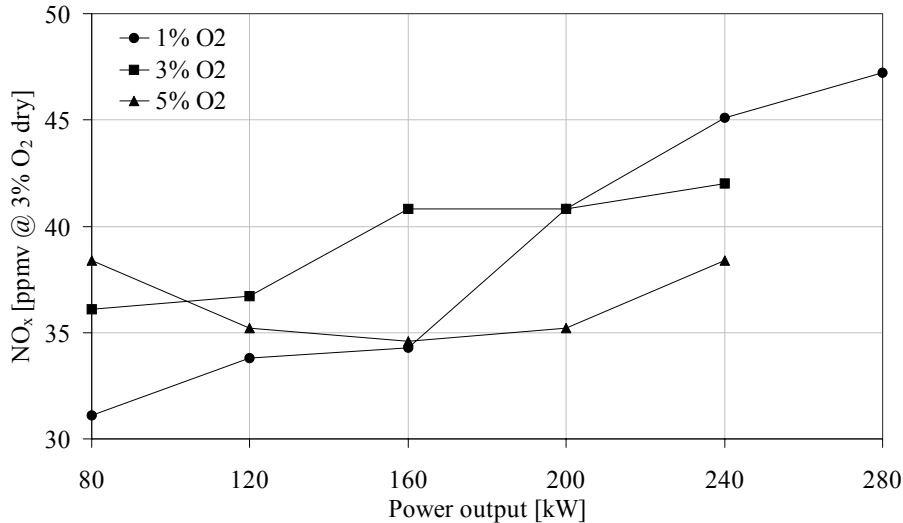
Figure 4–2 NO$_x$ emissions for propane as a function of power output at 1, 3 and 5% O$_2$ in the flue gases (Spangelo et al., 2003).

The effect of varying the swirl intensity on the NO$_x$ emissions and the fuel supply pressure in the Swirl Burner is presented in figure 4–3. It is seen that the NO$_x$ emissions are reduced with increasing swirl intensity. This illustrates the importance of the internal swirl-induced flue gas recirculation to keep the NO$_x$ emissions low. The same plot shows that while the NO$_x$ emissions are reduced with increased swirl intensity, this causes the pressure loss over the burner to increase at the same time, and a higher pressure on both fuel and air supply are therefore required.

NO$_x$ and CO emissions for the optimized propane and methane burners are compared in the plot in figure 4–4. A NO$_x$-reduction of about 50% can be gained by using methane instead of propane as fuel. According to Røkke et al. (1993) this fuel dependency on NO$_x$ is due to the prompt NO mechanism is less significant for methane as fuel and more significant for butane and heavier hydrocarbon fuels. It can also be seen from this plot that the emissions of CO are kept below 10 ppmv for both burners at the conditions tested.
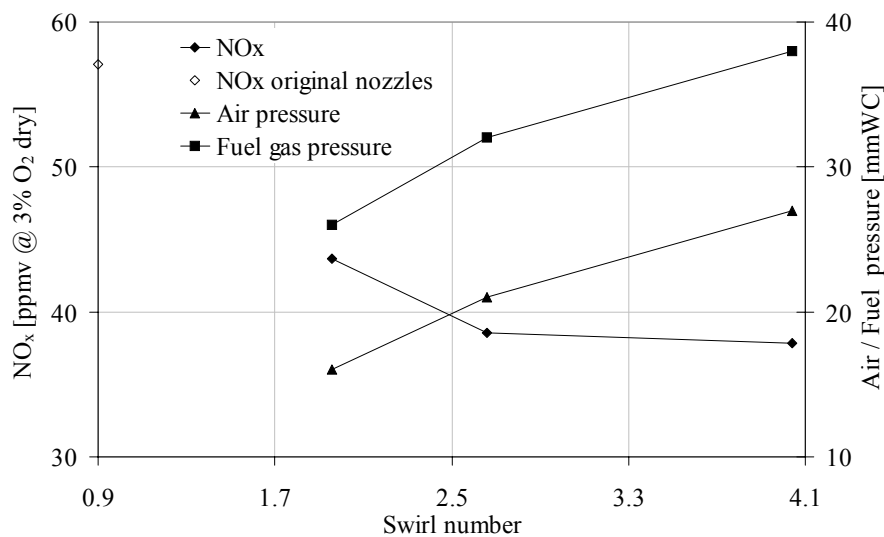
Figure 4–3 NO$_x$ emissions, fuel and air supply pressure as a function of the swirl number using propane as fuel at 120 kW power output (Spangelo et al., 2003).
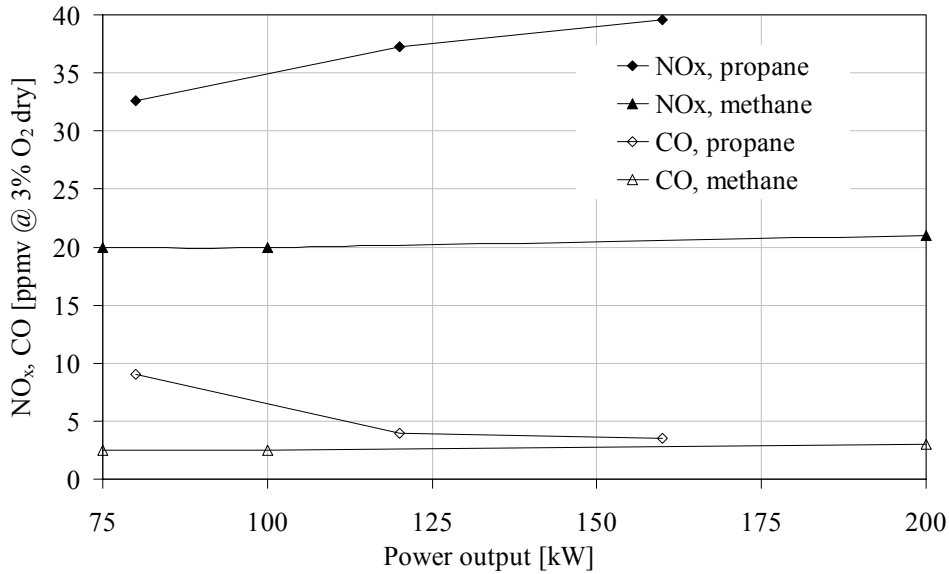
Figure 4–4 NO$_x$ and CO emissions as a function of power output and fuel, swirl number: S = 2.7 (Spangelo et al., 2003).

4.2 Scaling of the Swirl Burner

Having optimized the 200 kW Swirl Burner geometry as described in chapter 4.1 and appendix A, this burner was used as scaling basis to design a 20 kW and a 370 kW Swirl Burner. For this purpose the constant velocity scaling approach which has been described in chapter 2.3 and expressed in equation (2–12) was used. By inserting the burner exit diameter (d_0) into this equation, the other burner diameters are given as indicated in figure 4–5. The velocities considered important to keep constant were the combustion air velocity and the fuel gas velocity through the fuel gas nozzles. The gas tube diameter ($d_{gas\ tube}$) was therefore given the by the cross section area of the air supply annulus, not the area inside the gas tube. The exit angle of the swirl generator vanes was kept constant at 70°. This gives a swirl number (S) of about 2, which was chosen due to the increased air and fuel supply pressure with higher swirl numbers.

For the 20 kW Swirl Burner, the size and number of the fuel gas nozzles were determined experimentally and not theoretically by the constant velocity criteria. By varying the nozzle configuration while observing the NO$_x$ emissions and the burner stability, an optimum nozzle configuration was found experimentally for the 20 kW Swirl Burner design.
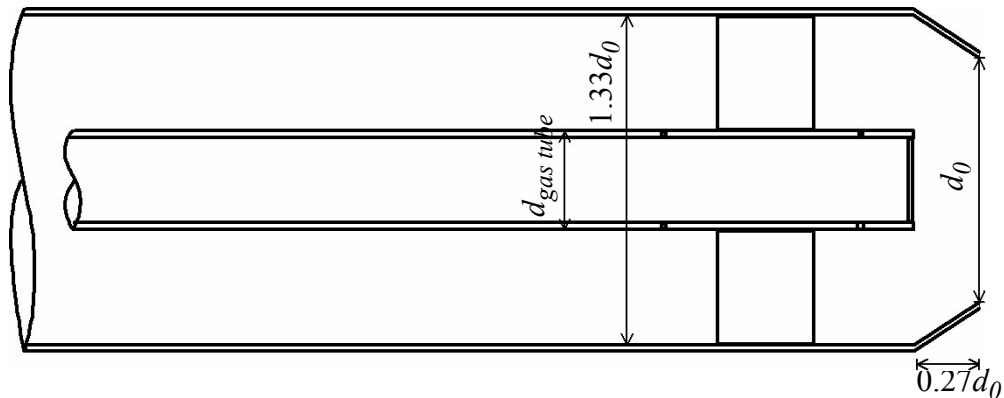
Figure 4–5 Main Swirl Burner dimensions as a function of the burner exit diameter, d_0.

The main dimensions for the 20 kW and the 370 kW burners resulting from the constant velocity scaling are given together with the dimensions for the 200 kW burner in table 4–1. Number and size of fuel nozzles positioned upstream and downstream the swirl generator are also given in this table as well as the swirl numbers resulting from an exit vane angle of 70° for the swirlers. The final burner dimensions were chosen not only from the scaling criteria, but also by considering the available constructing materials. For an easy and rapid manufacturing of the burners, standard sized tubes were used. This means for instance that instead of using a 31.6 mm diameter special made burner tube for the 20 kW Swirl Burner, a 34 mm diameter burner tube was used for convenience.

Table 4–1 Scaling parameters for the Swirl Burner.

Nominal Output	d_0	$d_{gas\ tube}$	u_{air}	Fuel nozzles upstream swirler	Fuel nozzles downstream swirler	Swirl number, S
200 kW	75 mm	30 mm	7.78 m/s	12x$\emptyset_{nozzle}$ 3.7 mm	12x$\emptyset_{nozzle}$ 3.7 mm	1.96
370 kW	102 mm	42 mm	7.83 m/s	12x$\emptyset_{nozzle}$ 5.0 mm	12x$\emptyset_{nozzle}$ 5.0 mm	1.96
20 kW	24.5 mm	13.5 mm	7.27 m/s	*8x$\emptyset_{nozzle}$ 1.5 mm	*24x$\emptyset_{nozzle}$ 1.5mm	2.04

* For the 20 kW burner the fuel nozzles were found experimentally.

4.3   Experiments with the scaled 370 kW Swirl Burner

The 370 kW Swirl Burner was tested using propane as fuel in the vertical boiler which is described in chapter 3.4. The main dimensions of this burner which were determined by the constant velocity scaling criteria, as described above, are summarized in table 4–1. For this burner the size and number of the fuel nozzles were determined by keeping the fuel gas velocity into the air supply the same as for the 200 kW Swirl Burner.

The burner has been tested with thermal throughput in the range 300 kW to 550 kW. This range is smaller than for the 200 kW Swirl Burner, which had a turndown ratio of 3:1 in the CEN boiler. The throughput tested with the 370 kW burner was limited both in the lower and the upper range by experimental reasons other than the burner itself. In the lower range, testing below 300 kW was found difficult due to the capacity of the combustion air fan used with this burner. The combustion air supply was adjusted by choking the air fan intake. Below 300 kW, choking the intake enough while keeping the air supply stable was not found possible. In the upper range, testing beyond 550 kW was not feasible due to the cooling capacity of the vertical boiler used in these experiments.

As seen from the graph in figure 4–6, the NO_x emissions at 3% O_2 in the flue gases were measured in the range from 40 to 44 ppmv corrected to dry conditions with the thermal throughput varying in the range 300 kW to 550 kW. It can also be seen that the NO_x emissions are increasing with increasing thermal throughput. This trend is similar to what is seen for the NO_x emissions measured with the 200 kW Swirl Burner (figure 4–1). The CO emissions were measured well below 10 ppmv dry during these experiments.

The burner was then tested for the effect of varying the excess air level on the NO_x and CO emissions while fuel supply was kept constant at 400 kW. These measurements were plotted and can be seen in figure 4–7. The NO_x emissions were now measured in the range from 34 to 43 ppmv corrected to dry conditions and 3% O_2. The NO_x formation is observed to be increasing with increasing amount of excess air. The CO emissions are measured well below 10 ppmv dry, except for the measuring point at 1% O_2 in the flue gas

where the CO measurement went off scale on the CO gas analyser. This means that the CO concentration in the flue gas is higher than 100 ppmv dry at an excess air level corresponding to 1% O_2. When measuring high emission values of CO, NO_x emissions are often found to decrease, as can be seen here. The trend of increasing NO_x emissions with increasing excess air level was also found for the 200 kW burner at 80 kW, while at 240 kW the opposite trend was found for the 200 kW burner. The 370 kW burner has only been tested for varying excess air at 400 kW.
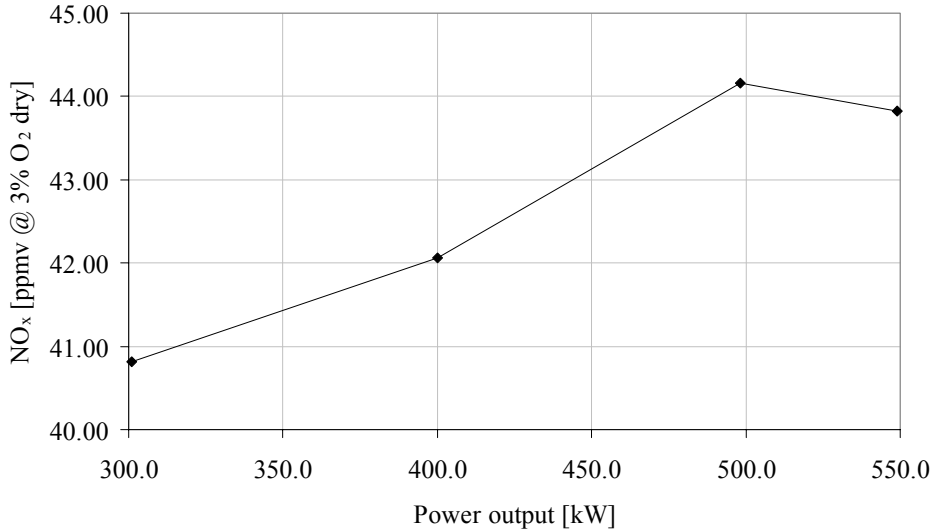
Figure 4–6 NO_x vs. power output, fuel: propane.
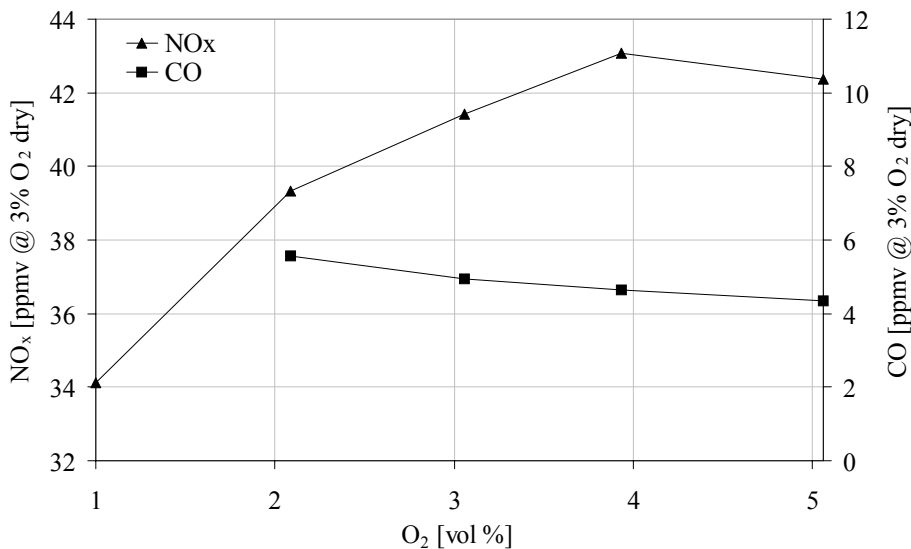
Figure 4–7 NO_x and CO vs. O_2 at 400 kW power output, fuel: propane.

4.4   Experiments with the scaled 20 kW Swirl Burner

The 20 kW Swirl Burner has been tested with both propane and methane as fuel. Experiments have been carried out in both an un-cooled combustion chamber and in a water-cooled combustion chamber. The latter is the combustion chamber with optical access that is described in chapter 3.5. The un-cooled combustion chamber is simply a 200 mm diameter vertical steel tube. There is no active cooling of this tube, but some heat is removed

by radiation and natural convection. While running burner experiments at high thermal throughput (> 10 kW) in the steel tube, its surface was glowing red. Results achieved from experiments in this combustion chamber can therefore not be directly compared with results from the other combustion chambers due to different conditions. Combined with the need for optical access to the flame inside the combustion chamber, this was the background for constructing and building the water cooled combustion chamber for burners up to 20 kW as described in chapter 3.5. Both methane and propane were used as fuel for the burner experiments in the un-cooled combustion chamber, while only propane was used as fuel for the experiments carried out in the optical water-cooled combustion chamber. For analysis of the flue gas composition from the un-cooled combustion chamber, the gas analyser set-up used with the CEN boiler and the vertical boiler was used.

The main dimensions of the 20 kW Swirl Burner were determined in the same way as with the 370 kW burner, by using the constant velocity scaling criteria. These dimensions are given in table 4–1. From this table it is seen that the air supply velocity in these three burners are the same, about 7-8 m/s.

The fuel nozzle configuration in this burner was determined experimentally instead of using the constant velocity scaling criteria for the nozzles. The background for this was an early theory for the Swirl Burner design, stating that having as many fuel gas nozzles downstream the swirl generator as possible was beneficial to reduce both the fuel supply pressure and the NO_x emissions. It was observed that with too many fuel nozzles downstream the swirler, the flame could not be ignited. The procedure for determining the fuel nozzles arrangement was by stepwise reducing the number of fuel nozzles, until the swirl flame could be ignited and stabilized by the burner. This procedure was carried out in the un-cooled combustion chamber. The resulting nozzle configuration for the 20 kW Swirl Burner had a fuel nozzle velocity of about half the corresponding velocities in the 200 kW and the 370 kW burners.

During testing, the 20 kW Swirl Burner flame was less stable than its 200 kW and 370 kW counterparts. At low flowrates of fuel and air (5-10 kW), the flame was very difficult or impossible to stabilize. This problem became even worse when moving the burner experiment to the water-cooled combustion chamber where more problems with flame stability and blow off were experienced. In this combustion chamber, lift off and subsequently blow off occurred at high flowrates when using propane as fuel. With methane as fuel, the flame could not be stabilized on the burner at all. Using propane, the flame blew off at about 17 kW, and at 5 kW the flame was unstable with high emissions of CO. The stability observations in both the un-cooled and the water-cooled combustion chamber with the 20 kW Swirl Burner are summarized in table 4–2.

Table 4–2 Stability observations of the 20 kW Swirl Burner.

Power Output	Un-cooled Chamber		Water-cooled Chamber	
[kW]	Propane	Methane	Propane	Methane
5	Unstable	No Flame	Unstable	No Flame
10	Stable	Unstable	Stable	No Flame
15	Stable	Stable	Stable	No Flame
20	Stable	Stable	No Flame (lift off at 17 kW	No Flame

NO_x emissions from the 20 kW Swirl Burner measured in the un-cooled combustion chamber using propane and methane as fuel are given in figure 4–8 and figure 4–9 respectively. With propane as fuel, NO_x emissions were measured from 32 to 45 ppmv dry corrected to 3% O_2 in the flue gases with the power output in the range 5 to 20 kW (figure 4–8). As seen from table 4–2, the burner was unstable at 5 kW with propane. The burner was also found unstable at low excess air (1% O_2 in the flue gases), and at 5 kW high levels of CO emissions were measured (30 ppmv dry) compared to the other measurements where CO was measured below 5 ppmv dry. This might explain the low NO_x measured at 5 kW and 1% O_2. Further, it can be seen that for the measurement series at 1% O_2 where the flame in general is quite unstable, emissions of NO_x versus power output do not follow the same trend as the more stable 3% O_2 and 5% O_2 measurement series (reduced NO_x emissions with increased power output). These trends are the opposite the findings for the 200 kW and the 370 kW Swirl Burner. This result will be further discussed and analysed in chapter 4.6.

When using methane as fuel in the un-cooled combustion chamber, NO_x emissions were measured in the range 18 to 25 ppmv dry corrected to 3% O_2 at 10 to 20 kW power output (figure 4–9). The flame stability was reduced with methane as fuel compared to propane. As seen from table 4–2, the burner could not be ignited below 10 kW power output, and at 10 kW the flame was very unstable and could only be ignited at high excess air (5% O_2). A weakly decreasing NO_x-trend with increasing power output might be identified for the 5% O_2 measurement series. Considering the experimental error of the NO_x analyser, the emissions of NO_x does not seem to change with power output for the methane measurements within this narrow range of stable operation. The CO emissions were measured below 5 ppmv dry when using methane as fuel. Both with propane and methane as fuel, the flame stability was increased when the excess air was increased.

As seen from table 4–2, in the water-cooled combustion chamber, the 20 kW Swirl Burner could not be ignited at all with methane as fuel. With propane, the burner was found less stable than in the un-cooled combustion chamber. Emissions of NO_x were therefore measured only with propane as fuel in this combustion chamber. In these measurements, which are plotted in figure 4–10, the emissions of NO_x were found to be in the range 16 to 35 ppmv dry corrected to 3% O_2. As seen from figure 4–10 and table 4–2, the power output was limited to the range 5 to 17 kW in these experiments. At 5 kW, the burner produced an unstable fluctuating flame with high CO emissions, while at increased power output emissions of CO were measured below 5 ppmv dry. As mentioned above, the flame blew off at 17 kW power output. To operate the burner at 17 kW, the excess air had to be increased to 7% O_2. At lower excess air, the flame blew off at even lower power output. The possible operating range with regard to power output and excess air in these experiments are represented by the data plotted in figure 4–10. From this plot it can also be seen that the measured emissions of NO_x are decreasing with increasing power output, similar as found for the 3% O_2 and 5% O_2 measurements in the un-cooled combustion chamber using propane as fuel. These trends are different from the trends found with the larger burners. As mentioned above, this result will be further discussed and analysed in chapter 4.6. The difference in the measured NO_x emissions for the 1% O_2, 3% O_2 and 5% O_2 measurement series is found to be within the measurement error of the NO_x analyser used.
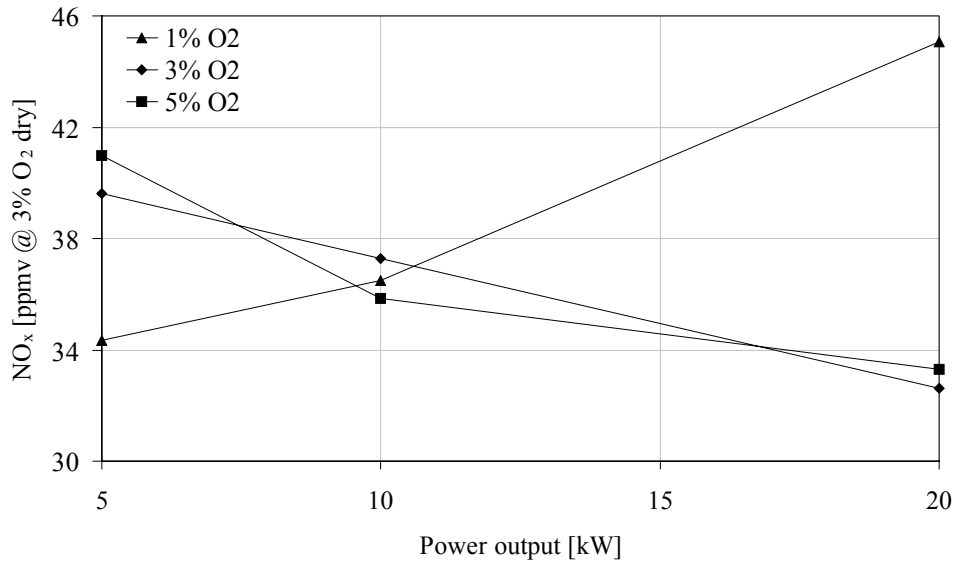
Figure 4–8 NO$_x$ vs. power output at various excess air levels (indicated as vol.% O$_2$ in flue gas) in an un-cooled combustion chamber, fuel: propane.
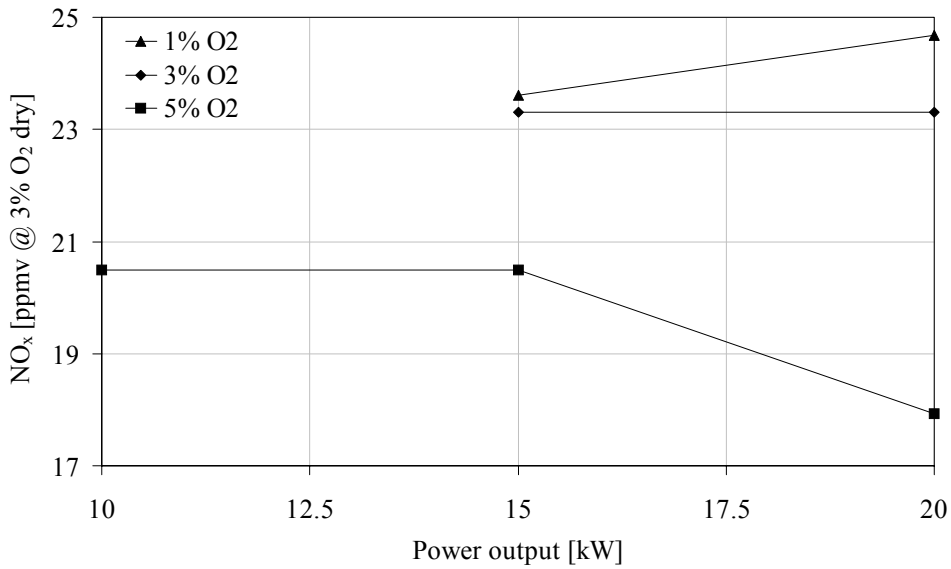
Figure 4–9 NO$_x$ vs. power output at various excess air levels (indicated as vol.% O$_2$ in flue gas) in an un-cooled combustion chamber, fuel: methane.
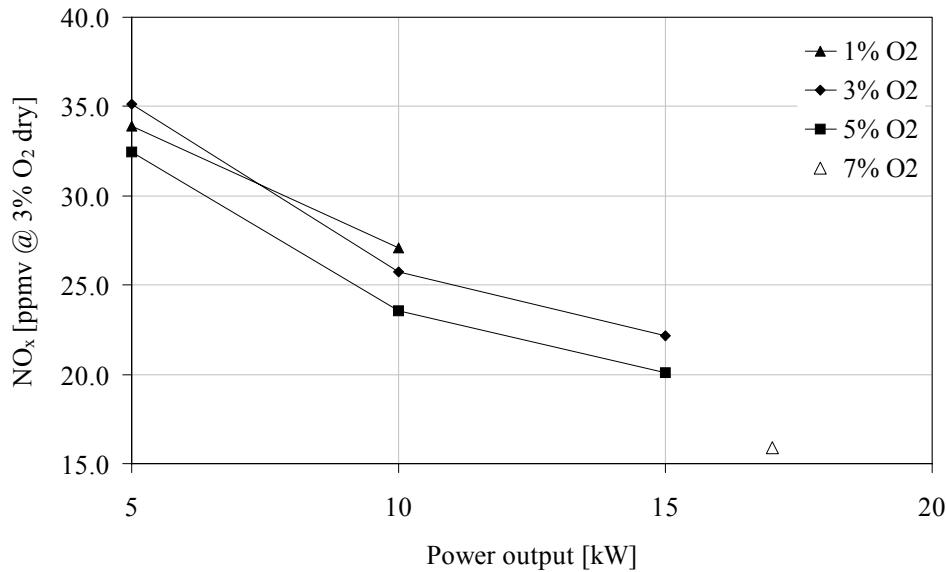
Figure 4–10 NO$_x$ vs. power output at various excess air levels (indicated as vol.% O$_2$ in flue gas) in the water-cooled combustion chamber, fuel: propane.

4.5 Non-intrusive measurements using Laser Induced Fluorescence

4.5.1 Correlation between OH concentrations and the measured OH LIF signal

Raw data from OH LIF measurements obtained with the experimental setup as described in chapter 3.7 (figure 3–13) consist in the light intensity incident at each pixel on the ICCD camera. This light consists of both background radiation and light emitted by the excited OH molecules present in the flame. The detected signal corrected for background radiation is proportional to the flame OH concentration. The raw data must be further processed to evaluate the absolute OH concentrations in the flame. For this purpose a correlation between the raw LIF data and the OH mole fraction is needed. This was found by comparing the LIF signal from a McKenna laminar flat flame burner with the theoretical OH profile through a laminar premixed flame calculated using the computer program Premix (Kee et al., 1985) as already described in chapter 3.7.

The temperature profile measured in the McKenna burner was corrected for radiation losses using equation (3–3) with emissivity, $\varepsilon = 0.22$ (Kyne, 2001), and bead diameter including coating, $d = 0.35$ mm. Velocities to calculate the *Nu*-number in equation (3–3) were achieved from an iteration between equation (3–3) and Premix which calculates velocities, density and gas composition in the flame (Kee et al., 1985). The corrected temperature profile is plotted in figure 4–11. The inaccuracy of the corrected temperature due to the emissivity of the coated thermocouple, is difficult to determine. An error of ±50K has been assumed for the corrected temperature profile, but this error might be greater.
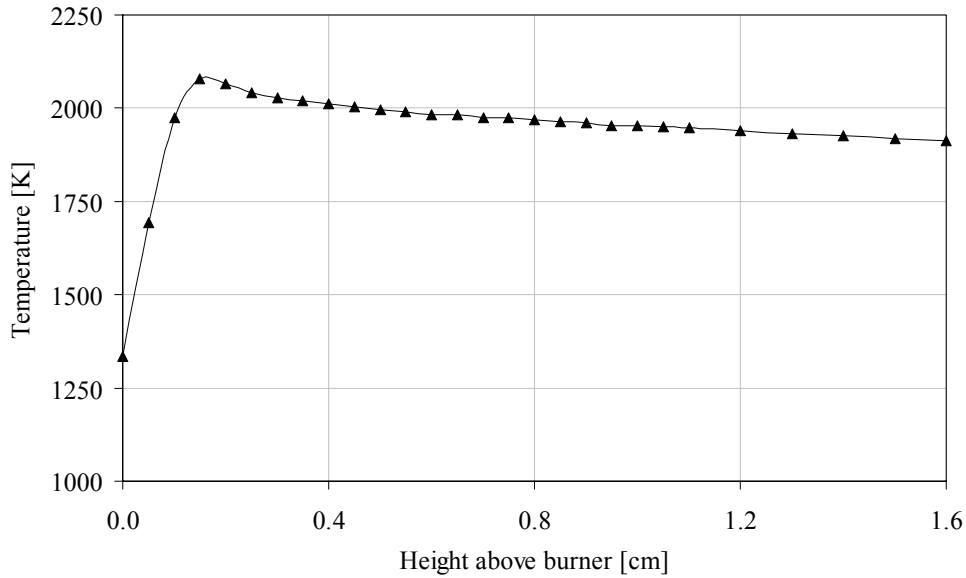
Figure 4–11 Radiation-corrected temperatures measured in the Mckenna burner, ε = 0.22.

The radiation-corrected temperature profile was used as input to the final Premix calculation to determine the theoretical OH concentrations in a one-dimensional, laminar, premixed flame (Kee et al., 1985) using the Leeds Methane Oxidation Mechanism v. 1.5 (Hughes et al., 2001) as database. The initial mesh used for this calculation consisted of 28 grid points distributed over a computational domain from 0.0 to 16.0 mm above the burner. After convergence, the mesh had been refined by the program to 61 grid points. The mass flow rate of reactants was set to 0.0072 g cm^{-2} sec^{-1}, and the inlet composition of methane (CH_4) and air (O_2 and N_2) corresponded to λ = 1.439 at a pressure of 1 atmosphere. Further details on this calculation can be found in appendix B where the input-file to this computer program is quoted. An error of ±12% on the calculated OH concentrations was found for the temperature measurement error assumed above.

The theoretical OH-profile could now be compared with the OH LIF raw signal measured at the centre of the McKenna burner. The calculated OH mole fractions were plotted against the raw OH LIF signal as seen in figure 4–12. From this plot, a linear function of the OH mole fraction as a function of the measured OH LIF signal was found. The OH mole fraction (X_{OH}) measured with this experimental setup is given by the following correlation:

$$X_{OH} = 5 \times 10^{-06} \times I_{OH} + 0.0012 \qquad (4–1)$$

Where I_{OH} is the background radiation corrected light intensity detected by the ICCD camera which originates from the laser induced OH fluorescence. The least error of the calculated OH mole fractions in equation (4–1) will be the error related to the temperature measurements, here assumed to be ±12% on the mole fraction. Further errors might be systematic errors in the OH LIF measurements as mentioned in chapter 3.7. In total, it might be reasonable to expect a total error in the range 12-20% for equation (4–1). By applying equation (4–1) to the OH LIF measurements made in the flame above the McKenna burner, a 2D plot of the OH mole fractions can be produced as seen in figure 4–13.
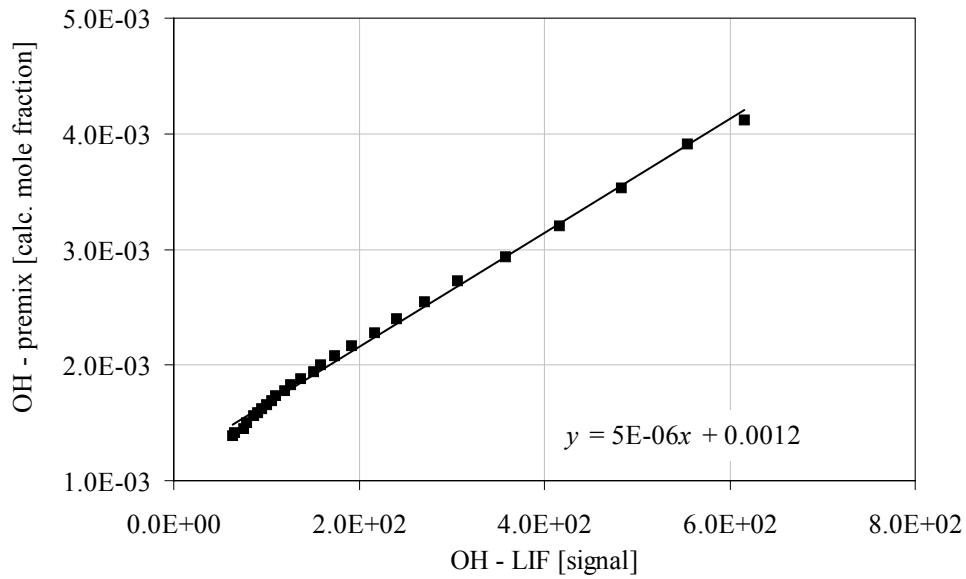
Figure 4–12 OH LIF raw signal vs. OH mole fractions calculated using Premix (Kee et al., 1985).

In figure 4–13, it can be seen that the area of high OH concentration in this flat flame is wedge-shaped. The laser beam enters the flame from the right at the thick end of the wedge. This wedge-shape is believed to originate from attenuation of laser intensity along the beam-path through the flame. To account for this attenuation, a linear correction was applied to reduce the calculated OH mole fraction at the right side of the burner where the beam enters the flame, and to increase it at the left side of the burner where the beam exits the flame. At the centre of the burner, no correction was applied. The result of this correction can be seen in figure 4–14. The flame is now represented as flat and the OH mole fraction changes only with height above the burner. This correction will be applied to all OH LIF measurements made with this experimental setup.
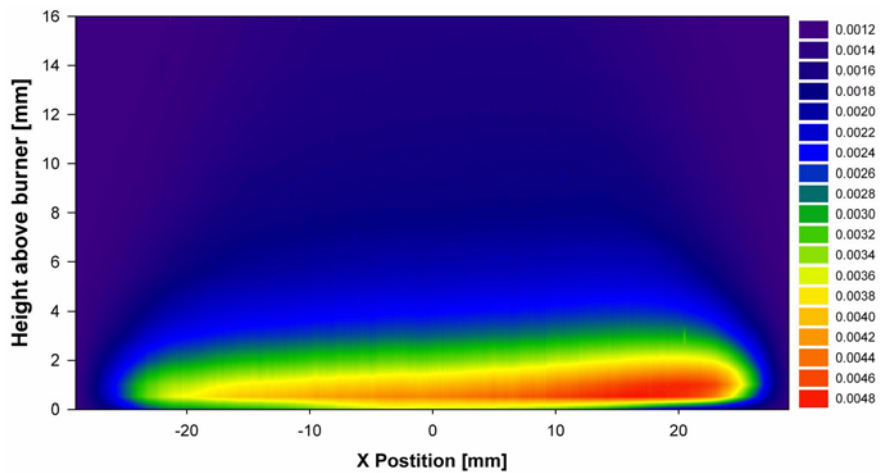
Figure 4–13 OH mole fractions in flat flame above McKenna premix burner with methane and air (λ = 1.439). Mole fractions not corrected for laser intensity attenuation through flame.
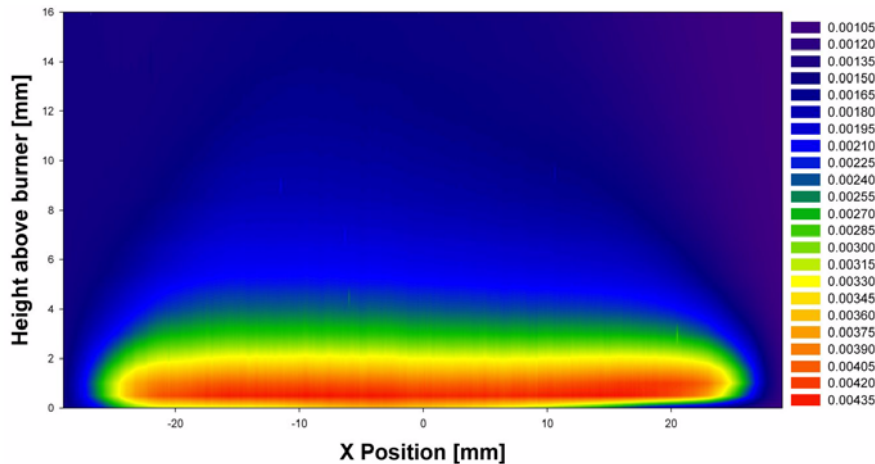
Figure 4–14 OH mole fractions in flat flame above McKenna premix burner with methane and air (λ = 1.439). Mole fractions corrected for laser intensity attenuation through flame.

4.5.2   OH LIF measurements in the Swirl-Burner

Having found the correlation to derive OH mole fractions from the measured OH LIF raw data in equation (4–1), experiments to measure OH concentrations in the 20 kW Swirl Burner could be carried out. For these experiments, the water-cooled combustion chamber with optical access was used. A description of this combustion chamber can be found in chapter 3.5. It was found, as described in chapter 4.4, that the flame could not be stabilized in this combustion chamber using methane as fuel. The OH LIF measurements were therefore made using propane as fuel. Measurements of NO_x emissions from the 20 kW Swirl Burner in this combustion chamber are described in chapter 4.4 and can be found plotted in figure 4–10.

OH mole fractions derived from the OH LIF data using equation (4–1) were used to construct 2D contour plots of the OH concentrations in the Swirl Burner. OH flame concentrations at thermal throughputs of 5 kW, 10 kW and 13 kW with excess air corresponding to 3% O_2 in the flue gases are shown in figure 4–15, figure 4–16 and figure 4–17 respectively. To avoid possible stability problems at higher thermal throughput, a maximum of 13 kW was used in the laser measurements.

From the OH-plots in figure 4–15, figure 4–16 and figure 4–17, it is seen that the peak OH mole fraction at 5 kW and 10 kW is measured to be around 0.0050 (0.0056 and 0.0052 respectively), while at 13 kW it is measured to be 0.0038 which is about two-thirds of the value measured at 5 kW and 10 kW. The change in peak OH concentration at 13 kW might be caused by the flame lifting off during measurements. This behaviour will change the flame conditions during capturing the OH measurement which can cause measurement inaccuracies. Since the OH laser induced fluorescence and the background radiation were measured separately, a slight change in flame conditions would alter the final OH mole fraction derived from these measurements.

It can be seen from figure 4–14, that the OH contour plot of the laminar flame above the McKenna burner has a sharp and defined shape, while the turbulent Swirl Burner flames in figure 4–15 to figure 4–17 appear more blurred due to turbulent fluctuations. Since the OH plots are constructed from averaged and not instantaneous OH measurements, turbulent fluctuations will make the OH plots appear increasingly blurred with increased turbulence intensity. The dark horizontal lines of low OH-concentration seen at the top of the 5 kW and the 13 kW flames in figure 4–15 and figure 4–17 respectively, might also be a result of the averaging of the OH measurements. A fluctuating flame "tail" might have

caused such lines as seen in these OH contour plots.

In flames, OH radicals are present in both the burned gases and in the flame front. According to Gülder et al. (2000), the flame front can be identified where the spatial OH gradient is highest. By applying this, the OH contour plots in figure 4–15, figure 4–16 and figure 4–17 can be used to give an indication of the flame front location, and it can be seen that the flame volume is reduced with increasing thermal throughput. At 5 kW the flame stretches from 20 mm to 105 mm above the burner exit including the flame "tail", while at 10 kW and 13 kW the OH plots indicate that the flame stretches from 5 mm to 70 mm above the burner exit and 25 mm to 65 mm above the burner exit including the flame "tail" respectively.

The reduction in flame volume with increased thermal throughput might cause a reduction in residence time for the combustion gases in the flame, which in turn will result in a decrease of thermal NO formation. Assuming the lower OH concentrations found for the 13 kW flame are not due to measurement errors, indicates lower flame temperatures in this flame since the OH radical concentrations will be higher at higher temperatures. This corresponds with the NO_x measurements presented in figure 4–10 where the NO_x concentrations were found to decrease with an increase in thermal throughput.
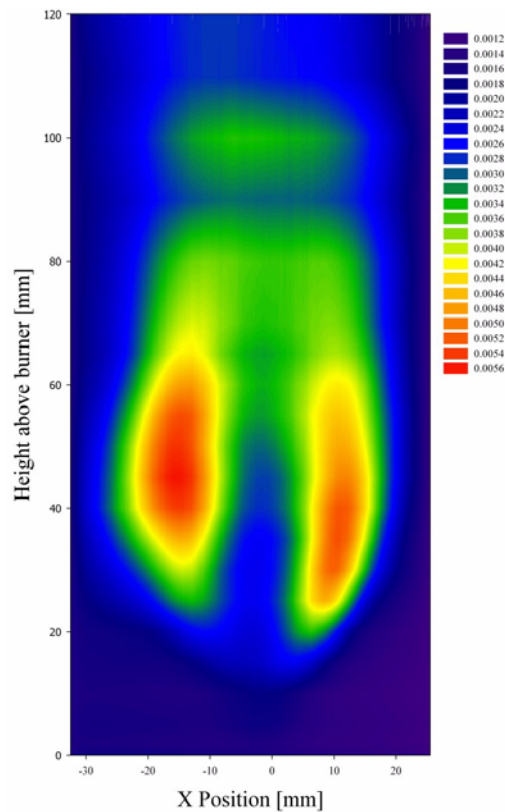
Figure 4–15 OH mole fractions in Swirl Burner using propane as fuel, 5 kW @ 3% O2.
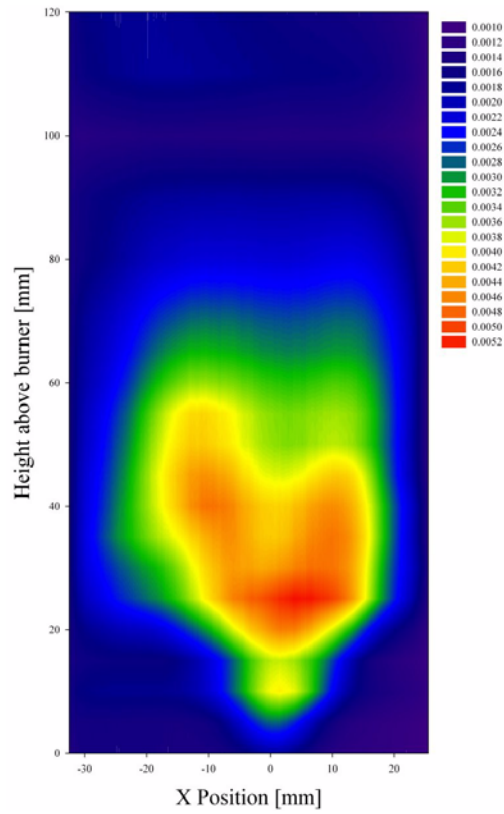
Figure 4–16 OH mole fractions in Swirl Burner using propane as fuel, 10 kW @ 3% O2.
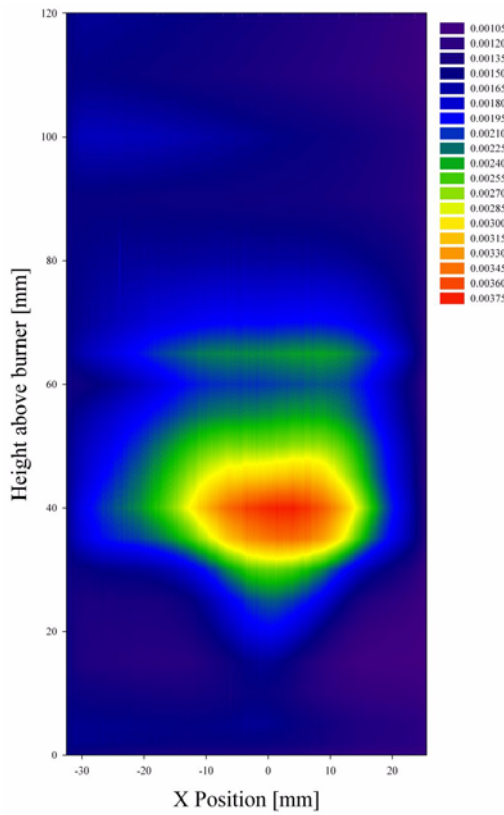
Figure 4–17 OH mole fractions in Swirl Burner using propane as fuel, 13 kW @ 3% O2.

4.5.3 Temperature measurements with LIF

The possibility for measuring flame temperatures using the current OH LIF setup as described in chapter 3.7 has been investigated. By measuring the emitted light intensity from two transitions of the OH $A^2\Sigma^+$ - $X^2\Pi_i$ (1,0), temperatures can be found from the intensity ratio. This technique was applied by Meier et al. (2000) for temperature measurements in a combustor using two lasers tuned to the $Q_1(1)$ and the $Q_1(11)$ OH transitions. The setup described in chapter 3.7 consists of only one laser which can be tuned to one transition at a time to find the intensity ratio. This means that the flame must be stable and all conditions are assumed to be independent of time.

Two different transition ratios were studied in order to measure the flame temperatures. These were the $Q_1(3)$ to $R_1(13)$ intensity ratio and the $Q_{21}(3)$ to $R_1(13)$ intensity ratio which are found close to each other in the OH LIF emission spectrum as seen in figure 4–18. By calculating the OH emission spectra at different temperatures using LIFBASE (Luque and Crosley, 1999), the intensity ratios at various temperatures could be found. The $Q_1(3)$ - $R_1(13)$ intensity ratio and the $Q_{21}(3)$ - $R_1(13)$ intensity ratio were plotted against temperature as seen in figure 4–19 and figure 4–20 respectively. By line-fitting these plots, an equation was found for the temperature, T, as a function of the emission intensity ratio, I, for each transition ratio. The line-fitted equations are given by equation (4–2) and equation (4–3) for the $Q_1(3)$ - $R_1(13)$ intensity ratio and the $Q_{21}(3)$ - $R_1(13)$ intensity ratio respectively.

$$T = 547.56934\exp(-I/60.03044) + 2946.91591\exp(-I/1.97786) \qquad (4–2)$$
$$+ 972.17267\exp(-I/8.8741)) + 758.98184$$

$$T = 547.5569\exp(-I/12.65327) + 2945.74213\exp(-I/0.41694) \qquad (4–3)$$
$$+ 972.10723\exp(I/1.87054) + 758.97823$$
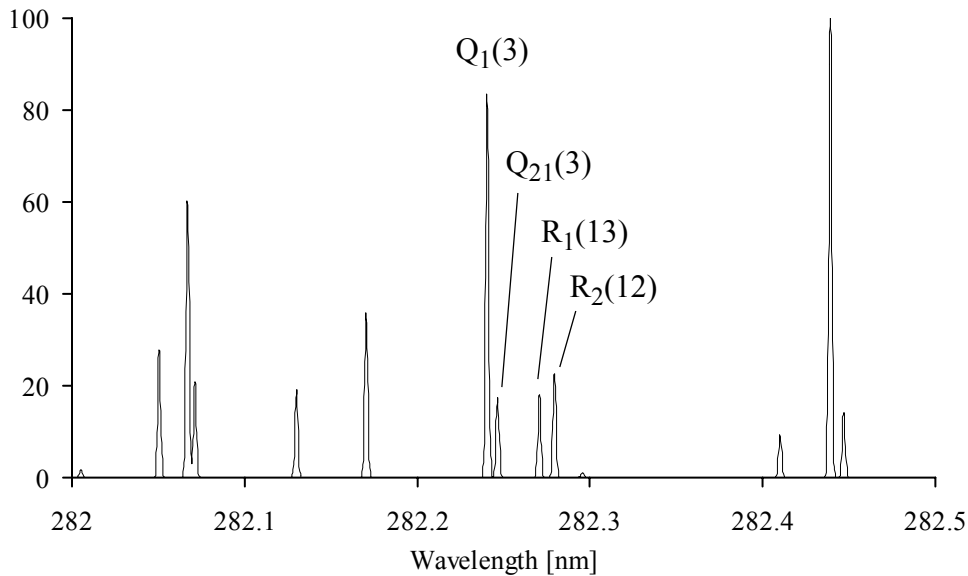
Figure 4–18 OH LIF emission spectrum from 282.0 nm to 282.5 nm at 2000 K.
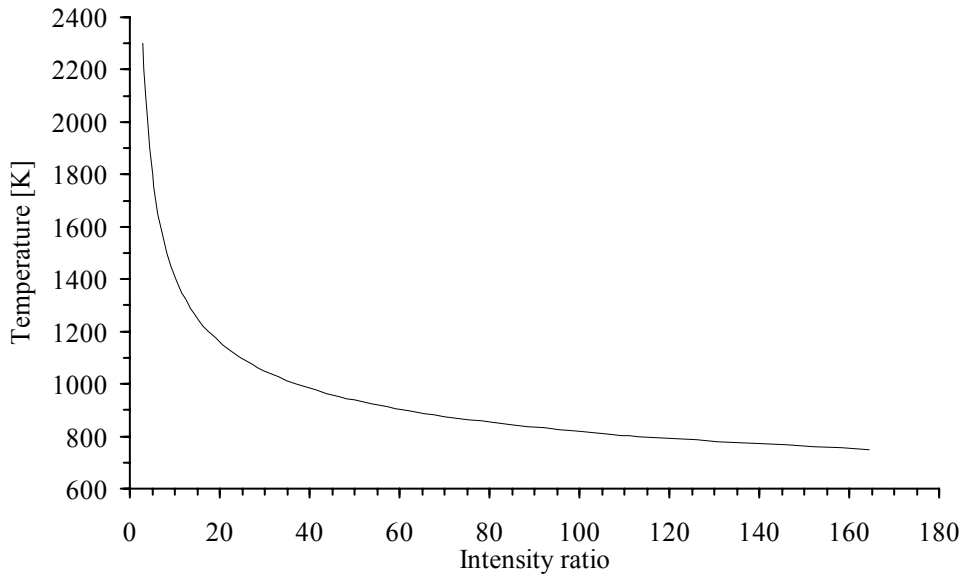
Figure 4–19 $Q_1(3)$ to $R_1(13)$ emission intensity ratio vs. temperature.
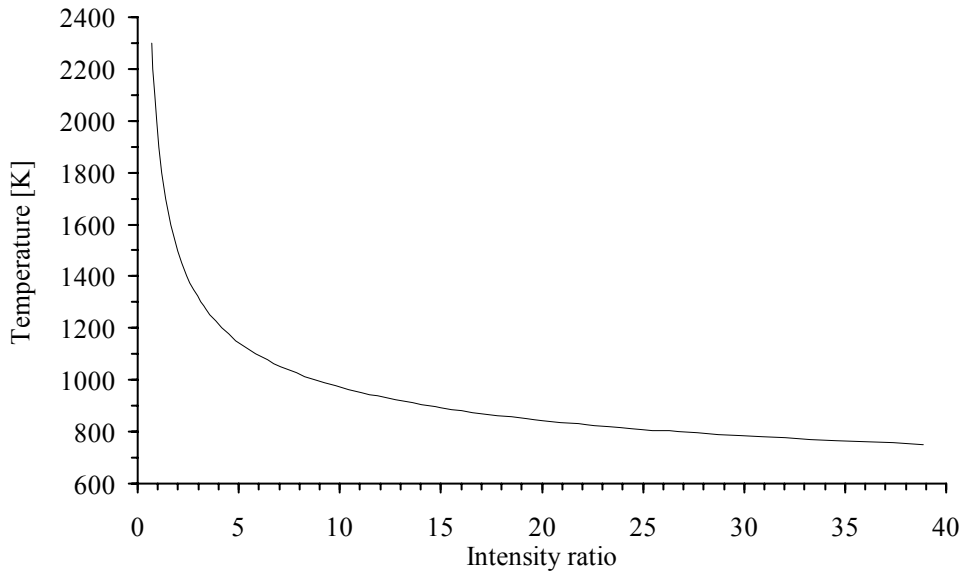
Figure 4–20 $Q_{21}(3)$ to $R_1(13)$ emission intensity ratio vs. temperature.

The temperature measurements were made using the McKenna burner. This burner provided a very stable, flat premixed laminar flame. The measured intensity ratios at different heights above this burner were used to calculate a temperature profile through the flame using equation (4–2) and equation (4–3). The resulting temperature profiles found with this LIF technique were plotted and can be seen in figure 4–21. In this plot, a temperature profile measured in the same flame using a thermocouple corrected for radiation losses can also be found plotted. It can be seen that the temperatures found from the OH LIF measured $Q_1(3)$ - $R_1(13)$ intensity ratio and $Q_{21}(3)$ - $R_1(13)$ intensity ratio are much lower than the temperatures found with the thermocouple.

The differences in temperatures measured by thermocouple and the OH LIF technique can be caused by small changes in flame conditions during the measurements of light intensity from the different transitions which were not made simultaneously. Measurement inaccu-

racies might also be caused by the dye laser calibration which is described in chapter 3.7. While calibrating the dye laser, it was sometimes found difficult to separate the $Q_1(3)$ transition from the $Q_{21}(3)$ transition and the $R_1(13)$ transition from the $R_2(12)$ transition. If the laser is not properly tuned into the transitions considered, the intensity ratios found will be incorrect. For temperatures in the range 1000-2000 K, it can be seen from figure 4–19 and figure 4–20, that small deviations in the intensity ratios will cause great deviations in the flame temperatures found. Due to this result, as seen in figure 4–21, the current LIF setup was not found to be suitable for temperature measurements with this technique.
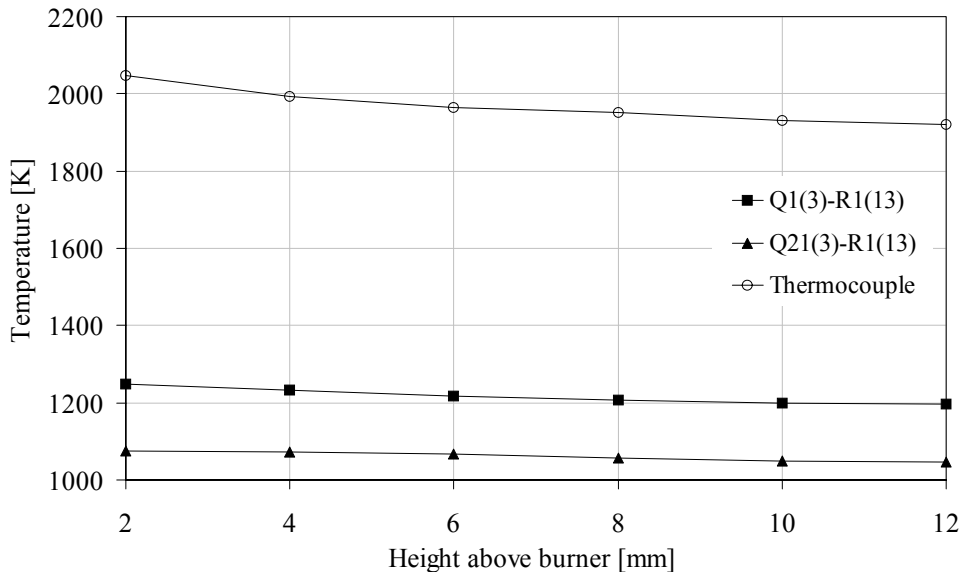
Figure 4–21 Temperature measurements in laminar flat flame above Mckenna premix burner made by the OH LIF technique and by thermocouple.

4.6 Analysis and discussion of experimental results

4.6.1 Scaling

The 200 kW Swirl Burner has been used as a basis for scaling to a 370 kW and a 20 kW burner. The 200 kW burner was first extensively tested and optimized to find the best burner geometry for low emissions of NO_x while keeping the air and fuel supply pressure low (Spangelo et al., 2003). The latter is important due to possible capacity limitations of the air fan used with this type of burners.

The 200 kW burner was tested with various swirl numbers, from 2 to 4, showing that the formation of NO_x was reduced with increased swirl intensity while the pressure on the air and fuel supply was increased with increasing swirl intensity. The reduced NO_x formation is related to the internal flue gas recirculation which is increased with higher intensity of swirl. The flame temperature is then reduced by addition of inert flue gas into the flame, hence reducing the formation of thermal NO. The combustion air flow is obstructed by the swirl generator and by increasing the swirl vane angle, the pressure drop over the swirler is increased. As seen in figure 4–3, the air supply pressure is reduced by about one third when reducing the swirl number from 4 to 2. To avoid the combustion air fan becoming too small for the Swirl Burner, the swirl number was kept at about 2 when scaling the burner to 370 kW and 20 kW.

The burner main dimensions were scaled using the constant velocity criteria as described in chapter 2.3, where the velocities of fuel and air in the burner are kept constant. This criteria was not applied for the fuel nozzles of the 20 kW Swirl Burner which was found experimentally as described in chapter 4.4. As a result of this, the fuel to air momentum ratio is not preserved in the 20 kW burner. According to Weber (1996), this is an important parameter for achieving flow pattern similarity in scaled burners. To preserve the fuel to air momentum ratio from the 200 kW to the 20 kW burner, the fuel nozzle velocities in the 20 kW burner must be increased. This can be achieved by reducing the number of fuel nozzles, a procedure that was found to increase the burner stability of the 200 kW burner (Spangelo et al., 2003). The 370 kW burner was scaled with the constant velocity criteria applied for the fuel nozzles as well. This burner was operated without any burner instabilities observed and the emissions of NO_x were found to increase with power output and the level was measured in the same range as with the 200 kW burner. The fuel to air momentum ratio must therefore be seen as an important parameter for the Swirl Burner that must be remained constant when scaling the burner.

Burner experiments as described in the previous chapters show that the NO_x emissions measured from the different scaled burners behave somewhat different. The 200 kW Swirl Burner NO_x emissions are found in the range 32 to 43 ppmv dry, and as seen from figure 4–1, these emissions characteristically increase with increasing power output. The same trend is seen for the 370 kW burner in figure 4–6. For the smaller 20 kW Swirl Burner though, the NO_x emissions follows a different trend. As seen from figure 4–8 and figure 4–10, where propane is used as fuel in an un-cooled and a water-cooled combustion chamber respectively, emissions of NO_x follow a trend of decreasing NO_x with increasing power output apart from the 1% O_2 test series in the un-cooled combustion chamber. In addition, the 20 kW burner is found to be very unstable compared to the other burners, and has a limited range of stable operation (table 4–2).

For comparison of the measured NO_x emissions from the different Swirl Burners, a flamelet-based correlation for the scaling of NO_x emissions from diffusion flames proposed by Røkke et al. (1992) is applied. The correlation, quoted in equation (2–9), is based on the derivation of explicit expressions for local instantaneous NO production rates using 14 elementary steps in a two-reaction-zone laminar flamelet model. Emissions of NO_x from diffusion flames were found to scale with $Fr^{0.6}$ which was proportional to the flame volume. Weber (1996) later expanded this correlation for complex burners enclosed in boilers with various amount of heat extraction (HE). Al-Fawaz et al. (1994) has also successfully applied the correlation to complex burners enclosed in a boiler. The original correlation from Røkke et al. (1992) and the expansions by Weber (1996) are summarized in table 4–3. Measured NO_x emissions from the Swirl Burners were expressed as EI_{NOx}, the emission index of NO_x in g NO_x/kg fuel, which can be calculated by the following equation:

$$EI_{NOx} = \frac{n[NO_x]MW_{NO_2}1000}{[CO_2]MW_{C_nH_m}}\left[\frac{\text{g } NO_x}{\text{kg fuel}}\right] \tag{4–4}$$

Where n is the number of carbon atoms in the hydrocarbon fuel, [] denotes the mole fraction of NO_x and CO_2 and MW is the molecular weight of NO_2 and the hydrocarbon fuel. The equation is based on the assumption that all the carbon atoms in the fuel are oxidized to CO_2 and the NO_x is represented by NO_2. The Froude numbers for the burners were calculated using an equivalent area diameter single-jet similarity for the fuel nozzles of the burners (Al-Fawaz et al., 1994). This diameter, d_0, and the fuel jet velocity, u_0, through

the fuel nozzles were used to calculate the Froude numbers, $Fr = u_0^2/d_0g$. All burner experiments could now be compared by plotting the Froude number against the EI_{NOx} multiplied by ρ_0u_0/d_0 for each measurement. This plot can be seen in figure 4–22. The original correlation suggested by Røkke et al. (1992) and the extended correlations suggested by Weber (1996) for 30% to 60% heat extraction are shown as straight lines in the same plot.

Table 4–3 Correlations for $EI_{NOx}\,\rho_0\,u_0\,/\,d_0$.

Røkke et al. (1992)	$44Fr^{0.6}$
Weber (1996), 30% HE	$34.8Fr^{0.6}$
Weber (1996), 40% HE	$23.2Fr^{0.6}$
Weber (1996), 50% HE	$14.5Fr^{0.6}$
Weber (1996), 60% HE	$7.5Fr^{0.6}$
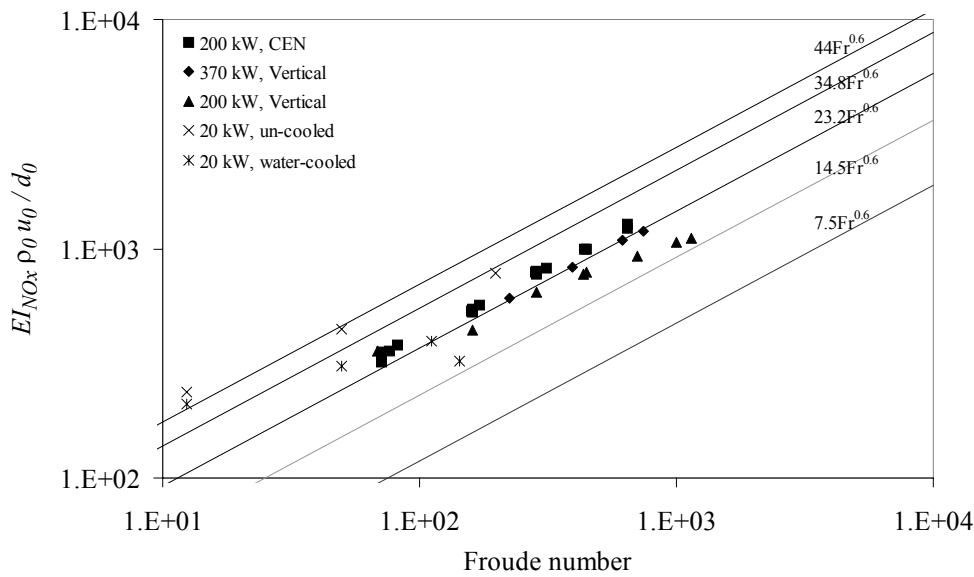
Figure 4–22 Correlations for NO_x emission index plotted together with the experimental data from the Swirl Burners.

From the plot in figure 4–22, it is seen that the NO_x emissions measured from the Swirl Burners in different boilers fits quite well into the NO_x emission correlation expanded by Weber (1996) for complex burners enclosed in combustion chambers. For both the 200 kW burner in the CEN boiler and the 370 kW burner in the Vertical boiler, the measured NO_x emissions are found close to or on the $23.2Fr^{0.6}$ line which corresponds to 40% heat extraction according to Weber (1996). With the 20 kW burner, NO_x emissions measured in the un-cooled combustion chamber partly follows the original correlation (Røkke et al., 1992), the $44Fr^{0.6}$ line, but at increased Froude number which corresponds to the highest thermal throughput for this burner (20 kW), the measured NO_x is found to be lower than

expected from the $44Fr^{0.6}$ line. This implies that the heat extraction from the flame is higher at 20 kW power output than at lower power output. In the water-cooled combustion chamber, NO_x emissions measured from the 20 kW burner does not fit into the Froude number correlation as good as emissions from the other burners. The plotted data for this burner and boiler combination are not parallel to any of the $Fr^{0.6}$ lines in the plot, but are found scattered between the $14.5Fr^{0.6}$ and $44Fr^{0.6}$ lines. As for the measurements in the un-cooled chamber, this suggests that the heat extraction from the flame is increasing with increasing power output, and according to Weber (1996), reaches a maximum of about 50% heat extraction at the highest power output (17 kW).

The NO_x scaling correlation by Røkke et al. (1992) was derived assuming that the leading-order parameter for NO_x formation was the flame volume which was found to be proportional to $Fr^{0.6}$. According to Weber (1996), heat extraction from flames will cause reduction of the flame volumes. The experiments presented here show that the correlations holds for the 200 kW Swirl Burner in the CEN boiler and the 370 kW Swirl Burner in the Vertical boiler, indicating that the leading order for NO_x formation in these burners is the flame volume as found for diffusion flames (Røkke et al., 1992) and other complex burners (Al-Fawaz et al., 1994, Weber, 1996). Assuming the flame volume is the leading-order parameter for NO_x formation, implies that the 20 kW burner flame volume is not proportional to $Fr^{0.6}$. Røkke et al. (1992) computed the diffusion flame volume as a cylinder from the flame height and the averaged radius which both were found to be proportional to $Fr^{0.2}$. From the 20 kW data plotted in figure 4–22 it can be found that a line parallel to $Fr^{0.4}$ better fits the measured NO_x emissions from the 20 kW Swirl Burner, implying that the flame volume is not scaled by the same Froude number correlation as the bigger burners.

Weber (1996) stated that the confinement ratio (boiler to burner diameter ratio, d_{boiler}/d_0) was of secondary importance when scaling burners if kept higher than 3 for the burners in their study ("Scaling 400 project"). A minimum confinement ratio is required to enable the entrainment of combustion products into the flame by internal flue gas recirculation. For the Swirl Burner, the internal flue gas recirculation is important for both keeping the emissions of NO_x low and for flame ignition and stabilization. A too narrow boiler might disturb the flame flow pattern and alter the flue gas recirculation. The confinement ratios for the different burner and boiler configurations tested here are summarized in table 4–4. The burners that were operated without stability issues and NO_x emissions measured to fit the $23.2Fr^{0.6}$ line in figure 4–22, namely the 200 kW burner in the CEN boiler and the 370 kW burner in the Vertical boiler, have a confinement ratio of respectively 5.33 and 6.72. For the 20 kW burner in the water-cooled laser-chamber or in the un-cooled chamber this ratio is 8.16. The 20 kW burner is found to be more unstable and the NO_x emissions are found not to be proportional to $Fr^{0.6}$.

Table 4–4 Confinement ratio for various burners and combustion chambers.

Burner	200 kW	370 kW	20 kW	200 kW
Combustion chamber (D_{boiler})	CEN (400 mm)	Vertical (686 mm)	Laser-chamber (200 mm)	Vertical (686 mm)
D_{boiler}/D_0	5.33	6.72	8.16	9.15

The effect of increasing the confinement ratio on the emissions of NO_x was studied closer by running the 200 kW Swirl Burner in the Vertical boiler, where the confinement ratio for this burner was 9.15. In figure 4–23, NO_x emissions measured with this burner in the Vertical boiler are compared with NO_x emissions from the same burner measured in the

CEN boiler. From these results it can be seen that the NO_x emissions are characteristically increasing with increasing power output in the CEN boiler, while in the Vertical boiler the NO_x emissions are lower and decreasing with increasing power output. These measurements are also plotted in figure 4–22 as EI_{NOx} against the Froude number together with the other burner measurements. It can be seen that the measured NO_x emissions with this burner in the Vertical boiler are not parallel with any of the $Fr^{0.6}$ lines in figure 4–22, the same as previously found for the 20 kW burner.
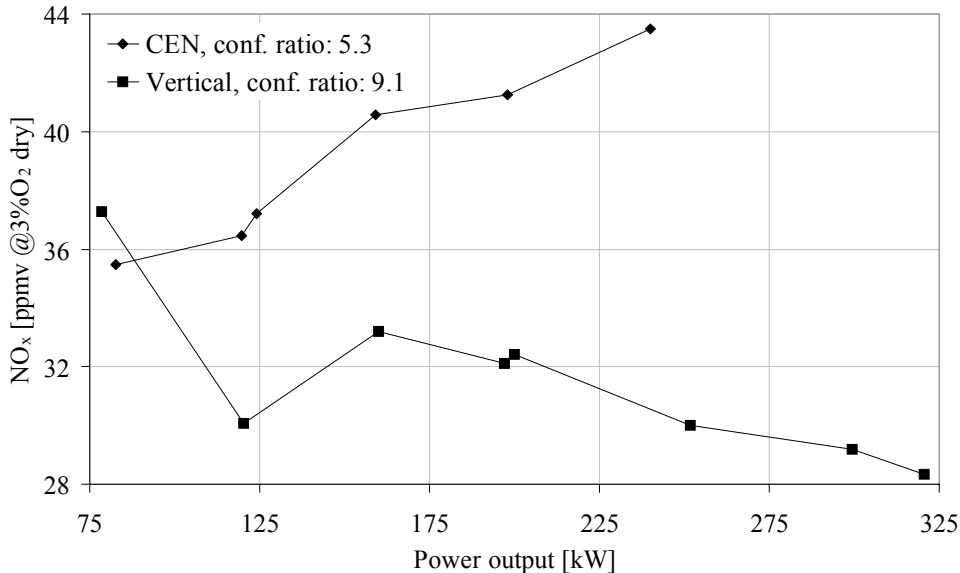
Figure 4–23 NO_x measured in the CEN boiler and the Vertical boiler with the 200 kW Swirl Burner.

In the Vertical boiler, the burners are directed downwards. Due to buoyancy this might cause a reduction in flame volume compared to a horizontally directed burner. Since the same trend with decreasing NO_x with increasing power output was found with the upwards directed 20 kW burner where buoyancy will have the opposite effect on flame volume, buoyancy alone are not assumed to account for the change in NO_x trends found for the 200 kW burner in figure 4–23.

To increase the confinement ratio with the same burner, the combustion chamber diameter and hence the volume must be increased. According to Sayre et al. (1994), most of the heat extraction from a flame confined in a boiler takes place in the post-flame region by both radiation (mainly) and convection. The amount of heat extracted in the post-flame region will affect the flame temperature due to the internal flue gas recirculation entraining combustion products into the flame. As a result, the amount of heat extracted in the post-flame region will alter the NO_x-formation and the flame stability. By increasing the combustion chamber diameter, the post-flame radiative and convective heat transfer from the combustion products to the colder combustion chamber walls will be increased. This might cause the reduced NO_x-formation seen in figure 4–23 for the higher confinement ratio.

Introducing colder combustion chamber walls will further increase the heat extraction. This was demonstrated by testing the 20 kW burner in both a water-cooled combustion chamber and an un-cooled combustion chamber. The increased heat extraction seen in experiments with increased power output implies that higher turbulence intensity enhances the heat extraction by convective heat transfer from the combustion products in the post-

flame region to the combustion chamber walls. Sayre et al. (1994) found the same increase in heat extraction and reduction of NO_x emissions when replacing a hot refractory lining with colder water-cooled steel walls in a combustion chamber enclosing a swirl burner. The results discussed here indicate that there exists an upper limit for the confinement ratio to ensure stable operation of the Swirl Burner. It is also important that the combustion chamber is operated with caution to avoid too high heat extraction from the post-flame region and hence burner instabilities.

4.6.2 OH Laser measurements

By studying the OH-plots of the 20 kW Swirl Burner flame in figure 4–15 to figure 4–17, it can be seen how the flame changes in shape with thermal throughput from 5 kW to 13 kW. At 5 kW, the flame appears as a stretched doughnut which is merged together at the flame end. By increasing the throughput to 10 kW, the doughnut shape is completely merged together and the flame appears to have a divergent shape from the bottom of the flame and upwards. It is seen that the flame height and the flame volume have been reduced. At the highest thermal throughput, 13 kW, the flame volume is clearly reduced, and from the OH plot in figure 4–17 the flame shape can be described as spherical and very compact compared to the 5 kW flame.

A significant behaviour of the 20 kW Swirl Burner in the water-cooled combustion chamber is the flame volume reduction with increasing thermal throughput. This was predicted above by assuming that the flame volume was the leading-order parameter for NO_x formation, and applying NO_x scaling correlations (Weber, 1996) to the NO_x emissions measured with this burner and combustion chamber. This prediction is supported by the OH LIF measurements described in chapter 4.5 which have been visualized by the OH contour plots in figure 4–15 to figure 4–17 showing that the flame volume is reduced with increasing thermal throughput.

The NO_x scaling correlation by Weber (1996) used in the plot above (figure 4–22) can be expressed by equation (4–5), where C is a constant. For the constant in equation (4–5), Røkke et al. (1992) used a value of 44 for their diffusion flames, while Weber (1996) reduced this constant with increasing heat extraction to scale NO_x emissions from complex burners.

$$EI_{NOx}\rho_0 u_0 / d_0 = C \times Fr^{0.6}$$
(4–5)

To fit the NO_x emissions measured from the 20 kW Swirl Burner in the water-cooled combustion chamber into the plot in figure 4–22, a value of 44, 29 and 25 must be used for the constant in equation (4–5) for measurements made at thermal throughput of 5 kW, 10 kW and 13 kW respectively. From the OH contour plots in figure 4–15 to figure 4–17 flame heights and diameters can be found. It is seen that the maximum flame diameters are nearly constant, while the flame heights change with thermal throughput. The flame heights are plotted against the measured emissions of NO_x for each flame in figure 4–24, where it can be seen that the formation of NO_x in the 20 kW burner in the water-cooled combustion chamber is increasing as the flame height increases. Reduction of flame volume is according to Weber (1996) caused by increased heat extraction which implies that the volume change of the 20 kW Swirl Burner flame is caused by increased heat extraction with increased thermal throughput.
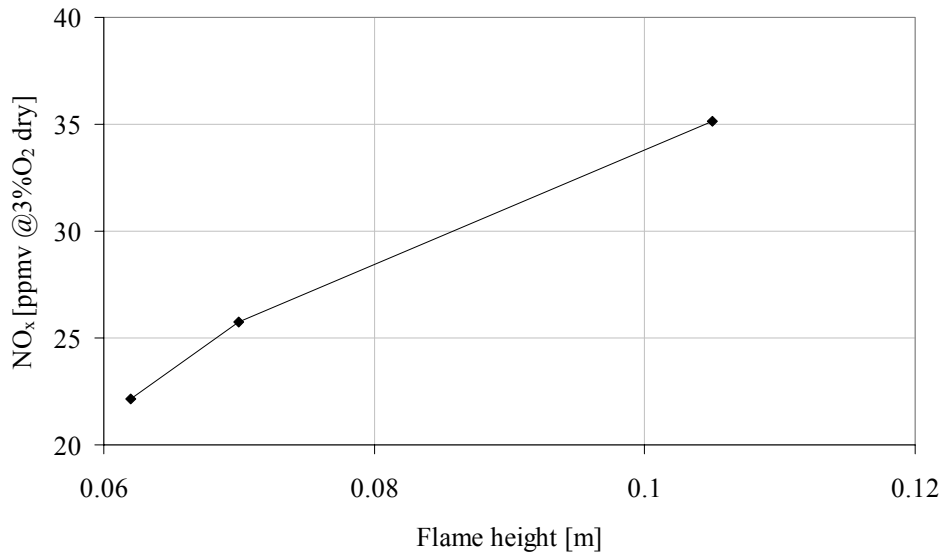
Figure 4–24 Flame height vs. emission index of NO_x (EI_{NOx}).

The increase in heat extraction seen with the 20 kW Swirl Burner in the water-cooled combustion chamber was not found for the 200 kW burner in the CEN boiler or the 370 kW burner in the Vertical boiler where the value of C in equation (4–5) was found to be constant for the emissions of NO_x measured at various thermal throughput for these burners and boilers. The main difference in these burner and boiler setups, as was touched upon above and illustrated by the plot in figure 4–23, is the confinement ratio. There is also a difference in cooling effect between the un-cooled combustion chamber and the water-cooled combustion chamber. The NO_x emissions measured in the former are better predicted using a constant value of C in equation (4–5) than in the latter, hence heat extraction can be assumed to be constant with thermal throughput in the un-cooled combustion chamber.

As mentioned above, most of the heat extraction from enclosed burners is found to take place in the post-flame region (Sayre et al., 1994). By shortening the flame, the post-flame region will be larger in volume and more heat can be extracted from the combustion products by radiative and convective heat transfer from this region before being entrained into the flame by internal flue gas recirculation. Besides reduction in flame temperatures by enhanced heat extraction, formation of NO_x via the thermal NO mechanism will be reduced by the shorter residence time caused by the flame volume reduction.

The reason for flame shortening has not yet been properly divulged, but this behaviour might be caused by the negative axial velocities induced by the swirling flow. By increasing the thermal throughput, the burner exit velocity and hence the swirl intensity is increased which again results in a higher recirculation velocity. Due to increased burner exit velocities and recirculation velocities in the opposite direction, the flame becomes more compact at high thermal throughout than at lower thermal throughput. This behaviour remains to investigate further by experiments.

4.7   Summary and conclusions

The 200 kW Swirl Burner has been extensively tested for variations in the burner geometry such as the fuel nozzle configuration, the swirl number and the position of the gas tube. An optimal design has been found for this burner with respect to the emissions of

NO_x and the fuel and air supply pressure. The burner has been optimized for both propane and methane as fuel. The 200 kW Swirl Burner has been tested with power output in the range 80 kW to 320 kW, i.e. a turn down ratio of 4:1.

The constant velocity scaling approach has been used for scaling the Swirl Burner to a 20 kW and a 370 kW burner. The optimized 200 kW burner was used as scaling basis. The 370 kW burner was scaled using the scaling criteria for all dimensions including the fuel supply nozzles, while for the 20 kW burner the fuel supply nozzles was found experimentally. The latter burner, where the fuel to air momentum ratio was not preserved while scaling, was found to operate less stable than the 370 kW burner where this ratio was preserved from the 200 kW burner.

NO_x emissions from the 200 kW burner in the CEN boiler and the 370 kW burner in the Vertical boiler were found to scale with the correlation by Weber (1996) stating that the EI_{NOx} multiplied by $\rho_0 u_0/d_0$ is proportional to $Fr^{0.6}$, implying that flame volume is the leading-order parameter for NO_x formation in these burners. For burners with a confinement ratio higher than 8, the NO_x emissions were not found to be proportional to $Fr^{0.6}$. The correlation by Weber (1996) suggests that this is due to increased heat extraction from the combustion products in the post-flame region.

The 370 kW Swirl Burner has been operated in the range from 300 kW to 550 kW power output. This narrow operation range was caused by limitations on the combustion air fan and the Vertical boiler. The 20 kW Swirl Burner has been operated in the power output range from 5 kW to 20 kW in an un-cooled combustion chamber and from 5 kW to 17 kW in a water-cooled combustion chamber. The 20 kW burner operation range was limited by lift-off in the upper range and flame instabilities at lower power output. Burner stability is affected by post-flame heat extraction.

The flame front in the 20 kW Swirl Burner in the water-cooled combustion chamber has been visualized by OH LIF measurements in the flame at 5 kW, 10 kW and 13 kW. It has been found that the flame height and volume are decreasing with increasing thermal throughput. The flame volume reduction agrees with the NO_x scaling correlations by Weber (1996) which suggests that the heat extraction is increasing with increasing thermal throughput.

Heat extraction from the 20 kW burner in the water-cooled combustion chamber is enhanced by the high confinement ratio (> 8) and by the low combustion chamber wall temperatures. Reduced flame heights with increasing thermal throughput increase the volume of the post-flame region and hence the post-flame heat extraction. Formation of NO_x is reduced by increased thermal throughput due to increased post-flame heat extraction and reduced flame residence time.

5   *Computational Fluid Dynamics*

5.1   Introduction

The computational fluid dynamics (CFD) investigation of the Swirl Burner was carried out using the commercial CFD program FLUENT. This is a commercial code designed for modelling various fluid flow and heat transfer problems in complex geometries.

There are many commercial codes available on the market beside FLUENT, and a few of them are: CFX, Star CD, Flow-3D, CFD-ACE and PHOENICS. All of these are able to solve complex turbulent flow problems, and in most of them, models for solving reacting flow are included as well. This study does not include an evaluation of commercial CFD software, but the motivation for choosing FLUENT as a modelling tool for this work will be presented.

At NTNU, a reasonable amount of FLUENT licences for research work and student projects within the university were already available. The availability of CFD software without spending an excessive amount of project-funding was an important motive for choosing FLUENT, since these codes are fairly expensive for each license in use. The expertise and skills on using FLUENT available through my colleague Tom Engebretsen working at SINTEF Materials Technology, where FLUENT already was in use for modelling of reacting flow, was another reason for choosing this software. At last, when considering going abroad one year as a part of this thesis work, the CFD group at the University of Leeds had a lot of experience in using FLUENT for modelling of turbulent combustion.

The computations and the results that will be presented here are performed on a 20 kW Swirl burner using propane (C_3H_8) as fuel. This is the same burner and combustion chamber setup that was used for the OH LIF measurements of the Swirl Burner found described in chapter 4.5.

5.2   Problem setup

5.2.1   Description of grid

The computational mesh used in the following computations is 2D axisymmetric and consists of about 21000 cells. This grid can be seen in figure 5–1. The assumption of the burner and combustion chamber being axisymmetric simplified the computations by enabling a 2D solution of the turbulent reacting flow. The reduction in grid size from 3D to 2D resulted in a considerable reduction in CPU time necessary to reach convergence and memory needed for solving the problem. The 2D computations could be carried out on a standard Pentium 3 workstation or laptop with 512 megabytes of memory.

The grid is structured and was created with a higher density of nodes in areas where the fluid flow was expected to change much and where a finer grid resolution was assumed to be beneficial for achieving an accurate solution, such as close to the burner exit and around the fuel nozzles. A close-up of the mesh around the burner section can be seen in figure 5–2. The grid refinement around the fuel nozzles can clearly be seen as two vertical regions of higher grid density. While constructing this grid, the skewness of the grid elements defined by equation (5–1) was kept as low as possible and a maximum value of 0.39 was achieved for this grid. The average element skewness was 0.1.

$$Q_{EAS} = max\left\{\frac{\theta_{max} - 90}{90}, \frac{90 - \theta_{min}}{90}\right\}$$ (5–1)

In equation (5–1) θ_{max} and θ_{min} are the maximum and minimum angles in degrees between the edges of an element. A Q_{EAS} of 0 describes a perfect rectangular element, whereas a Q_{EAS} equal to 1 describes a completely degenerate (poorly shaped) element. When examining grid quality, a Q_{EAS} value between 0 and 0.25 is defined as excellent and a Q_{EAS} value between 0.25 and 0.5 is good. In general a high-quality 2D mesh should contain elements that possess an average Q_{EAS} value of 0.1 (Fluent Inc., 2003).
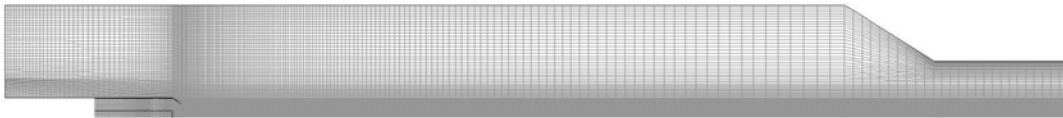
Figure 5–1 Computational grid used for the 20 kW Swirl Burner.
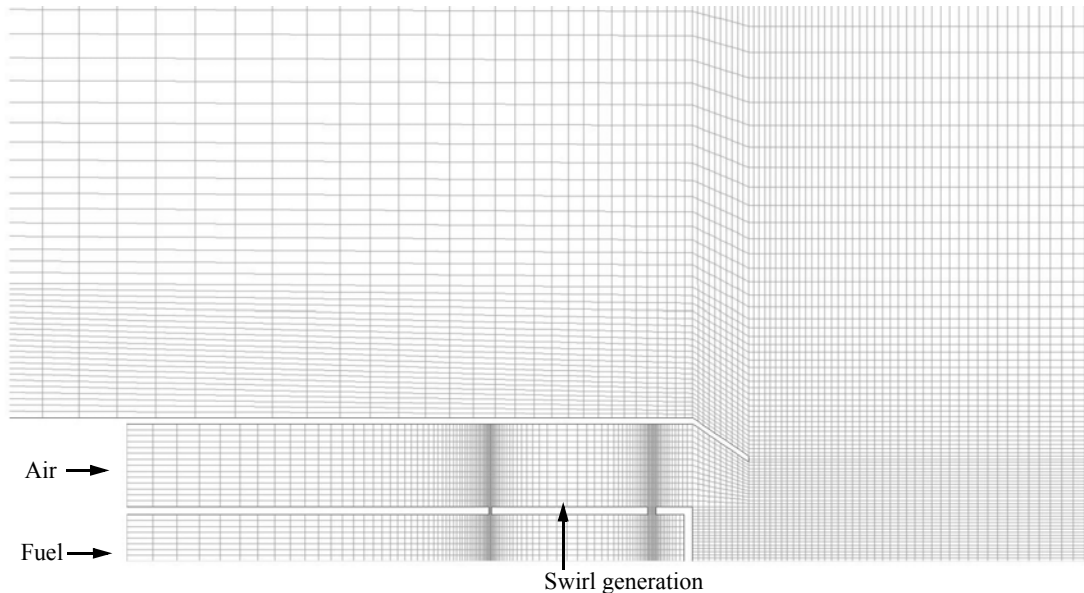
Figure 5–2 Close-up of the burner section of the grid, with air and fuel inlet and position for the swirl generation indicated.

5.2.2 Boundary conditions

Calculations were carried out using an operating pressure of $1.01e^5$ Pa. Fuel and air inlet mass-flows are given for various thermal throughputs in table 5–1. Both fuel and air inlet temperatures were set to 298 K and the hydraulic diameters of the inlets are respectively 20.5 mm and 11.5 mm for air and fuel. The inlets are indicated in the grid in figure 5–2. The bottom of the combustion chamber which is seen in the left end of figure 5–1 is insulated steel, whereas the side walls are water cooled steel and the conical top is uncooled steel. The temperature at the water cooled walls were set to 373 K (100 °C) and for the uncooled conical top and exhaust pipe it was set to 650K. The exhaust outlet, which is found at the right hand side of figure 5–1, was defined as a pressure outlet with a hydraulic diameter of 100 mm. The gauge pressure at the outlet was set to 50 Pa and the backflow temperature to 650 K.

Table 5–1 Flow-rates for fuel and air inlets (3% O_2 in flue gas).

Mass-flow inlet	5 kW	10 kW	15 kW	20 kW
Air [kg/s]	0.001945515	0.003891029	0.005836544	0.007782059
Fuel (C_3H_8) [kg/s]	0.0001078283	0.0002156567	0.000323485	0.0004313133

Swirling flow was generated by defining a tangential velocity as an internal boundary condition where the swirl generator is located, at about 20 mm upstream of the burner exit as indicated in figure 5–2. This was done by creating a user defined function in Fluent. Input to this function is the axial velocity component calculated by Fluent in the cells where it is applied to create a tangential velocity component in the very same cells. The tangential velocity component is defined by equation (5–2), where u_θ is the tangential velocity, u_x is the axial velocity and β is set to 60 degrees. The user defined function can be found in appendix C.

$$u_\theta = u_x \times \tan\beta \qquad\qquad (5\text{–}2)$$

Turbulence modelling of swirling flows is closer discussed in chapter 2.5.2.

5.2.3 Combustion models

During the following calculations, three different chemistry models were evaluated to account for the combustion of propane with air in the Swirl burner. These were the Eddy Dissipation model and two mixture fraction based models.

The Eddy Dissipation model was proposed by Magnussen and Hjertager (1976) and assumes that the reaction rate in turbulent combustion is controlled by turbulent mixing of fuel and oxidizer. A two step propane-air mechanism predefined in the FLUENT materials database containing six species (C_3H_8, O_2, CO, CO_2, H_2O and N_2) where CO is an intermediate and N_2 an inert species, was used for the volumetric reactions in the Eddy Dissipation model.

The mixture fraction based models used were the Equilibrium model and the Flamelet model. Both of these were set up using FLUENT's pre-processor, PrePDF. The Equilibrium model is based on the assumption that the chemistry is rapid enough for chemical equilibrium always to exist at the molecular level. In PrePDF, a lookup table was created for the chemical system based on minimization of Gibb's free energy (Kuo, 1986 p101-104). The Equilibrium model was set up as non-adiabatic using a β-function for the probability density function (PDF) to describe the chemical system consisting of 12 species (C_3H_8, C_2H_6, CH_4, CO, CO_2, N_2, O_2, H_2O, H_2, O, OH, H). The lookup table was implemented into the turbulent flow calculation in FLUENT through the conserved scalars mixture fraction, $\bar{f}$, and its variance, $\overline{f''^2}$ (Jones and Whitelaw, 1982).

The lookup table for the Flamelet model (Peters, 1984 and 1986) was also created in PrePDF. The Flamelet model is a non-equilibrium model where the chemistry in turbulent flames is assumed to be similar to that found in thin, one-dimensional laminar flames (Peters, 1984 and 1986). The lookup table was calculated in prePDF as non-adiabatic multiple strained laminar flamelets using the GRI-Mech Version 3.0 chemical mechanism (Smith et al., 1999) that had been modified by removing all the NO-related reactions. This modification was done to reduce the calculation time in PrePDF and because the NO-chemistry could be post-calculated in FLUENT. The modified chemical mechanism con-

sisted of 36 species, from which 20 were selected by PrePDF to be included in the final flamelet lookup table. The species were selected by concentration for the given fuel and oxidizer. The mixture fraction was assumed to follow the β-function for the probability density function (PDF) and scalar dissipation the double-delta-function PDF.

5.2.4 The solver

For these computations, a segregated solver formulation was used. This implies that the continuity, momentum, energy and species equations were solved sequentially in stead of simultaneously as in a coupled solver. Using a control-volume based technique, FLUENT converts the governing equations to algebraic equations that can be solved numerically. The control volume technique consists in integrating the governing equations about each control volume, yielding discrete equations that conserve each quantity on a control-volume basis (Fluent Inc., 2003). The solver stores discrete values of the scalars at the cell centres and to determine the scalar's value in between the cell centres, a second order upwind scheme was used for interpolation. As recommended by Fluent Inc. (2003) for strong swirling flows, the PRESTO! scheme was used for pressure interpolation. For the velocity-pressure coupling, the SIMPLE method described by Patankar and Spalding (1972) was used.

The flow was calculated as steady-state to achieve a time independent solution. If convergence problems occurred during computations, time-stepping the solution before trying to achieve a new steady-state converged solution could be a useful remedy. The convergence criteria based on scaled residuals was set to 10^{-4} for all equations except the energy and radiation equations which was set to 10^{-6}.

5.3   Evaluation of computational models

5.3.1   Turbulence models

Before deciding which turbulence model to use for the Swirl burner computations, a series of isothermal computations were carried out to investigate the performance of three different turbulence models in strong swirling flow. The turbulence models that were considered were the first moment closure standard k-ε and RNG k-ε models and the more elaborate Reynolds Stress Model (RSM). These models have been described and discussed in chapter 2.5.2. Under isothermal conditions, the fluid is set to air and the mass-flow through the computational domain corresponds to the mass flow at 10 kW thermal throughput.

A fundamental feature of strong swirling flow ($S > 0.6$) is the presence of a central toroidal recirculation zone (CTRZ) close to the swirl generator exit caused by radial and axial pressure gradients (Gupta et al., 1984). In figure 5–3 the zero-axial velocity contours are plotted from the flow fields calculated with the three turbulence models. The zero-axial contours indicate the boundaries for the recirculation zones in the swirling flow field. Both the CTRZ and the corner recirculation zone (CRZ) are labelled in figure 5–3. The calculated mean axial velocity profiles at various positions downstream the burner exit are shown in figure 5–4.

From figure 5–3 it can be seen that all three models manage to predict the expected recirculation zones described in literature (CTRZ and CRZ), but the size and shape of these zones differ between the models. In the CRZ which appears due to the flow expansion, the velocities are relatively small as can be seen in figure 5–4, but from figure 5–3 it is noticed that even this relatively calm recirculation zone is predicted differently by the three models. The CRZ predicted by the RSM has a more distinct shape than the CRZ predicted by the two k-ε models which appear more rounded in shape. This is due to a

"smearing" effect caused by the isotropic turbulence treatment in the k-ε models. It is also clearly seen from figure 5–3 that the RSM predicts a larger CRZ than both the k-ε models. Between the k-ε models, the RNG k-ε model predicts a slightly larger CRZ than the standard k-ε model.

For prediction of the more turbulent intense and highly non-isotropic CTRZ (Gupta et al., 1984), the differences between the three turbulent models are more noticeable. In figure 5–3, it is seen that the length of the CTRZ predicted by the RNG k-ε model is increased by a factor of 1.5 - 2.0 in the axial direction compared to the CTRZ predicted by the standard k-ε model, but apart from the change in length, the shape of the CTRZ computed using the RNG k-ε model has a similar shape as the CTRZ computed by the standard k-ε model. This might be caused by the additional rate of strain term introduced into the ε-equation and the swirl-modification of the turbulent viscosity in the RNG k-ε model which reduces the isotropy predicted by the k-ε models.

The difference between the evaluated turbulence models can also be seen from figure 5–4 where the computed axial velocity profiles at various axial locations are shown. Also here the "smearing" effect of the standard k-ε model can be seen; the axial velocity peak is diffused radially outwards with axial position, while the other two models predicts a higher peak velocity which is more slowly attenuated with axial position and the velocity peak is less radially diffused.

For these computations, probably the most important feature of the turbulence model is the prediction of the CTRZ. As seen in figure 5–4 and expected from various literature (Engdar and Klingmann, 2002, Benim, 1990, Hanjalic, 2002) and discussed in chapter 2.5.2, the standard k-ε model does not predict as strong a recirculation as the RNG k-ε model and the RSM do. There exists an excessive amount of evidence in the literature (see chapter 2.5.2) showing that the standard k-ε model perform badly compared to experiments in swirling flow. When it comes to the RNG k-ε model, as discussed in chapter 2.5.2, there is some improvement from the standard k-ε model for the purpose of modelling swirling flow (Widman et al., 2000), but there is also evidence that this improvement is non-existent or very small, especially for strong swirl (Xia et al., 1998, Verboven et al., 2000). As seen in figure 5–3 and figure 5–4, in the axial direction the RNG-modification results in less attenuation of velocities compared to the standard k-ε model, but compared to the RSM prediction this model predicts higher axial velocities in both directions, and hence a stronger CTRZ.

A clear weakness of this evaluation is the lack of experimental measurements to judge the computations, but as discussed in chapter 2.5.2, there exists lots of evidence in literature of the superiority of the RSM over two-equation models such as the standard k-ε model and the RNG k-ε model (Hanjalic, 2002, Sharif and Wong, 1995, Benim, 1990, Xia et al., 1998). Additionally, for computations of strong swirling flows in FLUENT, RSM is the turbulence model recommended by Fluent Inc. (2003).

From this evaluation of computations of an isotropic test case and from recommendations in literature, it is clear that the RSM is superior to the two other models evaluated. The investigation has also demonstrated that the RNG k-ε model might produce a satisfactory prediction of swirling flows. The advantage of the RNG k-ε model is that it is robust and easy to converge with less computational resources than the RSM. These advantages make the RNG k-ε model attractive to use also together with the RSM for modelling of complex flow. A converged solution achieved using the RNG k-ε model makes a good starting point for further computations using the RSM. The total computational time and effort needed for achieving an accurate converged solution can be reduced using this strategy (Fluent Inc., 2003).
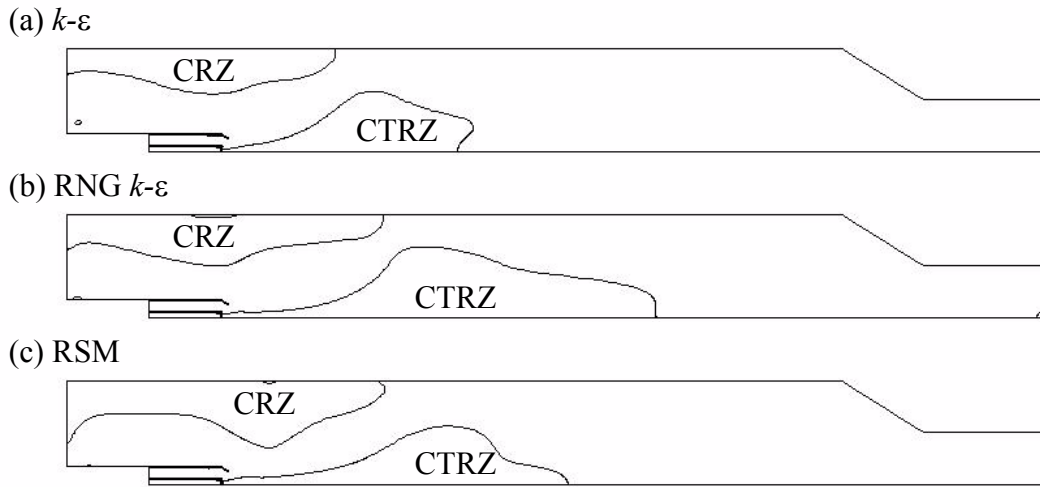
Figure 5–3 Contours of zero-axial velocities; (a) k-e; (b) RNG k-ε; (c) RSM.
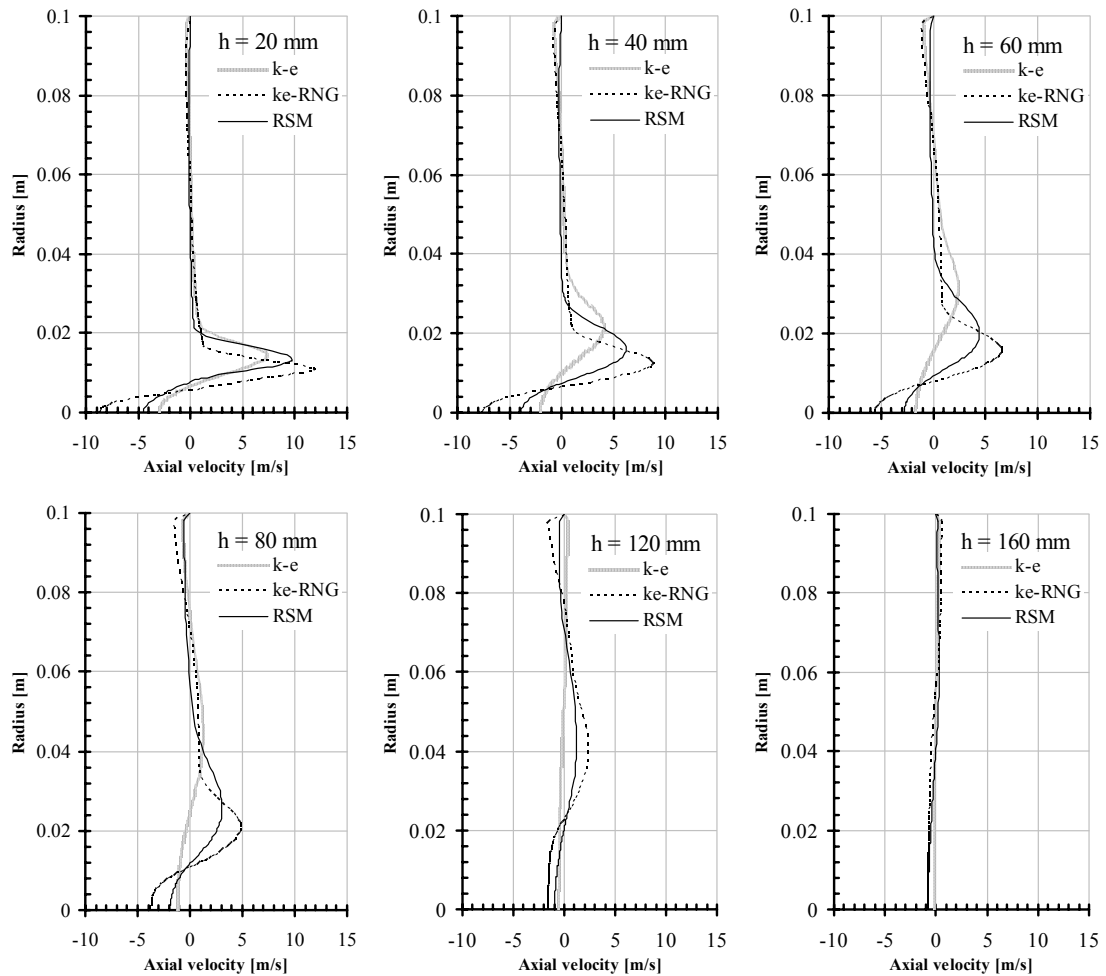
Figure 5–4 Mean axial velocities at various positions above the burner (h) using the k-ε model, the RNG k-ε model and the RSM for a cold flow.

5.3.2 Combustion models

In a similar way as for the turbulence models, three different models for the combustion chemistry were evaluated. These were the Eddy Dissipation model, the Equilibrium PDF model and the Flamelet PDF model. These models are described in chapter 2.5.3. An attempt was also made to model combustion chemistry by the Eddy Dissipation Concept (EDC), but with this model, it was not found possible to get a converged solution. The turbulent flow was modelled using the RSM discussed in chapter 5.3.1 above. The boundary conditions are described in chapter 5.2.2 and the flow rates for 10 kW thermal throughput are used (see table 5–1). Since this setup is non-isothermal, the energy equation was enabled.

To visualize the recirculation zones, zero-axial velocity contours were again plotted from the calculated flow fields (figure 5–5). The effects of the combustion models on the recirculation zones are seen by comparing these plots with the isothermal plot in figure 5–3(c). Due to density changes, it is expected that the velocities and hence the recirculation zones will change from the isothermal calculations. The calculated velocity field for each reaction model is shown in figure 5–6.

The reaction models clearly affect the prediction of the characteristic CTRZ in various fashions. As seen in figure 5–5, the CTRZ predicted with the Eddy Dissipation model is longer and has a different shape than the two other CTRZs predicted with the Equilibrium PDF and the Flamelet PDF models. The CTRZ and the CRZ predicted with the Eddy Dissipation model resemble the zones predicted in the isothermal calculation in figure 5–3(c), the main difference being that the recirculation zones are more stretched in the axial direction due to velocity increase because of the temperature change from the isothermal flow to the reacting flow.

(a) Eddy Dissipation
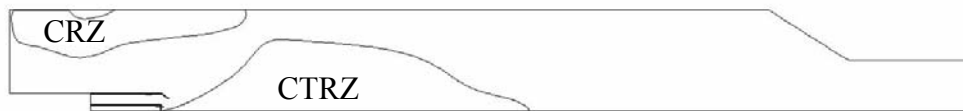
(b) Equilibrium PDF
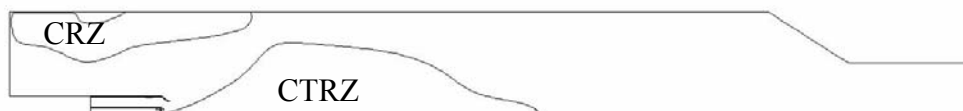
(c) Flamelet PDF

Figure 5–5 Contours of zero-axial velocities; (a) Eddy Dissipation; (b) Equilibrium PDF; (c) Flamelet PDF.

A result of Magnussen and Hjertager's (1976) assumption that chemical reactions are controlled by turbulence, is that all chemical reactions will be taking place in the most turbulent regions of the flow where fuel and oxidizer are present. This means that except for locally increasing the temperature and hence altering the fluid density, the chemical reactions modelled by the Eddy Dissipation model do not drastically change the flow predicted with reactions compared to the isothermal flow. Since the chemical reactions are being calculated on a "mixed-is-burned" basis, a well known weakness of the Eddy Dissipation

model is that the formation of combustion products is grossly overpredicted, and consequently the temperature increase is overpredicted as well (Warnatz et al., 1999 p199). This is seen in figure 5–7(a) where the temperatures predicted with the Eddy Dissipation model are displayed. The peak temperature calculated by using the Eddy Dissipation model is here found to be as high as 2293 K, which is even higher than the maximum flame temperature for propane-air mixtures (2250 K: Griffiths and Barnard, 1995).

Compared with calculations using the Eddy Dissipation model, flow calculations using the Equilibrium PDF model or the Flamelet model for chemical reactions produces a different flow pattern. From figure 5–5(b) and (c) it can be seen that the recirculation zones differ from both the Eddy Dissipation calculated flow in figure 5–5(a) and the isothermal flow prediction in figure 5–3(c). The CTRZ is increased in size and diameter compared to the other calculations while the CRZ is less dominant. From figure 5–6, it can be seen that the velocity flow pattern is more divergent in shape from the burner exit, and as a result the CTRZ is located closer to the burner than predicted with the Eddy Dissipation model. The increased diameter of the CTRZ results in an increase of the combustion products entrained into the flame. This is an important feature of swirling flows which in combustion will ensure both flame stabilization and reduction of flame temperatures due to dilution of the combustion gases.

The temperatures predicted with the three reaction models can be seen in figure 5–7. These plots show that the peak temperatures predicted with the Equilibrium model and the Flamelet model are well below the peak temperature predicted with the Eddy Dissipation model; respectively 1828 K and 1736 K compared to 2293 K. In figure 5–7(b) and (c) it is also seen that due to the increased amount of combustion products entrained into the CTRZ, the maximum temperature region is considerably reduced in size. The reduction in predicted peak temperatures and size of the high temperature regions will have an influence on the calculation of NO_x formation.

Similarities of the flow patterns predicted with the Equilibrium PDF model and the Flamelet PDF model for chemical reactions are caused by the turbulence-chemistry interaction which in both models is modelled using a probability density function. The difference between the Equilibrium PDF and the Flamelet PDF model is the methods used for creating the lookup table (see chapter 2.5.3), which in both cases are linked to the turbulent flow by assuming that the mixture fraction follows a β-function for the probability density function. This results in similar flow fields predicted, but in different thermochemical state of the reacting flow as seen for the temperatures in figure 5–7(b) and (c).

It has been shown that the three different reaction models give different results for the flow field prediction. The Eddy Dissipation model predicted less combustion product entrainment into the CTRZ than the other models evaluated and unrealistically high combustion temperatures. The two PDF-based models evaluated (Equilibrium and Flamelet) predicted similar flow patterns with more dominant CTRZs where more combustion products are entrained. The PDF models predicted more realistic combustion temperatures than the Eddy Dissipation model. Besides the very high temperature prediction, the Eddy Dissipation model considers only 6 species. Both PDF models can take more species into consideration, including important intermediate radicals like OH which also takes part in the thermal NO and the prompt NO mechanisms. Prediction of OH is also important for the purpose of comparison of computational results with experimental data from the OH LIF measurements. The Flamelet model has the advantage over the Equilibrium model that it can predict moderate chemical non-equilibrium effects in turbulent flames due to aerodynamic straining by the turbulence (Fluent Inc., 2003). The performance of the Equilibrium and the Flamelet model has been compared by other workers (Kyne et al., 2002, Price et al., 2002, Goldin and Choudhury, 2001) and their investigations concluded

that the Flamelet model performed better towards experimental data, especially with regards to OH (Goldin and Choudhury, 2001) and NO (Price et al., 2002), which are of special interest here. Based on the results and discussion above and the results found in literature, it was concluded to base the following computations on the Flamelet PDF model for the combustion chemistry.

(a) Eddy Dissipation
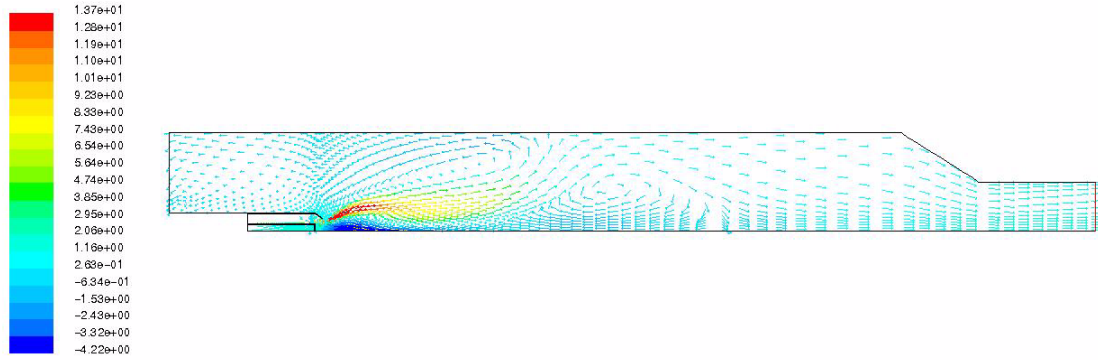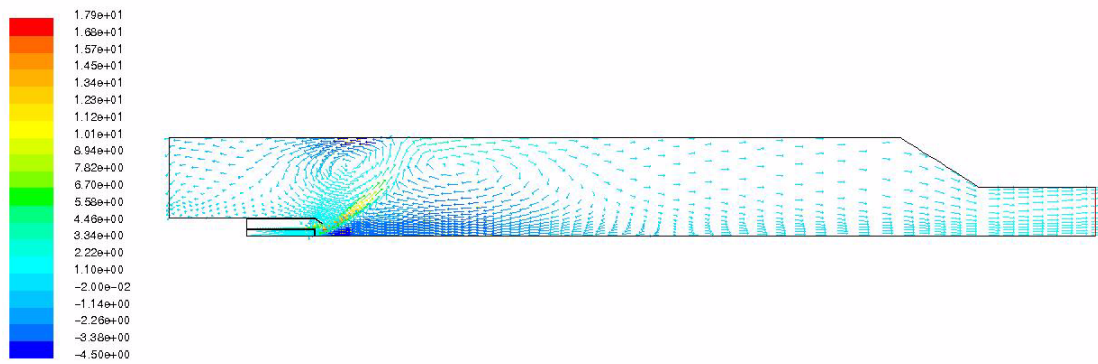
(b) Equilibrium PDF
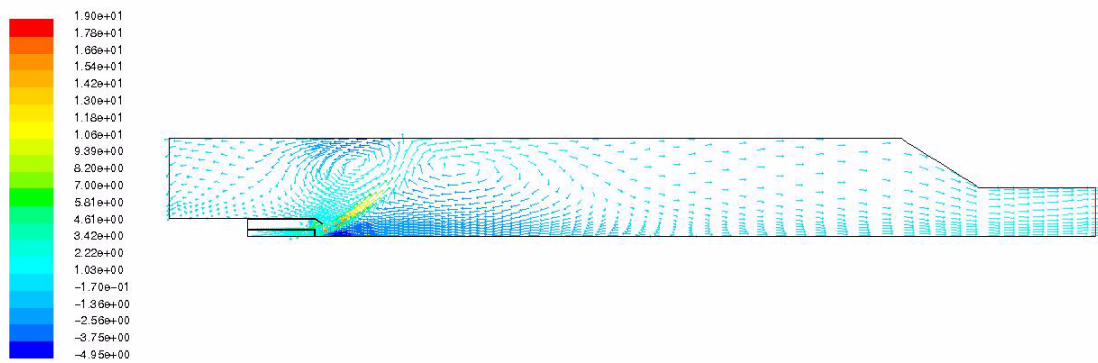
(c) Flamelet PDF

Figure 5–6 Computed velocities in Swirl Burner, coloured by axial velocity; (a) Eddy Dissipation; (b) Equilibrium PDF; (c) Flamelet PDF.

(a) Eddy Dissipation

(b) Equilibrium PDF
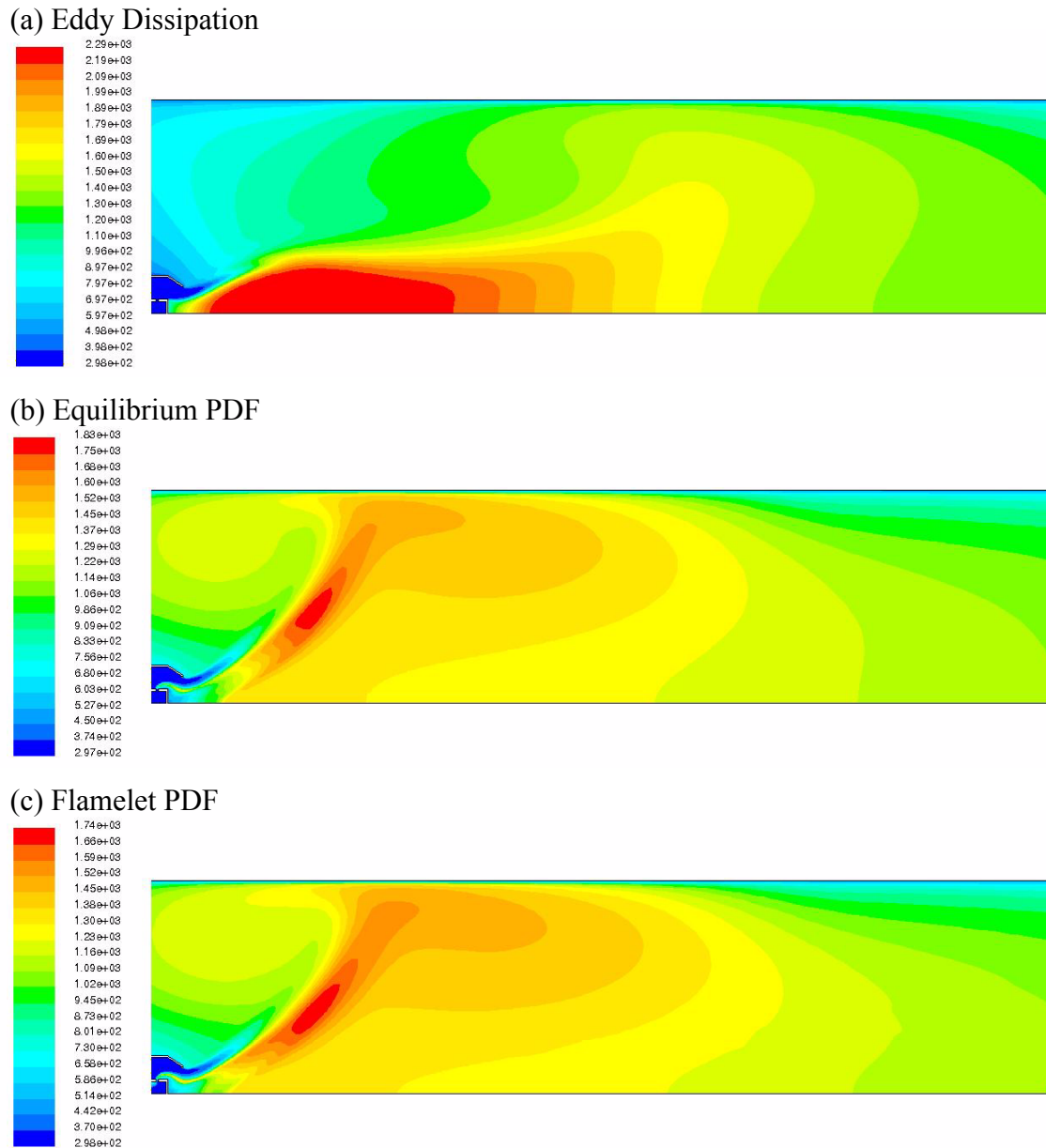
(c) Flamelet PDF

Figure 5–7 Contours of temperature (K); (a) Eddy Dissipation; (b) Equilibrium PDF; (c) Flamelet PDF.

5.4   Recirculation zones, velocities and temperatures

From the evaluation of turbulence and combustion models in chapter 5.3, the Reynolds Stress Model and the Flamelet PDF model were chosen for the Swirl Burner computations. To increase the accuracy of the computations, the grid was refined in the regions around the flame. When convergence was reached for each case, the grid was refined using the grid adaption function in FLUENT in the regions where the OH mole fractions were higher than $1.4e^{-4}$. The computations were then restarted to achieve a converged solution on the refined grid. The grid adaption in FLUENT divides each cell-face in two, i.e. each of the quadrilateral cells in the selected region are divided into four cells. A refined grid is shown in figure 5–8.

The Swirl Burner calculations were carried out for flows with thermal throughput of 5 kW, 10 kW and 15 kW. This was according to the range where the flame stability was found to be good enough for measurements in chapter 4.4. The mass flows of fuel and air can be found in table 5–1.
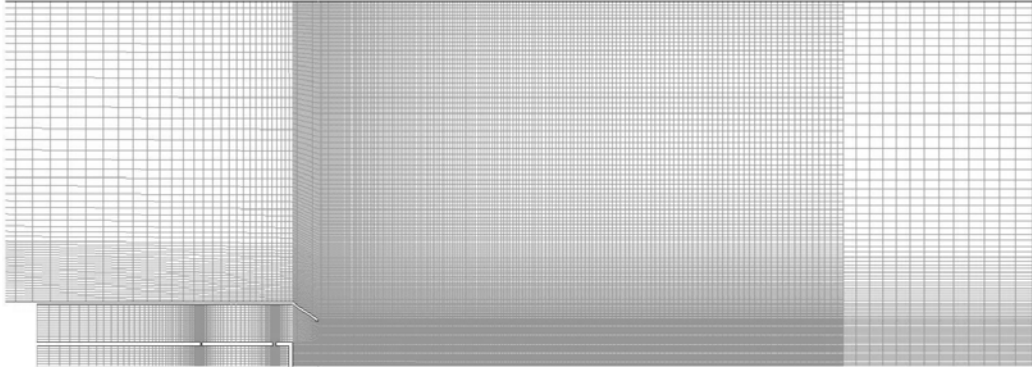
Figure 5–8 Refined grid for the 15 kW calculations.

During these calculations, it was experienced that the 5 kW case was difficult to converge. Convergence could only be reached by making the case time-dependent and stepping forward in time before solving the case as time-independent again. The difficulties with finding a steady solution at 5 kW might reflect that there are some instability issues at this low throughput. This is in accordance with the experimental findings in chapter 4.4 where the burner was found to be unstable at 5 kW.

From the converged solutions, the recirculation zones are visualized by plotting the zero axial velocity contours (figure 5–9). These plots show that the predicted CTRZ does not change when the throughput changes from 5 kW to 15 kW. The internal recirculation is caused by axial and radial pressure gradients set up by the rotating flow (Gupta et al., 1984). The strength of the recirculation is dependent on the intensity of the swirl. The calculated swirl velocities are plotted in figure 5–10. Even though the CTRZ does not change in size, figure 5–10 shows that the swirl intensity is reduced with reduced thermal throughput. At 5 kW the swirl velocities are reduced to about one third of the swirl velocities at 15 kW, which corresponds to the same reduction of mass flow through the swirl generator. At 10 kW though, the swirl velocities are still about 75% of the swirl velocities at 15 kW. At 15 kW the swirl velocities might be limited by other factors, such as suppression of the swirl velocities by the combustion chamber walls.
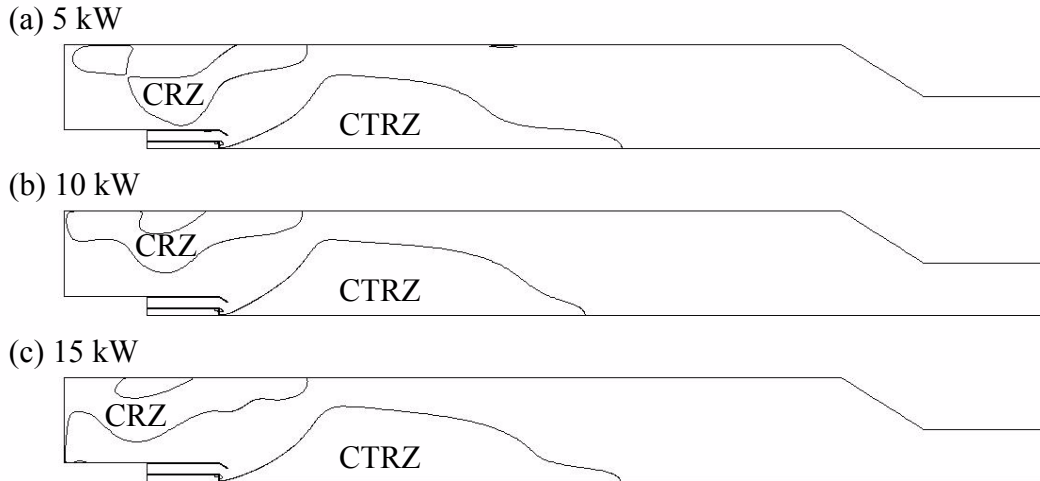
(a) 5 kW

(b) 10 kW

(c) 15 kW

Figure 5–9 Contours of zero-axial velocities; (a) 5 kW; (b) 10 kW; (c) 15 kW.
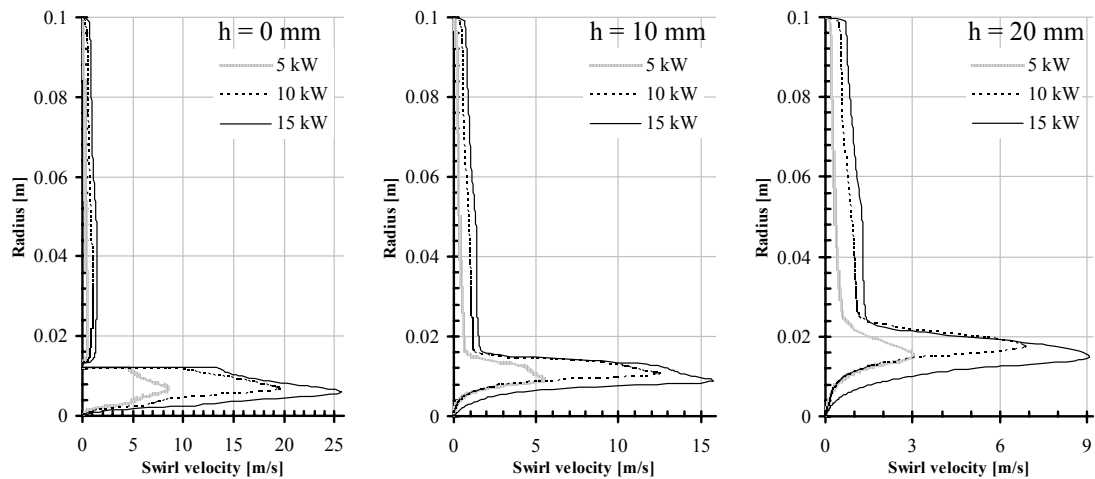
Figure 5–10 Swirl velocities at various positions above the burner (h) at 5 kW, 10 kW and 15 kW.

The amount of combustion gases recirculated into the CTRZ is illustrated by plotting the product of density and axial velocity, the axial mass-flux, at various positions above the burner in figure 5–11. These plots show as seen in figure 5–9 and noticed above, that the radial size of the recirculation zone is unchanged with the burner throughput. More importantly, they show that the mass of the recirculated gases are increasing with increasing burner throughput. This implies that the flame instabilities experienced with the burner at 5 kW thermal throughput, as observed and described in chapter 4.4, can be explained by reduced amounts of hot combustion products being recirculated into the combustion zone to ignite and stabilize the flame.
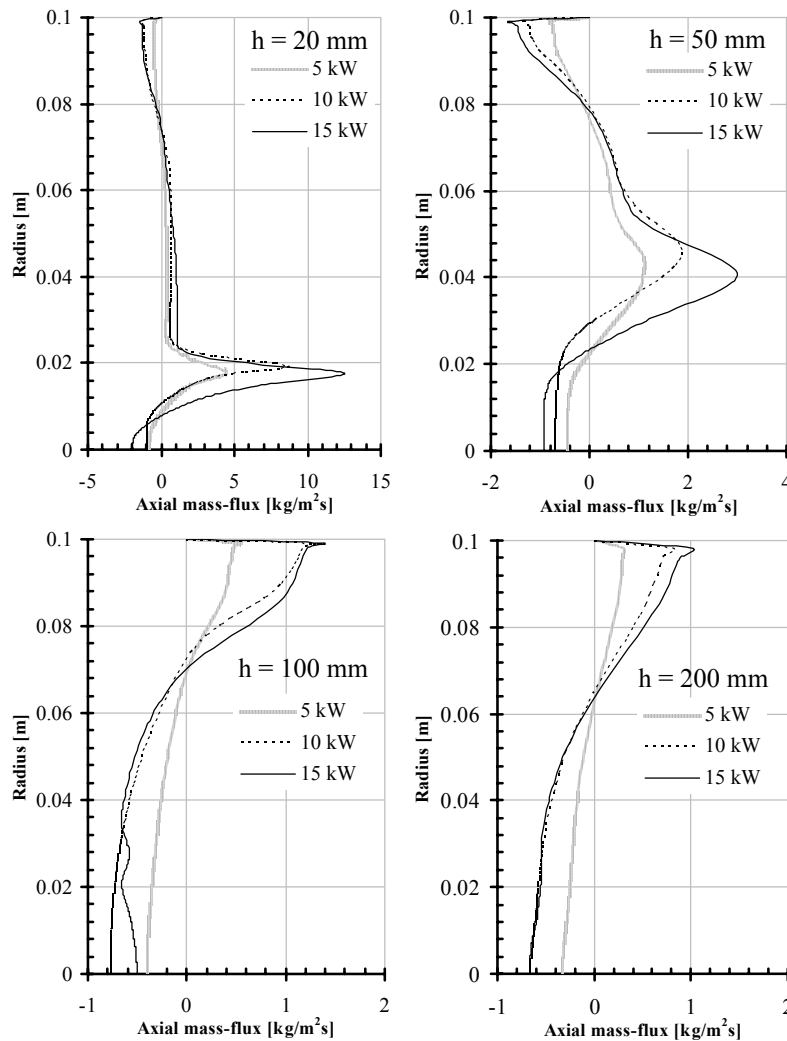
Figure 5–11 Axial flux of mass at various positions above the burner (h) at 5 kW, 10 kW and 15 kW.

The flow fields predicted by these calculations are visualized by the vector plots shown in figure 5–12. Besides illustrating the flow field represented by vectors, the axial velocities are given by the colour scheme applied to the vectors in figure 5–12. In the CTRZ (indicated in figure 5–9), the maximum negative axial velocity are found along the symmetry axis near the burner exit. These negative velocities are as expected, largest for 15 kW, and reduced with reduced thermal throughput. The vector plots clearly demonstrates the divergent shape of the flow exiting from the burner, and that combustion products are recirculated into the flame from the post-flame region.

Temperatures predicted with the Flamelet PDF model for these flames are seen in figure 5–13. The temperatures found, will clearly affect the stability for the 5 kW flame. The recirculated combustion products which are the source of ignition and flame stabilization have considerably lower temperatures in the 5 kW flame than the other flames. In figure 5–13(a) it is seen that the calculated temperatures in the CTRZ for the 5 kW flame are in the range 750 - 1000 K, whereas at higher throughputs the CTRZ temperatures are in the range 1000 - 1350 K and 1100 - 1450 K for 10 kW and 15 kW respectively. The very low

CTRZ temperatures predicted for the 5 kW flame is close to the minimum auto-ignition temperature for propane which is 723 K (Bjerketvedt et al., 1993). The low CTRZ temperature together with reduced recirculation as discussed above, might cause the unstable flame observed from experiments with the Swirl Burner as described in chapter 4.4. In general, the temperatures predicted for the 5 kW flame are considerably lower than at higher throughputs. The peak temperature predicted for the 5 kW flame is only 1450 K while it is predicted to be 1705 K and 1720 K for the 10 kW and 15 kW flames respectively. It is also noticed that all the peak temperatures predicted by these computations are well below 1800 K which, according to Turns (1995), is the minimum temperature for NO_x formation through the thermal NO mechanism.
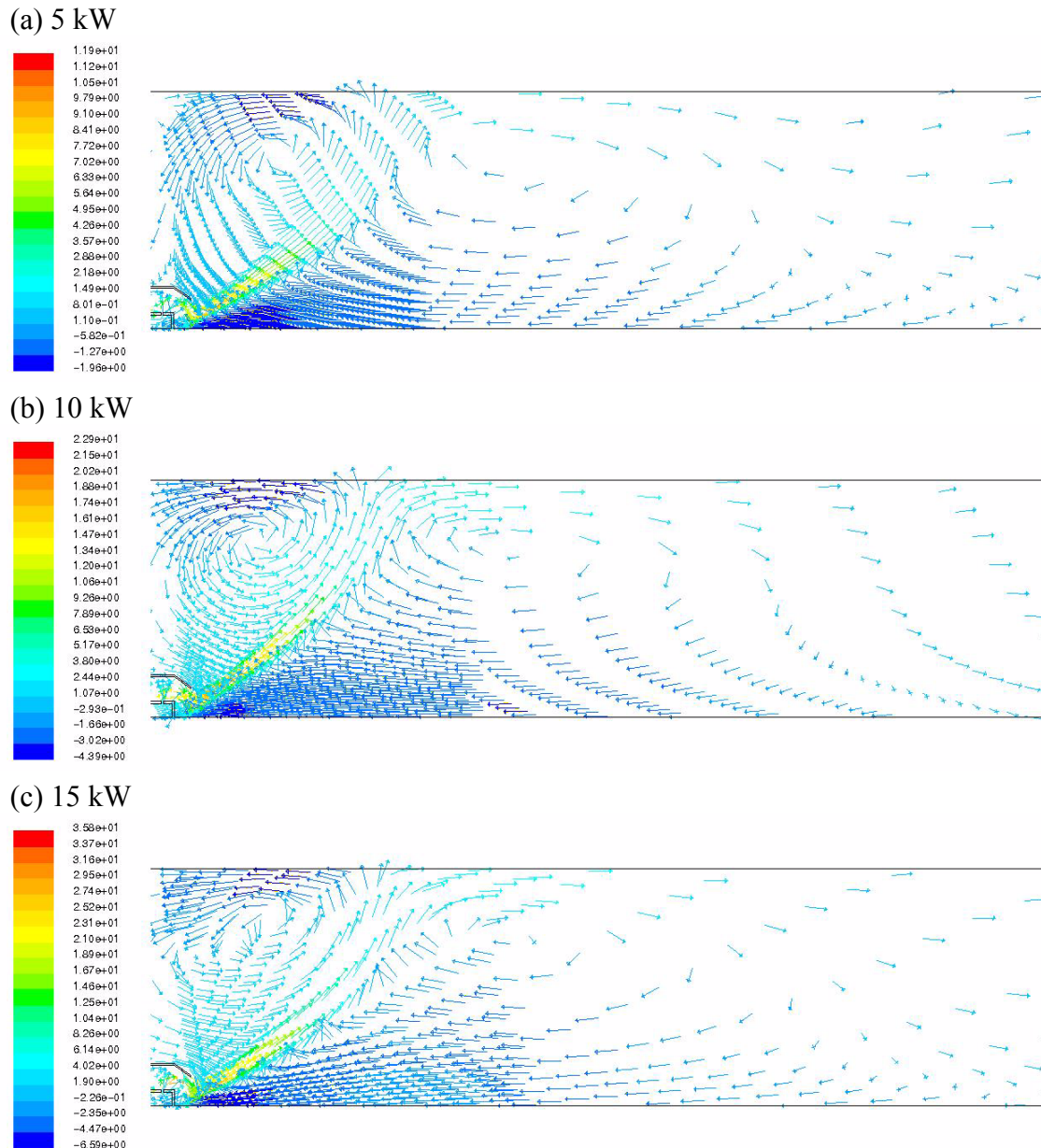
(a) 5 kW

(b) 10 kW

(c) 15 kW

Figure 5–12 Vector plots of computed velocities in the Swirl Burner, coloured by axial velocity (m/s); (a) 5 kW; (b) 10 kW; (c) 15 kW.
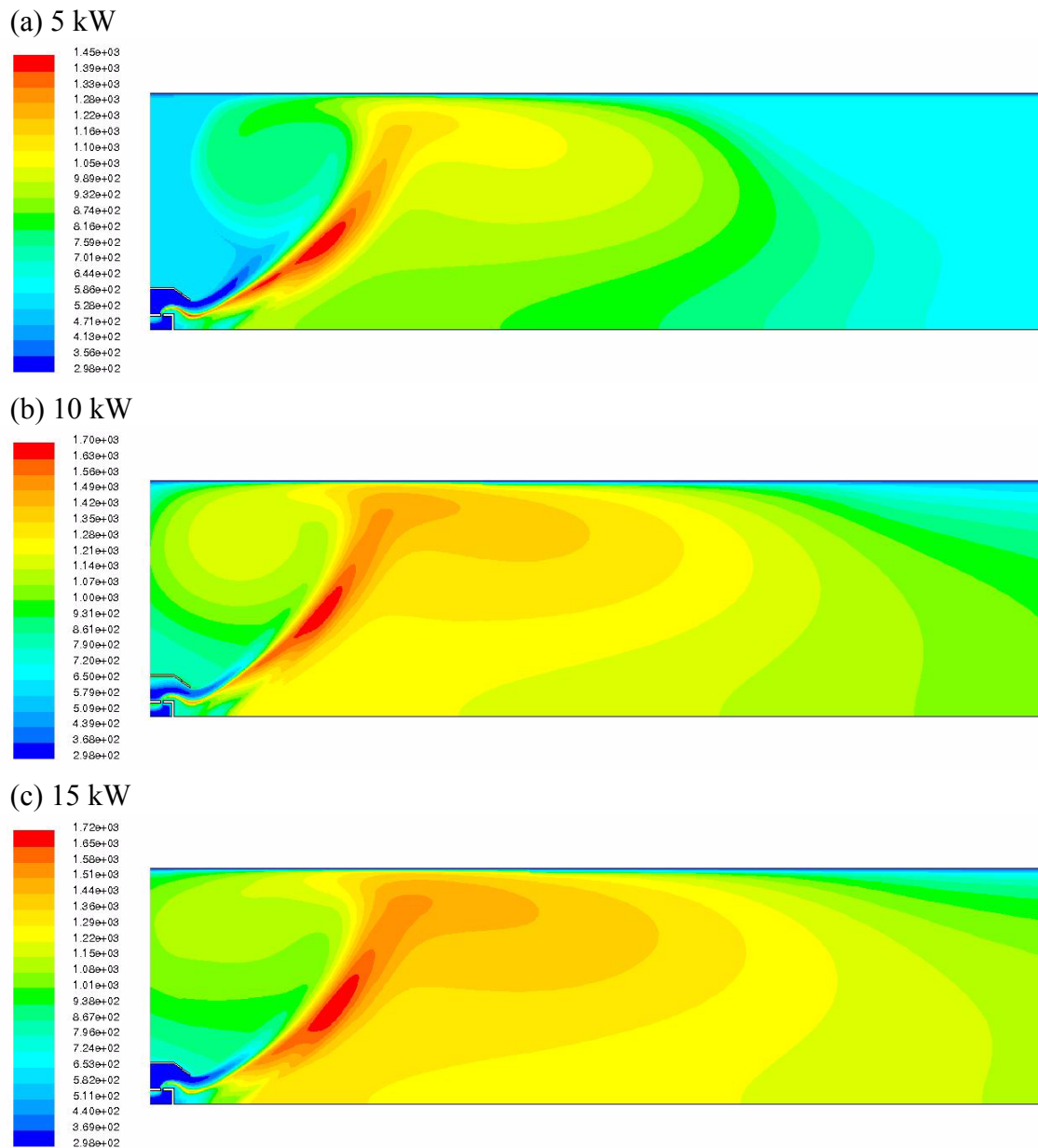
(a) 5 kW

(b) 10 kW

(c) 15 kW

Figure 5–13 Computed temperatures (K) in the Swirl Burner; (a) 5 kW; (b) 10 kW; (c) 15 kW.

5.5 Comparison of computed OH concentrations with OH concentrations measured by LIF

2D contour plots of the predicted OH concentrations for the 5 kW, 10 kW and 15 kW flames in the Swirl Burner are displayed in figure 5–14. These plots can be qualitatively compared with the 2D contour plots of the OH concentrations measured by LIF found in figure 4–15, figure 4–16 and figure 4–17. The computed OH concentrations are compared with the experimentally found OH concentrations in the plots in figure 5–15, figure 5–16 and figure 5–17 for the 5 kW, 10 kW and 13/15 kW flames respectively where the computed and measured OH concentrations are plotted at various heights above the burner, from 0 mm to 100 mm. The computed OH concentrations in the 15 kW flame are compared with the 13 kW experimental flame due to problems with blow-off at 15 kW and

higher throughputs as described in chapter 4.5.

By qualitatively comparing the 2D plots of the OH concentrations predicted by FLUENT (figure 5–14) with the corresponding experimentally achieved 2D OH plots (figure 4–15 to figure 4–17), it is seen that FLUENT does not manage to recreate the same shape of the flames found experimentally, neither does FLUENT manage to predict the change in flame shape seen from the 5 kW flame to the 10 kW and the 13 kW flame. FLUENT suggests instead a "flower"-shape for all these flames. The flames predicted by computations have a much more divergent shape than the flames measured by OH LIF. The radius of the computed flames increase with distance away from the burner and the flames seems to be limited radially only by the combustion chamber walls, which are 100 mm in radius. In contrast, the experiments show that the flame radius do not exceed 30 mm.

Computations indicate that the regions of significant OH concentrations in the flames are divided. As seen in figure 5–14, there is an outer OH zone surrounding an inner OH zone in the computed flames which can not be seen from the experiments. These OH zones can also be seen in figure 5–15 through to figure 5–17 where the LIF measured radial OH profiles appear as more smoothed than the computed profiles. The experimental data consists of time-averaged measurements in a turbulent flow field and the equipment used for LIF measurements of OH would not be able to resolve these OH zones inside the flame in the same way as seen from the computations.

From experiments it is seen that the Swirl Burner flames are lifted. By studying figure 4–15 through to figure 4–17, the lift-off heights in the Swirl Burner can be seen to vary from 20 mm at 5 kW to 5 mm at 10 kW and about 25 mm at 13 kW. The computed OH concentrations plotted in figure 5–14 reveal that there is some OH present near the fuel nozzles, but significant OH concentrations as that found in the flame front, appear first at a distance about one burner radius (17 mm) downstream of the burner exit. The computations did not manage to predict the change in lift-off height with varying thermal throughput.

A more detailed comparison of the OH concentrations computed in FLUENT and the OH concentrations measured using LIF are presented by the plots in figure 5–15, figure 5–16 and figure 5–17. Firstly, it can be noticed that both the computed and the measured OH concentrations are in the same order of magnitude. It is seen that the peak OH concentration from the computations increase with increasing thermal throughput. On the other side, the measured OH concentrations in these flames follows the opposite trend, the OH concentration is reduced with increased thermal throughput. The difference between the OH trend for the computed and experimental OH data might be explained with discrepancies in the experimental data. The LIF measurements described in chapter 4.5 are very sensitive to the energy content of the laser source which was experienced to have significant day to day variations. When comparing experimentally achieved OH concentrations using this LIF setup, the variations in laser energy might introduce experimental errors larger than the differences between cases. As mentioned in chapter 4.5, the 13 kW flame was close to blow off which occurred at 15 kW. Operating the flame close to the blow off limit where the lift off height occasionally changed, might have caused further experimental errors to the measurement of this flame.

The plots in figure 5–15 through to figure 5–17 emphasise the difference in flame shape found by the computations and OH LIF measurements. From the 2D OH plots in figure 5–14 it was noticed that the computed flames appeared more divergent in shape than seen from experiments with the Swirl Burner flames (figure 4–15 to figure 4–17). At 40 mm above the burner and higher, the radial peak in the computed OH-profile departs further away radially, while the LIF-measured radial OH-profiles are fairly constant with respect

to position of the radial peak and shape from 40 mm above the burner and increasing distance away from the burner. From 30 mm above the burner and lower, some similarities in the computed and measured radial profiles can be seen. The computed profile is not as smooth as the LIF-profile but the OH profiles do have the same radial distribution, and the peaks can be found at about the same radial positions.

Compared with experiments, the computed 5 kW (figure 5–15) and 10 kW (figure 5–16) flames differ most in absolute OH concentrations, while the computed 15 kW flame (figure 5–17) predicts concentrations more in accordance with the OH level found by experiments. With respect to the shape of the flames, it is seen from both the radial OH profiles and the 2D OH plots that the computed 5 kW flame best predicts the shape of the experimental flame until the computed OH peak are shifted radially outward with increasing axial distance from the burner at about 50-60 mm above the burner. Also the 10 kW computed flame resembles similarities with the shape of the experimental flame. The 2D OH plot from LIF measurements in figure 4–16 indicates a "flower"-shape, but is still not as divergent as the computed flame seen in figure 5–14(b). From figure 5–16 it is seen for the 10 kW flame that from 40 mm above the burner and further away, the computed OH zone is radially shifted outwards and away from the measured OH zone. At 15 kW the computed flame is totally different in shape than the experimental 13 kW flame. The 13 kW experimental flame appear "lumped" in shape and the radial OH peak is found along the axis of the combustion chamber at all axial positions, while the shape of the computed 15 kW flame resembles the same divergent "flower"-shape as the other computed flames.
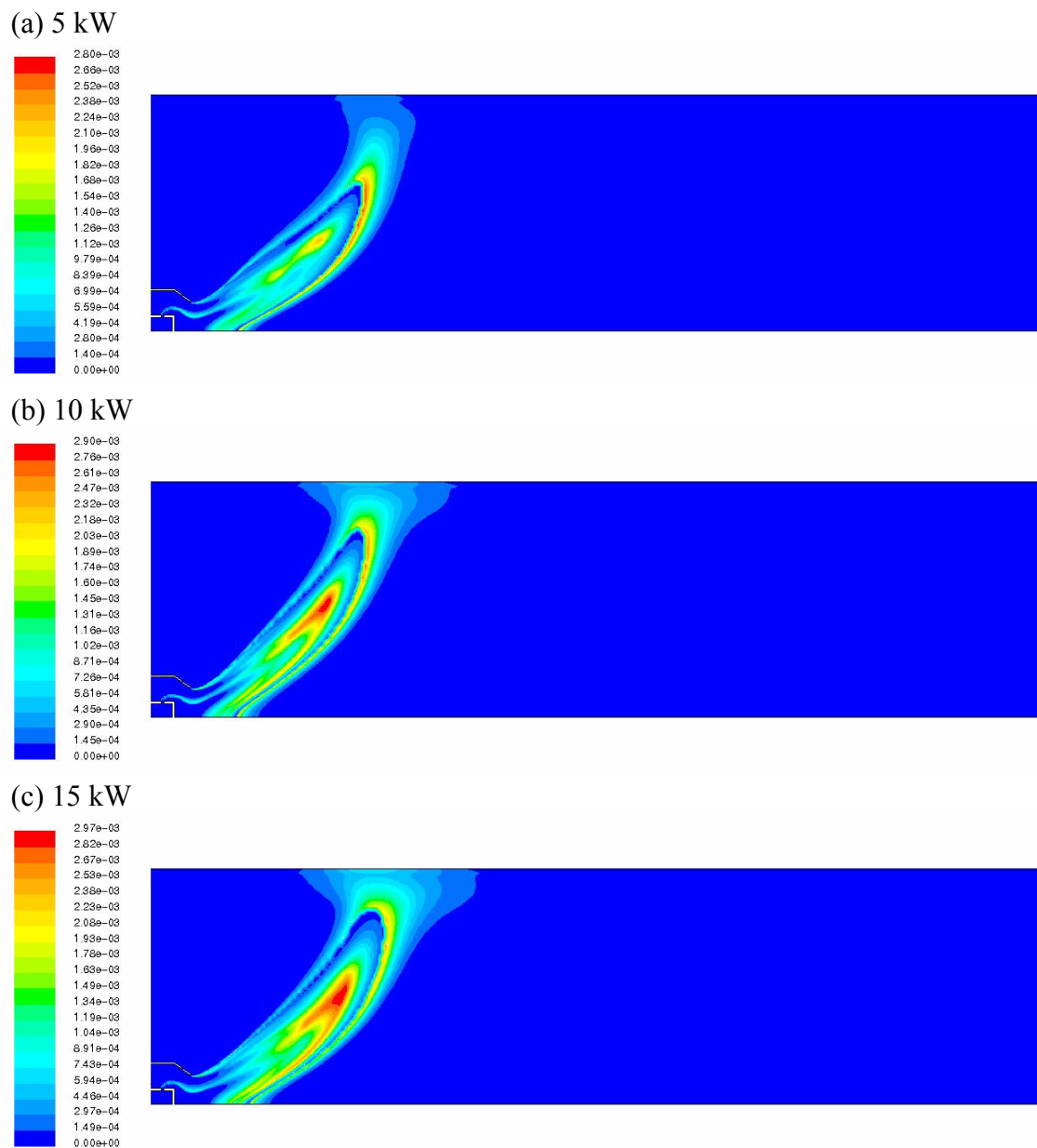
(a) 5 kW

(b) 10 kW

(c) 15 kW

Figure 5–14 Computed mole fractions of OH in the Swirl Burner; (a) 5 kW; (b) 10 kW; (c) 15 kW.
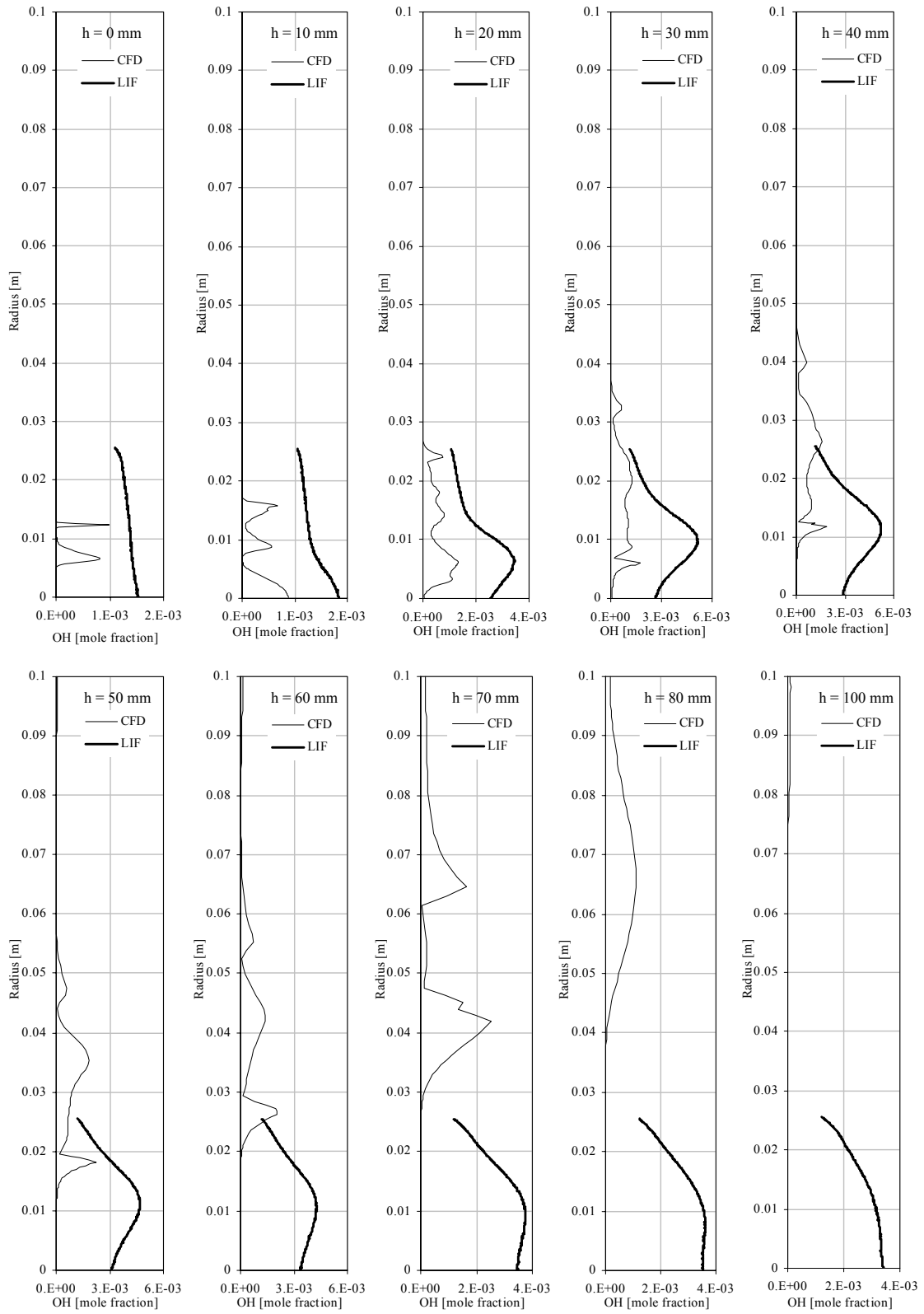
Figure 5–15 OH concentrations at various heights (h) above the burner; 5 kW.
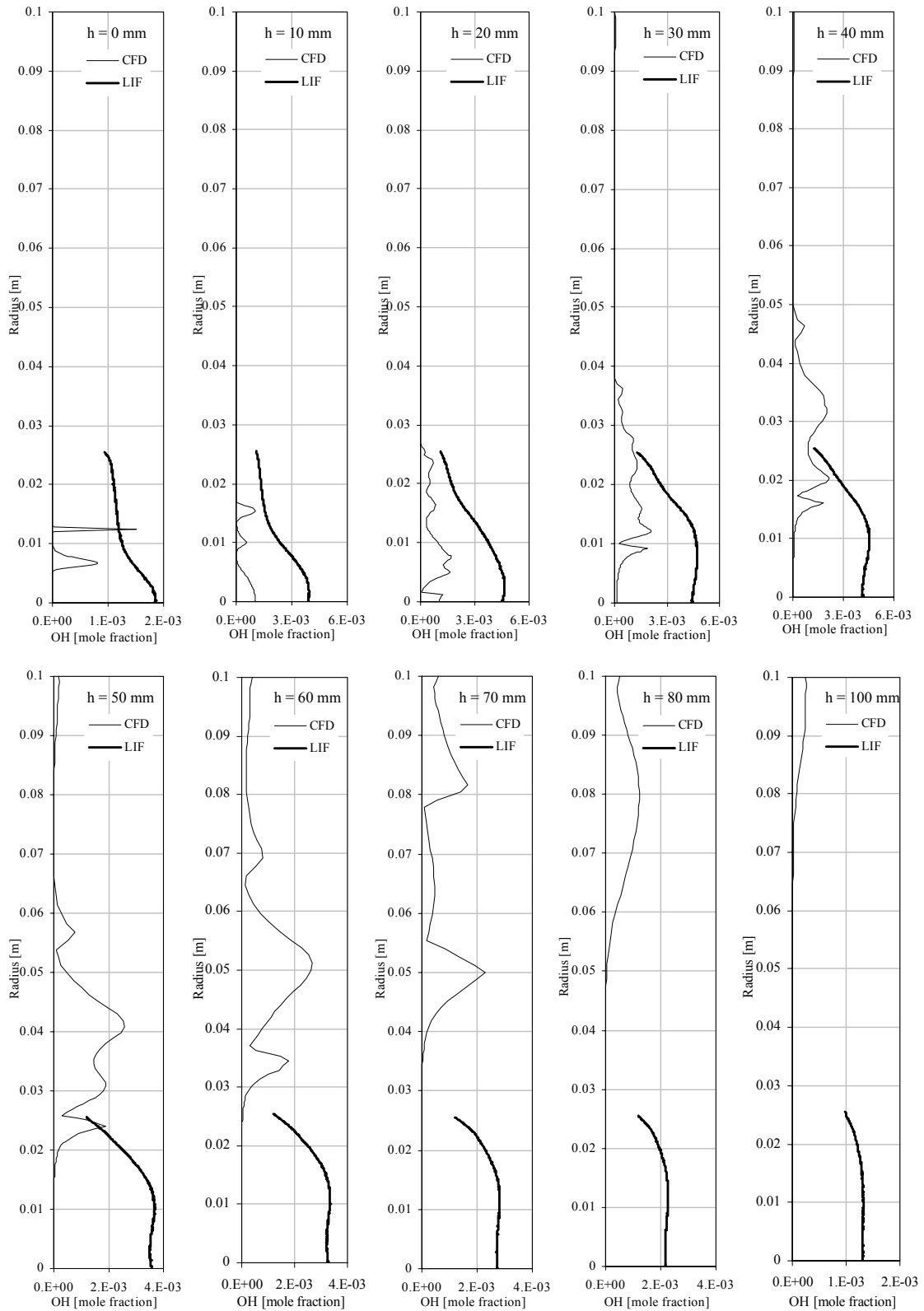
Figure 5–16 OH concentrations at various heights (h) above the burner; 10 kW.
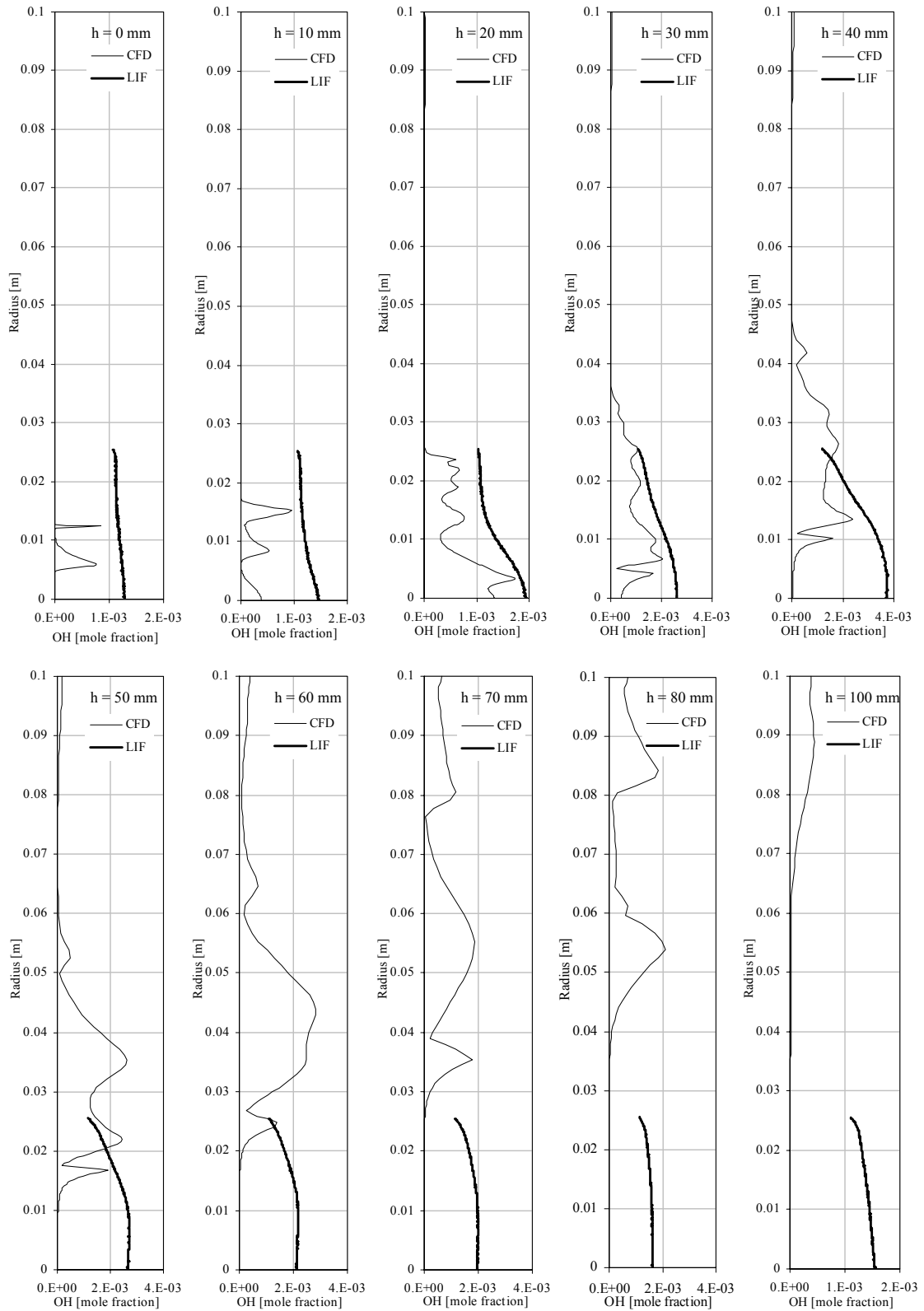
Figure 5–17 OH concentrations at various heights (h) above the burner; 13/15 kW.

5.6 NO$_x$ calculations

NO$_x$ concentrations were calculated from the converged reacting flow field solutions using a postprocessor based on the work of Al-Fawaz et al. (1994). The post-processing involves solving a transport equation for NO that takes into account convection, diffusion, production and consumption of NO and related species (Kyne et al., 2002). The NO transport equation is de-coupled from the main computations and can therefore be solved on the already converged solution for fluid flow and combustion. The NO mechanisms taken into account by the postprocessor are the thermal NO and the prompt NO mechanism. Formation of thermal NO is determined by the extended Zeldovich mechanism as described in chapter 2.2.2. The rate of prompt NO formation is calculated by the following equation (Fluent Inc., 2003):

$$\frac{d[NO]_{pr}}{dt} = fk_{pr}[O_2]^a[N_2][FUEL]e^{-E_a/(RT)} \qquad (5\text{--}3)$$

Where f is a correction factor that incorporates the effect of fuel type and equivalence ratio, k_{pr} is the rate coefficient, a is the oxygen reaction order, E_a is the activation energy and R is the universal gas constant.

NO concentrations predicted for the Swirl Burner are summarized in table 5–2. In this table, the maximum NO concentration and the NO concentration at the combustion chamber exit are given as total NO predicted and NO predicted by the prompt NO mechanism only. These NO concentrations are far too low compared with the measured NO emissions from this burner. In chapter 4.4, NO$_x$ emissions were measured in the range 20-35 ppmv dry using propane as fuel in the water-cooled combustion chamber (figure 4–10).

The NO$_x$ postprocessor has earlier been used by other workers for NO calculations in combustion (Kyne et al., 2002, Al Fawaz et al., 1994). Kyne et al. (2002) calculated NO in a gas turbine combustor where NO concentrations were found in the range 400-900 ppmv at temperatures as high as 2500 K. Al-Fawaz et al. (1994) measured and predicted NO$_x$ concentrations in a natural-gas burner in the range 50-90 ppmv with peak temperatures up to 2000 K. Al-Fawaz et al. (1994) found that the thermal NO accounted for about 80% of the total NO in the burners. For the Swirl Burner computations presented here, the peak flame temperatures are much lower, from 1450 K at 5 kW to 1720 K at 15 kW (chapter 5.4). The temperatures represent averaged values and fluctuations due to turbulence are not included in the computations. This might have a great influence on the formation of thermal NO which is very temperature dependent. According to Turns (1995), the thermal NO mechanism does not contribute to the formation of NO at flame temperatures below 1800 K. This implies that the averaged temperatures predicted for the Swirl Burner are too low for the thermal NO mechanism to contribute to the formation of NO. Formation of NO via the prompt NO mechanism, on the other hand, is less dependent on temperature, but the prompt NO formation predicted here is still in negligible concentrations. From equation (5–3) it can be seen that the rate of prompt NO formation calculated, is dependent on the fuel concentration. The low prompt NO concentrations predicted, indicates that there are no regions rich enough in fuel to be favourable for the calculation of prompt NO formation by equation (5–3). This implies further that the mixing of fuel and air in the Swirl Burner is good.

The results presented here indicate that the flame temperatures predicted for the Swirl Burner are too low. The low prompt NO formation predicted implies that the mixing of

fuel and air is good enough to avoid fuel rich regions which would result in higher prompt NO formation predicted by equation (5–3). According to these results, the prompt NO formation in the Swirl Burner is negligible.

Table 5–2 Computed total and prompt NO$_x$, peak and at chamber exit [ppmv dry].

	Total NO, max.	Prompt NO, max.	Total NO, exit	Prompt NO, exit
5 kW	0.00042	0.00042	0.00013	0.00013
10 kW	0.00604	0.004662	0.00489	0.00361
15 kW	0.00767	0.00097	0.00578	0.00048

5.7   Summary and conclusions

A CFD model of the Swirl Burner has been tested and evaluated using FLUENT. The Swirl Burner was modelled using a 2D structured grid consisting of about 21000 cells with an average skewness of 0.1. Three turbulence models were tested on a cold flow with a flow rate equivalent to 10 kW. These were the *k*-ε model, the *RNG k*-ε model and the Reynolds stress model (RSM). Based on an evaluation of the models ability to predict a central toroidal recirculation zone (CTRZ) of this strong swirling flow (*S* > 0.6) and recommendations from literature, the RSM was chosen for further modelling of the reacting flow. With the RSM turbulence model, three different combustion models were tested. These models were the Eddy Dissipation model, the PDF-based Equilibrium model and the PDF-based Flamelet model. Of the reaction models, the Eddy Dissipation model predicted peak flame temperatures higher than the adiabatic flame temperature for a propane-air mixture and was therefore dismissed. The Flamelet PDF model was chosen for the modelling of the Swirl Burner due to its ability to account for non-equilibrium chemistry. The decision of choosing the Flamelet PDF model was also based on recommendations found in literature. A major weakness of the evaluation of turbulence and combustion models was the lack of experimental measurements of velocities and in-flame temperatures.

Reacting flow in the Swirl Burner was modelled at 5 kW, 10 kW and 15 kW with the RSM to model turbulence and the Flamelet PDF model for the combustion chemistry. It was found that the CTRZ did not change in shape or size with thermal throughout, but the swirl velocity and the amount of mass recirculated into the CTRZ was increased with increasing thermal throughput. It was found difficult to reach convergence for the 5 kW flame. This might be caused by flame instabilities as observed experimentally with the same flame. Temperatures of the recirculated combustion products were predicted considerably lower for the 5 kW flame than the other flames. Flame instabilities observed experimentally and the convergence problems mentioned here might have been caused by the low flame temperatures and the reduced amount of recirculated gases for the 5 kW flame.

OH concentrations predicted here do not follow the same trends as seen from OH LIF measurements. The 2D OH contour plots from computations indicate that the flames have the same "flower"-shaped divergent flow at all thermal throughputs considered. The CFD calculations do not predict the change in flame shape as seen experimentally, but the absolute OH concentrations predicted by computations are in the same range as the concentrations found by experiments.

A NO$_x$ postprocessor was applied to the converged solutions of the reacting flow field to calculate the thermal and prompt NO formation in the Swirl Burner flames. Negligible concentrations of thermal NO and prompt NO were predicted. For the flames considered,

temperatures predicted by the Flamelet PDF model were below 1800 K which is a threshold temperature for the thermal NO mechanism (Turns, 1995). The thermal NO concentrations found implies that the flame temperatures predicted by the Flamelet PDF model are too low. The prompt NO, calculated by equation (5–3), was also found in negligible concentrations. This implies good mixing of fuel and air without fuel-rich regions favourable for prompt NO formation.

6   *Conclusions and recommendations for further work*

6.1   Conclusions

6.1.1   Introduction

A novel low NO_x swirl burner concept for fan driven gas burners has been studied experimentally, theoretically and numerically. The main conclusions from this study are drawn in the following.

6.1.2   200 kW burner testing and optimizing

A Swirl Burner with 200 kW nominal thermal throughput has been tested and optimized with propane and methane as fuel. The geometrical burner configuration has been varied to find the best arrangement of fuel nozzles, swirl vanes (swirl number) and position of the gas tube regarding emissions of NO_x, burner stability and the air and fuel supply pressure.

Using propane as fuel, the 200 kW Swirl Burner has been tested in the CEN boiler with thermal throughput in the range 80 kW to 240 kW and in the Vertical boiler up to 320 kW, which corresponds to a turn down ratio of 4:1. The 200 kW burner has been operated stable with excess air in the range 1-5% O_2 in the flue gases ($\lambda = 1.05$-1.30).

NO_x emissions measured from the optimized 200 kW Swirl Burner in the CEN boiler using propane as fuel were 31 to 45 ppmv dry corrected to 3% O_2 in the flue gases, with thermal throughput in the range 80-240 kW. Using methane as fuel, NO_x emissions from the Swirl Burner measured in the same boiler were 16 ppmv dry corrected to 3% O_2 in the flue gases at 120 kW thermal throughput.

6.1.3   Burner Scaling

The constant velocity scaling approach was applied for scaling the Swirl Burner to a 20 kW and a 370 kW burner using the 200 kW burner dimensions as basis. The 370 kW burner was operated stable while the 20 kW burner had a limited throughput range of stable operation. The fuel to air momentum was found to be an important parameter to be preserved while scaling the Swirl Burner.

The 370 kW burner has been tested in the Vertical boiler using propane as fuel with thermal throughput in the range 300 kW to 550 kW. The possible operation range for this burner is believed to be larger. The burner was operated stable with excess air level in the range 1-5% O_2 in the flue gases ($\lambda = 1.05$-1.30), but with excessive amounts of CO emissions at 1% O_2 in the flue gases. The emissions of NO_x were measured from 34 to 44 ppmv dry corrected to 3% O_2 in the flue gases.

The 20 kW burner has been tested with both propane and methane as fuel in an un-cooled combustion chamber and only with propane as fuel in a water-cooled combustion chamber. In the un-cooled combustion chamber, the burner was operated with thermal throughput in the ranges 5-20 kW and 10-20 kW using propane and methane as fuel respectively. In the water-cooled combustion chamber, the burner was operated with thermal throughput in the range 5-17 kW using propane as fuel. The burner could not be ignited in the water-cooled combustion chamber using methane. The 20 kW burner was in general found less stable than the larger burners. Emissions of NO_x were measured in the un-cooled combustion chamber in the ranges 32-45 and 18-25 ppmv dry corrected to 3% O_2 in the flue gases with propane and methane as fuel respectively. Emissions measured in the water-cooled combustion chamber were in the range 16-35 ppmv dry corrected to 3%

O_2 in the flue gases with propane as fuel.

NO_x emissions measured from the three Swirl Burners were found to scale with the following correlation from Weber (1996):

$$EI_{NOx}\rho_0 u_0 / d_0 \ = \ C \times Fr^{0.6} \qquad\qquad (6\text{--}1)$$

Where the constant (*C*) is inversely proportional to the post-flame heat extraction. The 200 kW burner in the CEN boiler and the 370 kW burner in the Vertical boiler were found to have a constant heat extraction with varying thermal throughput. The NO_x emissions from these burners could be fitted into equation (6–1) with a value of 23.2 for *C*. The NO_x emissions measured from the 20 kW burner in the water-cooled combustion chamber could not be fitted into equation (6–1) by a constant value of *C* due to increasing heat extraction with thermal throughput. The results from the burner scaling imply that the flame volume is the leading-order parameter for NO_x formation in the Swirl Burner.

It has been found that emissions of NO_x are reduced with increasing confinement ratio due to increased post-flame heat extraction. It has also been found that a high heat extraction caused by a high confinement ratio and too cold combustion chamber walls, can cause flame instabilities.

6.1.4 Non-intrusive OH measurements in the 20 kW burner

In-flame OH measurements have been made using the non-intrusive Laser Induced Fluorescence (LIF) technique. For the OH LIF measurements, a correlation was found between the intensity of fluorescence light emitted from the flame and detected by the ICCD camera, and the theoretical OH mole fractions of the flame. This correlation is given by equation (4–1).

LIF measurements were made in a water-cooled combustion chamber, custom made with optical access for this purpose, with the 20 kW burner using propane as fuel. By using the OH radicals as an indicator for the flame front, the flame size and shape has been visualized. It was found that the flame became more compact and was reduced in volume with increasing thermal throughput. The fact that the emissions of NO_x were reduced with increasing thermal throughput, supports the conclusion that the flame volume is the leading-order parameter for formation of NO_x in the Swirl Burner.

An attempt was made to measure flame temperatures using the OH LIF technique. By measuring the emitted light intensity from two different transitions in the OH spectrum, temperatures can be found from the intensity ratio. This attempt did not succeed due to limitations on the LIF equipment used.

6.1.5 CFD models evaluation

For modelling of the 20 kW Swirl Burner using FLUENT (Fluent Inc., 2003), a 2D structured grid consisting of about 21000 cells with an average skewness of 0.1 was made. Three turbulence models were evaluated for modelling of the swirling flow; these were the *k*-ε model, the RNG *k*-ε model and the Reynolds stress model (RSM). For modelling of the reacting flow, three combustion models were also evaluated; these were the Eddy Dissipation model, the PDF-based Equilibrium model and the PDF-based Flamelet model. The RSM was found to be the best model for turbulence and the PDF-based Flamelet model best for modelling combustion. The evaluation was based on computational results achieved with these models and recommendations found in literature. A weakness of this evaluation was the lack of experimental measurements of velocities and in-flame temperatures.

6.1.6 CFD modelling of the 20 kW burner

The 20 kW Swirl Burner has been modelled at thermal throughput of 5 kW, 10 kW and 15 kW with the RSM for turbulence and the PDF Flamelet model for combustion.

The CTRZ was not found to change in shape or size with thermal throughout, but the swirl velocity and the amount of mass recirculated into the CTRZ was increased with increasing thermal throughput. Flame temperatures predicted at 5 kW were considerably lower than at higher thermal throughput. Low flame temperature can cause flame instabilities as observed experimentally.

Predicted OH concentrations have been compared with OH LIF measurements. The computations do not predict the change in flame shape as seen from LIF measurements, but the predicted OH concentrations are in the same range as concentrations found experimentally.

Negligible concentrations of NO_x, thermal and prompt, were predicted by the computations. Due to the low temperatures predicted by the Flamelet PDF model (<1800 K), no thermal NO was predicted. The negligible amounts of prompt NO, calculated by equation (5–3), were caused by the absence of fuel-rich regions, favourable to prompt NO formation, in the calculated flow.

6.2 Recommendations for further work

The Swirl Burner has been scaled from a 200 kW burner down to a 20 kW burner and up to a 370 kW burner. The maximum thermal throughput tested with the 370 kW burner was limited by the Vertical boiler. For further work, this burner should be tested in a boiler with higher capacity to find the maximum possible turndown ratio of the burner. This will also indicate if the NO_x emissions from the 370 kW burner continue to scale with a constant value of C in equation (4–5) when increasing the thermal throughput.

The scaling results so far are encouraging, and further experiments with a larger scaled burner would be very interesting. This can verify if the NO_x scaling correlation by Weber (1996) still holds for an even larger Swirl Burner. To make this possible, a boiler with higher capacity than the Vertical boiler is needed.

The 20 kW burner was found to have a limited operation range with regards to thermal throughput in the water-cooled combustion chamber. For further experiments with this burner, the fuel nozzle configuration can be changed to increase the fuel nozzle velocity. It has been concluded here, that the fuel to air momentum ratio is an important parameter when scaling the Swirl Burner. Experiments with an increased fuel nozzle velocity in the 20 kW burner can further investigate this and possibly improve stability of this burner.

LIF measurements of OH flame radicals were carried out by traversing a laser beam through the flame, and 2D images were created by post-processing the results from these measurements. The OH measurements can be improved by using 2D LIF equipment, where OH radicals are exited by a laser sheet instead of a single beam. With laser sheets, it can be easier to achieve more accurate 2D images of the flame radicals, and hence the flame front.

Inaccuracies were introduced to the LIF measurements by the Nd:YAG laser source and the tunable dye laser. With the laser setup used, the energy content of the tuned laser beam and the wavelength of this had to be calibrated for every experiment. By using a state of the art laser setup, this calibration can be avoided.

An attempt was made to measure the flame temperatures using the LIF setup, but this did not succeed. Temperature is an important flame parameter, and for further work, it would be very interesting to measure the flame temperatures in the Swirl Burner with an improved LIF setup. Temperature measurements would be useful for validating CFD calculations as well.

Measurements of other flame species than OH with non-intrusive laser techniques, such as NO and CH, would be very valuable for further understanding of the Swirl Burner and for validation of CFD calculations.

Temperatures predicted by CFD were too low to predict any thermal NO formation in the Swirl Burner. For further work with FLUENT, this should be further investigated and if possible improve the temperatures predicted. The temperature calculations should be compared with flame temperatures measured with either laser techniques (see above) or with a thermocouple.

The Flame front visualized by the computed OH concentrations, did not compare directly with the flame front visualized by the OH radicals measured using LIF. Further work with FLUENT can be done to improve these results, since a better CFD solution of the reacting flow will give a much better understanding of the Swirl Burner.

More experimental work can be carried out to support the choice made of turbulence and combustion models used to model the Swirl Burner. For turbulence models, this might be velocity measurements in a cold flow. This can be done with a non-intrusive technique, such as Laser Doppler Velocimetry, where point-measurements of fluid velocity are made in one, two or three dimensions. For combustion models, this can be measurements of flame temperatures as mentioned above.

An improvement of the Swirl Burner CFD calculations worth considering for further work, is modelling of the turbulent reacting flow in three dimensions, as the calculations presented here are made only for two dimensions. Modelling of the Swirl Burner using Large Eddy Simulation instead of Reynolds Averaged Navier Stokes might produce better predictions of the swirling flow and might also be worthwhile to consider for further work. Large Eddy Simulation will be available in the next version of FLUENT (Diana, 2004). If the Swirl Burner computations can be further improved, a study of the effect of confinement ratio of the different burners using CFD might be an interesting topic for further work.

References

Al-Fawaz, A. D., Dearden, L. M., Hedley, J. T., Missaghi, M., Pourkashanian, M., Williams, A. and Yap, L. T. (1994). NO_x formation in geometrically scaled gas-fired industrial burners. 25th Symposium (International) on Combustion, The Combustion Institute, Pittsburgh, 1027-1034.

Arnold, A., Bombach, R., Käppeli, B. and Schlegel, A. (1997). Quantitative measurements of OH concentration fields by two-dimensional laser-induced fluorescence. Applied Physics B, vol. 64, 579-583.

Benim, A. C. (1990). Finite element analysis of confined turbulent swirling flows. International Journal for Numerical methods in Fluids, vol. 11, 697-717.

Bjerketvedt, D., Bakke, J. R. and van Wingerden, K. (1993). *Gas Explosion Handbook, Version 1.2*, Bergen: Christian Michelsen Research, CMR-93-A25034.

Bollettini, U., Breussin, F. N. and Weber, R. (2000). A study on scaling of natural gas burners. IFRF Combustion Journal, July 2000, art. no. 200006.

Bombach, R. and Käppeli, B. (1999). Simultaneous visualisation of transient species in flames by planar-laser-induced fluorescence using a single laser system. Applied Physics B, vol. 68, 251-255.

Borghi, R. (1988). Turbulent Combustion Modelling. Progress in energy and Combustion Science, vol. 14, 245-292.

Bowman, C.T. (1992). Control of Combustion-generated Nitrogen Oxide Emissions: Technology Driven by Regulation. 24th Symposium (International) on Combustion, The Combustion Institute, Pittsburgh, 859-878.

Brownsword, R. A., Hillenkamp, M., Schmiechen, P., Volpp, H.-R. and Wolfrum, J. (1997). The dynamics of the OH + HD gas-phase reaction: absolute reaction cross section and H/D atom product branching ratio. Chemical Physics Letters, vol. 275, 325-331.

Choudhury, D. (1993). *Introduction to the Renormalization Group Method and Turbulence Modeling.* Lebanon: Fluent Inc. Technical Memorandum TM-107.

Comité Européen de Normalisation (1998). Heating boilers - Part 3: Gas-fired central heating boilers - Assembly comprising a boiler body and a forced draught burner. European Standard EN 303-3:1998.

Correa, S. M. and Shyy, W. (1987). Computational Models and methods for Continuous Gaseous Turbulent Combustion. Progress in energy and Combustion Science, vol. 13, 249-292.

Daily, J. W. (1997). Laser Induced Fluorescence Spectroscopy in Flames. Progress in energy and combustion science, vol. 23, 133-199.

Diana, N. (2004). What's New in FLUENT 6.2. Fluent news, vol. 13, no. 1, 42-43.

Durbin, P. A. and Speziale C. G. (1991). Local Anisotropy in Strained Turbulence at High Reynolds Numbers. Journal of Fluids Engineering, vol. 113, 707-709.

Eckbreth, A. C. (1996). *Laser diagnostics for combustion temperature and species.* 2nd ed. Tunbridge Wells Kent: Abacus Press. ISBN 2-88449-225-9.

Egerter, A. C. (1957). Editorial. Combustion and Flame, vol. 1, 1-2.

Engdar, U. and Klingmann, J. (2002). Investigation of two-equation turbulence models applied to a confined axis-symmetric swirling flow. American Society of Mechanical Engineers, Pressure Vessels and Piping Division (Publication) PVP, vol. 448, no. 2, 199-206.

European Commission (2003). Integrated Pollution Prevention and Control (IPPC) Draft Reference Document on Best Available Techniques for Large Combustion Plants Draft March 2003. European IPPC Bureau, Seville. < http://eippcb.jrc.es/> [Accessed March 2004].

Fenimore, C. P. (1971). Formation of Nitric Oxide in Premixed Hydrocarbon Flames. 13th Symposium (International) on Combustion, The Combustion Institute, Pittsburgh, 373-380.

Ferziger, J. H. and Peric, M. (2002). *Computational Methods for Fluid Dynamics*, 3rd ed. Berlin Heidelberg New York: Springer-Verlag. ISBN 3-540-42074-6.

Fluent Inc. (2003). *Fluent 6.1 User's Guide*, Lebanon: Fluent Inc.

Goldin, G. and Choudhury, D. (2001). Steady-state simulation of a methane-air partially premixed turbulent flame. American Society of Mechanical Engineers, Heat Transfer Division, (Publication) HTD, vol. 369, no. 4, 57-63.

Griffiths, J.F. and Barnard, J.A. (1995). *Flame and combustion*, 3rd ed. London: Blackie Academic Professional. ISBN 0-7514-0199-4.

Gupta, A. K., Lilley, D. G. and Syred, N. (1984). *Swirl Flows*. Tunbridge Wells: Abacus Press. ISBN 0-85626-175-0.

Gülder, Ö. L., Smallwood, G. J., Wong, R., Snelling, D. R., Smith, R., Deschamps, B. M. and Sautet, J. -C. (2000). Flame front surface characteristics in turbulent premixed propane/air combustion. Combustion and Flame, vol. 120, no. 4, 407-416.

Hanjalic, K. (2002). Turbulence Closure Models. In: Benocci, C. and van Beeck, J. P. A. J. (eds.), *von Karman Institute for Fluid Dynamics Lecture Series 2002-02*, March 18-22, 2002.

Hottel and Hawthorne (1949). Diffusion in Laminar Flame Jets. 3rd Symposium (International) on Combustion, The Combustion Institute, Pittsburgh, 254-266.

Hughes, K. J., Turányi, T., Clague, A. and Pilling, M. J. (2001). Development and testing of a comprehensive chemical mechanism for the oxidation of methane. International Journal of Chemical Kinetics, vol. 33, 513-538.

Jaw, S. Y. and Chen, C. J. (1998). Present Status of Second-Order Closure Turbulence Models. I: Overview. Journal of Engineering Mechanics, vol. 124, no. 5, 485-501.

Jones, W. P. (1994). Turbulence modelling and numerical solution methods for variable density and combusting flows. In: Libby, P. A. and Williams, F. A. (eds.), *Turbulent re-*

REFERENCES

acting flows. London: Academic Press, 309-374. ISBN 0-12-447945-6.

Jones, W. P. and Launder, B. E. (1972). The Prediction of Laminarization with a Two-Equation Model of Turbulence. International Journal of Heat and Mass Transfer, vol. 15, 301-314.

Jones, W. P. and Whitelaw, J. H. (1982). Calculation Methods for Reacting Turbulent Flows: A Review. Combustion and Flame, vol. 48, 1-26.

Kaskan, W. E. (1957). The Dependence of Flame Temperature on Mass Burning Velocity. Sixth Symposium (International) on Combustion, The Combustion Institute, Pittsburgh, 134-143.

Kee, R. J., Grcar, J. F., Smooke, M. D. and Miller, J. A. (1985). A Fortran Program for Modeling Steady Laminar One-Dimensional Premixed Flames. Sandia Report, SAND85-8240.

Kohse-Höinghaus, K. (1994). Laser Techniques for the Quantitative Detection of Reactive Intermediates in Combustion Systems. Progress in energy and Combustion Science, vol. 20, 203-279.

Kuo, K. K. Y. (1986). *Principles of Combustion*. New York: John Wiley and Sons. ISBN: 0-471-62605-8.

Kyne, A. G. (2001). Experimental and Theoretical Investigation of the Oxidation of Kerosene. PhD thesis, University of Leeds (Department of Fuel and Energy), Leeds.

Kyne, A. G., Pourkashanian, M., Wilson, C. W. and Williams, A. (2002). Validation of a flamelet approach to modelling 3-D turbulent combustion within an airspray combustor. American Society of Mechanical Engineers, International Gas Turbine Institute, Turbo Expo (Publication) IGTI, vol. 1, 591-600.

Launder, B. E. (1989). Second-moment closure and its use in modelling turbulent industrial flows. International Journal for Numerical Methods in Fluids, vol. 9, 963-985.

Launder, B. E., Reece, G. J. and Rodi, W. (1975). Progress in the development of a Reynolds-stress turbulence closure. Journal of Fluid Mechanics, vol. 68, 537-566.

Launder, B. E. and Spalding, D. B. (1974). The Numerical Computation of Turbulent Flows. Computer methods in Applied Mechanics and Engineering, vol. 3, 269-289.

Lefebvre, A. H. (1983). *Gas Turbine Combustion*. New York: Hemisphere Publishing Company. ISBN: 0-89116-896-6.

Li, S. C. and Williams, F. A. (1999). NO_x Formation in Two-Stage Methane-Air Flames. Combustion and Flame, vol. 188, 399-414.

Luque, J. and Crosley, D. R. (1999). LIFBASE: Database and Spectral Simulation Program (Version 1.5). SRI International Report MP 99-009.

Magnussen, B. F. and Hjertager, B. H. (1976). On mathematical modeling of turbulent combustion with special emphasis on soot formation and combustion. 16th Symposium (International) on Combustion, The Combustion Institute, Pittsburgh, 719-729.

Mathieu, J. and Scott, J. (2000). *An introduction to Turbulent Flow*. Cambridge: Cambridge University Press. ISBN 0-521-57066-2.

Meier, U. E., Wolff-Gaßmann, D. and Stricker, W. (2000). LIF imaging and 2D temperature mapping in a model combustor at elevated pressure. Aerospace science and technology, vol. 4, 403-414.

Müller, E. (2002). Environmental Labelling, Innovation and the Toolbox of Environmental Policy - Lessons Learned from the German Blue Angel Program. Federation of German Consumer Organisations, Markgrafenstr. 66, D - 10969 Berlin, August 2002.

Nikjooy, M. and Mongia, H. C. (1991). International Journal of Heat and Fluid Flow, vol. 12, no. 1, 12-19.

Patankar, S. V. and Spalding, D. B. (1972). A calculation procedure for heat, mass and momentum transfer in three-dimensional parabolic flows. International Journal of Heat and Mass Transfer, vol. 15, no. 10, 1787-1806.

Peters, N. (1984). Laminar diffusion flamelet models in non-premixed turbulent combustion. Progress in Energy and Combustion Science, vol. 10, 319-339.

Peters, N. (1986). Laminar flamelet concepts in turbulent combustion. 21th Symposium (International) on Combustion, The Combustion Institute, Pittsburgh, 1231-1250.

Peters, N. (2000). *Turbulent combustion*. Cambridge: Cambridge University Press. ISBN 0-521-66082-3.

Price, G. R., Botros, K. K. and Goldin, G. M. (2002). CFD predictions and field measurements of NO_x emissions from LM1600 gas turbine during part load operation. Journal of Engineering for Gas Turbines and Power, vol. 124, no. 2, 276-283.

Røkke, N. A. (1994). Experimental and Theoretical Studies of Environmental Aspects of Natural Gas Combustion. PhD thesis, Norwegian Institute of Technology, Trondheim. ISBN: 82-7119-702-9.

Røkke, N. A., Hustad, J. E. and Jacobsen, M. (1993). Emissions from Buoyancy Dominated Gas/Oil Turbulent-Jet Diffusion Flames. Proceeding of the 2nd International Conference on Combustion Technologies for a Clean Environment, Lisboa, Portugal.

Røkke, N. A., Hustad, J. E. and Sønju, O. K. (1994). A Study of Partially Premixed Unconfined Propane Flames. Combustion and Flame, vol. 97, 88-106.

Røkke, N. A., Hustad, J. E., Sønju, O. K. and Williams, F. A. (1992). Scaling of nitric oxide emissions from buoyancy-dominated hydrocarbon turbulent-jet diffusion flames. 24th Symposium (International) on Combustion, The Combustion Institute, Pittsburgh, 385-393.

Rørtveit, G. J., Zepter, K., Skreiberg, Ø., Fossum, M. and Hustad, J. E. (2002). A comparison of low-NO_x burners for combustion of methane and hydrogen mixtures. 29th Symposium (International) on Combustion, The Combustion Institute, Pittsburgh, 1123-1129.

Sayre, A., Lallemant, N., Dugué, J. and Weber, R. (1994). Effect of radiation on nitrogen oxide emissions from nonsooty swirling flames of natural gas. 25th Symposium (In-

ternational) on Combustion, The Combustion Institute, Pittsburgh, 235-242.

Serway, R. A. (1996). *Physics for scientists and engineers, with modern physics*, 4th ed. Philadelphia: Saunders College Publishing. ISBN Philadelphia.

SFT (2002). Miljøstatus i Norge <http://www.miljostatus.no/> [Accessed May 2004].

Sharif, M. A. R. and Wong, Y. K. E. (1995). Evaluation of the performance of three turbulence closure models in the prediction of confined swirling flows. Computers and Fluids, vol. 24, no. 1, 81-100.

Smith, G. P., Golden, D. M., Frenklach, M., Moriarty, N. W., Eiteneer, B., Goldenberg, M., Bowman, C. T., Hanson, R. K., Song, S., Gardiner, W. C., Lissianski, V. V. and Qin Z. (1999). GRI-Mech Version 3.0. http://www.me.berkeley.edu/gri_mech/.

Simmie, J. M. (2003). Detailed chemical kinetic models for the combustion of hydrocarbon fuels. Progress in Energy and Combustion Science, vol. 29, 599-634.

Spalding, D. B. (1976). Mathematical Models of Turbulent Flames; A review. Combustion Science and Technology, vol. 13, 3-25.

Spangelo, Ø., Slungaard, T., Engebretsen, T. and Sønju, O. K. (2003). Development of Low NO_x Swirl Burner for Gaseous Fuels. Proceeding of the 7th International Conference on Energy for a Clean Environment, Lisboa, Portugal.

Suris, A. L., Flankin, E. V. and Shorin, S. N. (1977). Length of free diffusion flames. Combustion, Explosion and Shock Waves, vol. 13, no. 4, 459-462.

Sønju, O. K. and Hustad, J. E. (1984). An Experimental Study of Turbulent Jet Diffusion Flames. Progress in Astronautics and Aeronautics Series, vol. 95, AIAA, 320-339.

Turns, S. R. (1995). Understanding NO_x formation in nonpremixed flames: Experiments and modeling. Progress in Energy and Combustion Science, vol. 21, no. 5, 361-385.

UNECE (2004). The 1999 Gothenburg Protocol to Abate Acidification, Eutrophication and Ground-level Ozone. <http://www.unece.org/> [Accessed March 2004].

U.S. Environmental Protection Agency (1998). NO_x - How Nitrogen Oxides Affect the Way We Live and Breathe. EPA Report, EPA-456/F-98-005.

Verboven, P., Scheerlinck, N., Baerdemaeker, J. D. and Nicolaï, B. M. (2000). Computational fluid dynamics modelling and validation of the isothermal airflow in a forced convection oven. Journal of Food Engineering, vol. 43, 41-53.

Warnatz, J., Maas, U. and Dibble, R. W. (1999). *Combustion, Physical and Chemical Fundamentals, Modelling and Simulation, Experiments, Pollutant Formation*, 2nd ed. Berlin Heidelberg New York: Springer-Verlag. ISBN 3-540-65228-0.

Widman, J. F., Charagundla, S. R. and Presser, C. (2000). Aerodynamic study of a vane-cascade swirl generator. Chemical Engineering Science, vol. 55, 5311-5320.

Weber, R. (1996).Scaling characteristics of aerodynamics, heat transfer, and pollutant emissions in industrial flames. 26th Symposium (International) on Combustion, The Combustion Institute, Pittsburgh, 3343-3354.

REFERENCES

Williams, F.A. (1985). *Combustion Theory: The Fundamental Theory of Chemically Reacting Flow Systems*, 2nd ed. Menlo Park, California: The Benjamin/Cummings Publishing Company Inc. ISBN 0-8053-9801-5.

Xia, J. L., Yadigaroglu, G., Liu, Y. S., Schmidli, J. and Smith, B. L. (1998). Numerical and experimental study of swirling flow in a model combustor. International Journal of Heat and Mass Transfer, vol. 41, no. 11, 1485-1497.

Xue, H. and Aggarwal, S. K. (2003). NOx emissions in n-heptane/air partially premixed flames. Combustion and Flame, vol. 132, 723-741.

Yakhot, V., Orszag, S. A., Thangam, S., Gatski, T. B. and Speziale, C. G. (1992). Development of turbulence models for shear flows by a double expansion technique. Physics of Fluids. A, Fluid dynamics, vol. 4, no. 7, 1510-1520.

Zeldovich, Y. B. (1946). The Oxidation of Nitrogen in Combustion and Explosions. Acta Physicochimica U.R.S.S., vol. 21, no. 4, 577-628.

Zepter, K. (2003). Design Aspects of a Low-NO_x Burner for a Stirling Engine. PhD thesis, The Norwegian University of Science and Technology, Trondheim. ISBN: 82-471-5555-9.

APPENDIX A - DEVELOPMENT OF LOW NO$_X$ SWIRL BURNER FOR GASEOUS FUELS

Spangelo, Ø., Slungaard, T., Engebretsen, T. and Sønju, O. K. (2003). Development of Low NO$_X$ Swirl Burner for Gaseous Fuels. Proceeding of the 7th International Conference on Energy for a Clean Environment, Lisboa, Portugal.
-Manuscript presented at conference, and article published in the proceedings as well as accepted for Clean Air - International Journal on Energy for a Clean Environment.

DEVELOPMENT OF LOW NO$_X$ SWIRL BURNER FOR GASEOUS FUELS

O. Spangelo, T. Slungaard, T. Engebretsen* and O. K. Sonju
Department of Energy and Process Engineering, Norwegian University of Science and Technology, 7491 Trondheim, Norway
*SINTEF Materials Technology AS, 7465 Trondheim, Norway

Abstract A research and development project has resulted in a new low NO$_x$ fan-driven burner-concept called the Swirl Burner. This patented concept is in the final stages of development. The Swirl Burner is a partially premixed fan driven gas burner with internal flue gas recirculation and possibilities for staged fuel and air supply. Gas mixing and flame stabilization is provided by a swirl generating device with aerodynamically shaped vanes positioned in an annular airflow. Flue gas is recirculated into the combustion zone, providing a continuous ignition source. NO$_x$ emissions in the range 30-40 ppmvd at 3% oxygen are measured for 100 - 200 kW with propane. Using methane as fuel, NO$_x$ emissions about 20 ppmvd at 3% oxygen are measured for 75-200 kW. CO emissions were kept below about 5 ppmvd. NO$_x$ and CO emissions were fairly constant over a wide range of fuel/air ratios. Similar results have also been obtained for a 20 kW burner and a 1 MW burner. In this paper a detailed characterisation of the 200 kW Swirl Burner and the experimental results will be presented.

Keywords combustion, swirl, NO$_x$ emissions, gas burners

INTRODUCTION

Nitrogen oxide is a main component in the formation of ground-level ozone, but can also react to form nitrate particles and acid aerosols, which together with NO$_2$ can effect human health by causing respiratory problems. Further, nitrogen oxides (denoted as NO$_x$) consisting of NO and NO$_2$, contributes to formation of acid rain and global warming [1]. Consequently, reduction of NO$_x$ formation has become a major topic in combustion research. Emission reductions can be achieved by understanding the chemical kinetics producing NO$_x$ and their interaction with fluid dynamics. Four main routes to formation of NO$_x$ are identified so far [2]. Both NO$_x$ formation mechanisms and reduction techniques important to fan driven gas burners are further discussed.

Development of low NO$_x$ gas burner technology is a research and development project at the Norwegian University of Science and Technology (NTNU) and SINTEF Energy Research AS. Within this project four fan driven gas

burner concepts have been tested and evaluated [3]. These were the Venturi Burner, the Swirl Burner, the Premixed Bluff-Body Burner and the Metal-Fibre Burner. A new fan with more uniform flow and higher pressure has also been developed. Of the concepts studied, the Swirl Burner might be the most promising, and seem to be able to compete with leading technology both for large industrial burners and for fan driven burners. This concept has been selected for further development and optimization.

The Swirl Burner is a patented concept in the final stages of development. In this paper, a detailed characterisation of the Swirl Burner and the experimental results will be presented as well as emissions for some typical existing low NO_x burners.

NO_X FORMATION MECHANISMS

Generally, when using a gaseous fuel, the main pollution components are NO_x, with NO as the dominating component. NO_x in gas combustion is mainly formed by three mechanisms: the thermal NO mechanism originally proposed by Zel'dovich [4], the prompt NO mechanism first postulated by Fenimore [5] and the nitrous oxide (N_2O) route to NO. The different mechanisms are affected in different ways by temperature, residence time, oxygen concentration and fuel type. Thermal NO and prompt NO are the most important for fan driven gas burners.

Thermal NO is formed by the following elementary reactions (extended Zel'dovich mechanism):

$$O + N_2 \rightarrow NO + N \tag{1}$$

$$N + O_2 \rightarrow NO + O \tag{2}$$

$$N + OH \rightarrow NO + H \tag{3}$$

where Equation (1) is the rate limiting step because of its high activation energy [6], requiring high temperatures to give any significant contribution to the total NO formation. From Equation (1) to (3) and the assumption that $d[N]/dt \approx 0$ it can be obtained for the NO formation that:

$$\frac{d[NO]}{dt} = 2k_1[O][N_2] \tag{4}$$

where [ ] denotes concentration and k_1 is the rate coefficient of the reaction in Equation (1). From Equation (4) and the temperature dependence of k_1, it can be shown that NO formation can be controlled by [O], [N_2], temperature and residence time. Thermal NO formation can, therefore, be minimized by reducing peak temperatures, by reducing oxygen levels especially at peak temperatures and by reducing the time of exposure to peak temperatures.

Prompt NO, identified by Fenimore [5], who suggested that hydrocarbon radicals reacted with molecular nitrogen in the primary reaction zone, explaining the promptly formation of NO not predicted by the thermal NO mechanism. According to [6], the prompt NO mechanism is a more complicated process than for the thermal NO. The prompt NO mechanism involves molecular nitrogen from the combustion air reacting with the CH radical, which is an intermediate at the flame front only, forming hydrocyanic acid (HCN), which further reacts to NO:
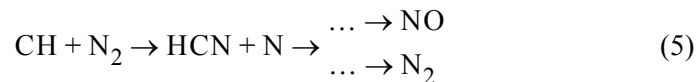
$$CH + N_2 \rightarrow HCN + N \rightarrow \begin{matrix} \dots \rightarrow NO \\ \dots \rightarrow N_2 \end{matrix} \qquad (5)$$

Prompt NO is favoured by fuel rich conditions and its formation takes place at lower temperatures (about 1000 K) than thermal NO.

NO formation by the nitrous oxide route increases in importance under conditions such as lean mixtures, high pressure and lower combustion temperatures [2]. This route is therefore more important in other applications, e.g. gas turbines, than in the burner considered here. Another mechanism, not considered to be of importance here, is conversion of fuel bound nitrogen to NO if the fuel contains nitrogen, which is the case especially for some liquid and solid fuels.

NO$_X$ REDUCTION TECHNIQUES

NO$_x$ formation can be controlled by different techniques. Most widely used primary measures are external and internal flue gas recirculation, staged combustion and different levels of premixing. External flue gas recirculation and secondary measures such as catalytic conversion and ammonia addition can be expensive, especially on small burners, and can be difficult to install on existing boilers. These techniques were, therefore, not further investigated. In the present work, a combination of techniques are sought utilised for lowest possible NO$_x$ formation.

Internal flue gas recirculation is achieved when reacted gas is recirculated towards the unreacted gas by a recirculating flow in the combustion chamber.

The recirculation is both an ignition source and provides inert gas to reduce the peak temperatures. Swirl generators, bluff bodies and other geometrical shapes and devices can be used to guide the flow and to generate a recirculating flow-field.

Staged combustion consists of adding fuel and air at different stages of the combustion process. One technique is to start with a fuel rich condition, then adding more air to create an oxygen rich condition. A third stage of adding more fuel can be used before the final equivalence ratio is reached.

Premixing of fuel and air will normally result in too high temperatures at normal equivalence ratios for achieving low NO_x emissions. Partial premixing, however, can, especially in combination with other techniques, give large NO_x reductions.

Further details on NO_x formation and reduction can be found in literature such as [2], [6] and [7].

TYPICAL EXISTING LOW NO$_X$ BURNERS

Most manufacturers of fan driven gas burners offer special low-NO_x models or versions. Some examples are shown in Table 1. Values are assumed to be based on dry flue gas conditions. These numbers show that the concept studied can be comparable with leading technology both for large industrial burners and for smaller fan driven burners. Standard gas burners without special low NO_x emission focus will have emissions considerable above the values shown in Table 1. An example is the standard gas burner from Dreizler with a NO_x emission of up to 68 ppm. Generally, when converting a standard gas burner to a low NO_x version, an additional device is mounted in the burner tube outlet, and the maximum power output is somewhat lowered. This lowering varies between different models.

All examples in Table 1 are for natural gas, which generally gives lower NO_x emissions than if using propane as in most of the experiments discussed in this paper.

Table 1. Examples of typical low NO$_x$ burners without external flue gas recirculation and using natural gas as fuel.

Manufacturer	Approx. NO$_x$ emission	Approx. CO emission
Coen (industrial installation 3.5-17 MW)[a]	12-20 ppm	1-7 ppm
Dreizler (various fan driven models)[b]	20-45 ppm	Not specified
Giersch (various fan driven models)[c]	30-40 ppm	2-34 ppm
Weishaupt (various fan driven models)[d]	<45 ppm	28 ppm

a.   Coen Company Inc., 1510 Rollins Road, Burlingame, California 94010, USA. http://www.coen.com/
b.   Dreizler, Max-PlanckStrasse 1-5, 78549 Spaichingen, Germany. http://www.dreizler.com/
c.   Giersch, Postfach 3063, D-58662 Hemer, Germany. http://www.giersch.de/
d.   Weishaupt, D-88475 Schwendi, Germany. http://www.weishaupt.de/

A NOVEL SWIRL BURNER CONCEPT

The Swirl Burner is a partially premixed fan driven gas burner with internal flue gas recirculation and possibilities for staged fuel and air supply. A recirculation zone is set up due to the rotating air flow from the swirl generator. The swirl number for the rotating flow can be calculated as follows [8]:

$$ S = \frac{2}{3}\left(\frac{1-(d_h/d)^3}{1-(d_h/d)^2}\right)\tan\beta $$ (6)

where d_h is the diameter of the swirl generator hub, d is the outer diameter of the swirl generator and β is the exit angle of the vanes. In addition there will be a swirl efficiency factor reducing the true swirl number compared to the theoretical value. Swirl numbers higher than 0.6 are characterised as strong swirl, while swirl number below this value is characterized as weak swirl. For strong swirling flows, axial and radial pressure gradients are set up downstream the burner exit, resulting in the recirculation zone characteristic for this burner. Swirl numbers up to about 4 have been tested, and the stronger swirl tends to lower the NO$_x$-emissions.

As can be seen from Figure 1, the Swirl Burner consists of a cylindrical and a converging conical section. The burner uses a swirl generator with aerodynamically shaped swirl vanes for gas mixing and stabilization of the flame. Flue gas is recirculated into the centre of the cylindrical section, providing a continuous ignition source. Fuel gas is provided through a central tube which is held in position by the swirl generator. The design allows for axial adjust-

ment of both the gas tube and the swirl generator independently.
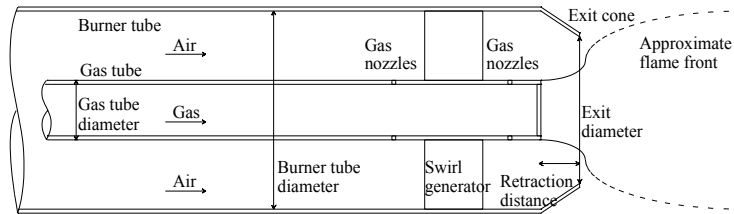
Figure 1. Schematic illustration of the swirl gas burner concept.

Gas nozzles can be placed both up- and downstream of the swirl generator for varying the degree of premixing. Nozzle area can be increased for lower gas pressure drop. A larger portion of the nozzles downstream of the swirl generator will also decrease gas pressure drop, but altering nozzle configuration can affect both emissions and stability. As an example, all nozzles placed downstream of the swirl generator will work fine for methane/natural gas, but not necessarily for propane. This is believed to be caused by different reactivity of the two gases. Swirl generators with different swirl numbers can be used. Lower swirl number will give lower pressure drop, both for the air and for the fuel gas, but will increase emissions. A swirl number in the range 2.0 - 4.0 as defined in Equation (6) is found practical and gives low emissions.
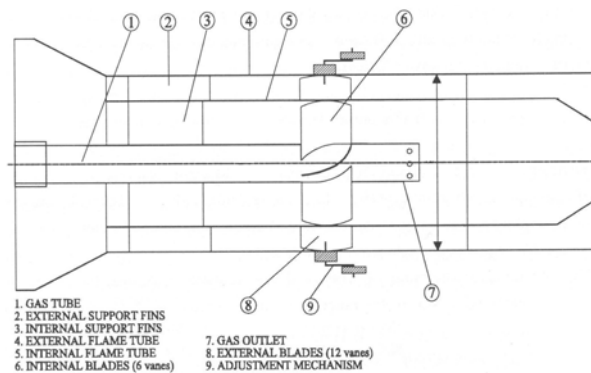
Figure 2. The Swirl Burner schematic for the first prototype [7].

The first burner prototype was designed to benefit from both staging of oxidizer and internal flue gas recirculation to give low emissions of NO_x. Secondary air was supplied through an outer tube as shown in Figure 2. This air could be supplied with varying degree of both co- and counter-swirl. Due to lower emissions and more simple design without staging of oxidizer, this version of the burner was abandoned when further revising this design. The revised design is shown in Figure 1.

TESTING OF THE FIRST PROTOTYPE

Experimental Setup

The experimental testing was conducted in a vertical down-draught boiler with straight through flow of the flue gases and with a maximum power output of 500 kW_{th}. Propane was used as fuel gas in these experiments. The flue gas composition was measured with a Signal Luminox Series 4000 NO_x analyser, a Sybron Taylor Servomex Series 500 O_2 analyser and a Hartmann & Braun Uras 3G CO/CO_2 analyser. The data was automatically logged to a computer.

Experimental Results

A primary air swirl number of 1.2 and a secondary air swirl number of ±0.8 were used in the experimental results presented. Tests without secondary air were also performed. The results are shown in Figure 3. CO emissions were kept below 10 ppmvd for equivalence ratios over 0.7. Co- and counter-swirl on the secondary air showed a significantly different behaviour which influenced the emissions. Co-swirl resulted in a longer flame with lower emissions and better stability than for counter-swirl. The Swirl Burner needed higher fan pressures than standard burners to generate the recirculating flow field.
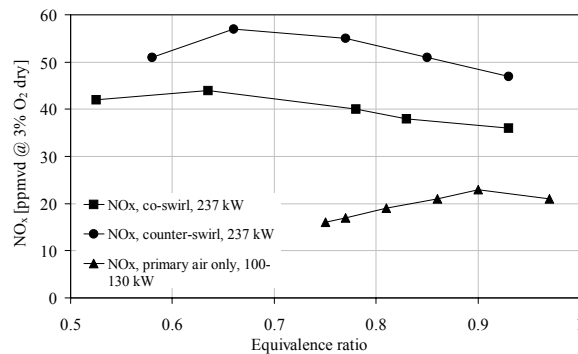
Figure 3. The Swirl Burner emissions as a function of equivalence ratio for 0-10% O_2 in the flue gas using propane as fuel with the first burner prototype [7].

Lowest emissions were found without secondary air. The burner is then operating without staged air supply and with good mixing and internal flue gas recirculation for NO_x emissions reduction. Operation down to 1% O_2 in the flue gas is possible. Emissions are comparable with leading technology for large industrial burners and better than for smaller existing low NO_x fan driven burners as shown in Table 1. There is still a potential for further optimization of the performance.

Due to these results, further work has been concentrated on a revised design with single stage air only as shown in Figure 1.

TESTING WITH THE REVISED DESIGN

Experimental Setup

The investigation was carried out on a 250 kW CEN (European Committee for Standardization) boiler as shown in Figure 4. Straight through flow of the flue gases were used in all tests. The power output was varied between 80 and 280 kW. Both methane and propane were used as fuel.

The flue gas composition (NO_x, CO and O_2) was monitored using the same gas analysing equipment as described for the first prototype testing.
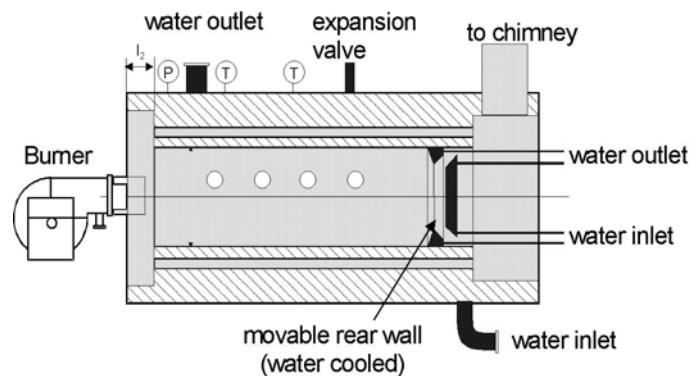
Figure 4. 250 kW CEN boiler.

Experimental Results

A nominal 200 kW burner design was first developed. NO_x emissions in the range 30-40 ppmvd at 3% oxygen for 100 - 200 kW are measured in most cases for propane as shown in Figure 5 and Figure 6. About 20 ppmvd NO_x emissions at 3% oxygen is measured for methane for 75-200 kW as shown in Figure 5. CO emissions were kept below about 5 ppmvd. NO_x and CO emissions were fairly constant over a wide range of fuel/air ratios. Similar results have also been obtained for a 20 kW burner and a 1 MW burner.
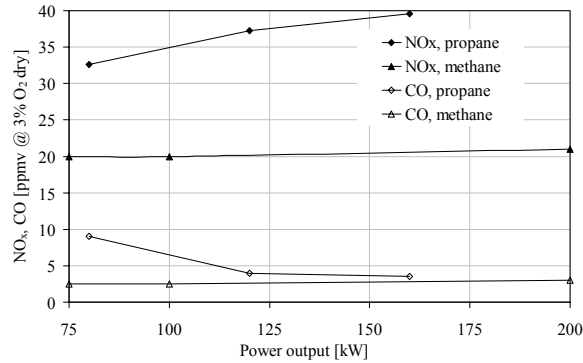
Figure 5. NO$_x$ and CO emissions as a function of power output and fuel. All tests were run at 3% O$_2$ in the flue gas.
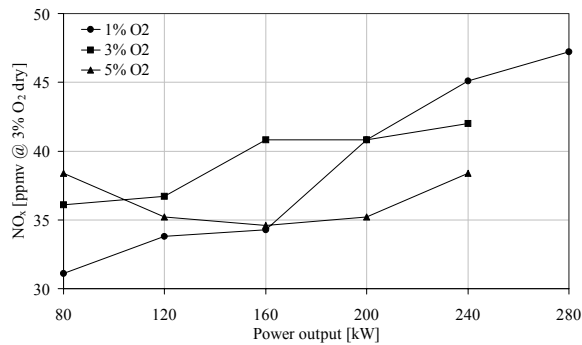
Figure 6. NO$_x$ emissions for propane as a function of power output. Tests performed for 1, 3 and 5% O$_2$ in the flue gas.

Influence of fuel nozzle arrangement on pollutant emissions and fuel gas pressure

Available fuel gas pressure can be a limiting factor on power output if total gas nozzle area is too small. Gas supplied upstream of the swirl generator will also have to work against a certain pressure. Positioning most of the fuel nozzles downstream of the swirl generator will therefore be beneficial. Experiments have been performed with varying gas nozzle area and positioning to optimize the burner for low emissions and stable combustion at a minimum fuel gas supply pressure.

Prior to these experiments the amount of fuel nozzles were equally distributed up- and downstream of the swirl generator. To reduce the necessary fuel gas supply pressure, all fuel nozzles were moved downstream of the swirl generator. The reason for this was to provide a lower back pressure for the fuel gas supply. To further reduce the pressure, the total nozzle area was increased. Un-

fortunately, this resulted in an unstable burner with a fluctuating flame zone and high emissions of NO_x and CO.

The instability was believed to be caused by the repositioning of the nozzles. Original positioning was therefore restored, but total nozzle area was increased with 50% and 100%. A 100% increase of the total nozzle area resulted in a slightly unstable burner at low power output and hence unacceptable high CO emissions. A 50% increase of the nozzle area resulted in lower fuel supply pressure, and a small reduction in NO_x emissions. This can be seen from the plot shown in Figure 7. The CO emissions are below 10 ppmvd except for the one case mentioned above.
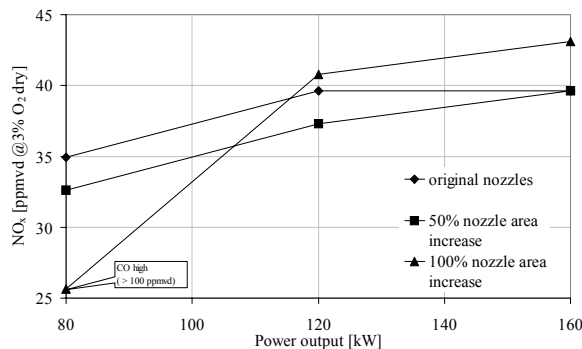
Figure 7. NO_x emissions with original positioning of fuel nozzles, varying the total nozzle area with propane as fuel.

Varying the swirl number

Another approach to reduce the fuel gas supply pressure as well as air supply pressure is to reduce the swirl number. Reducing the swirl number can be done by reducing the angle of the swirl blades, which in turn reduces the obstruction of the flow. Swirl generators with varying swirl number were tested to investigate the influence on emissions of NO_x from the burner. As can be seen from Figure 8, reducing the swirl number resulted in reduced fuel gas supply pressure, but NO_x-emissions were increased. Due to the flame stabilizing effect of the swirling flow, reduced swirl intensity resulted in a less stable combustion.

These experiments were carried out with an increase of the original nozzle area of 50% except the case with swirl number 0.9. This was tested with the original nozzle area, hence the dotted line in Figure 8.

Swirl numbers below 0.9 did not stabilize the flame at all.
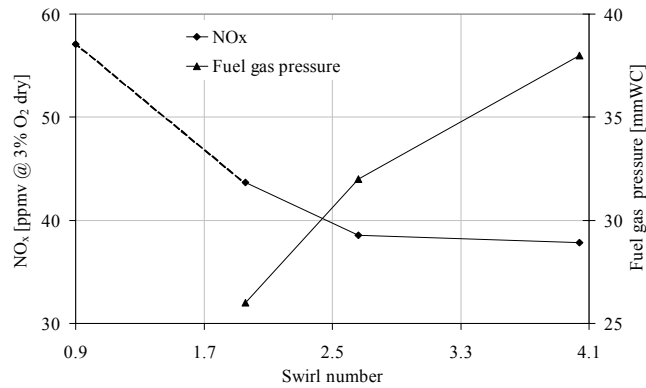
Figure 8. NO$_x$ emissions and fuel supply pressure as a function of the swirl number. Tests performed with 3% O$_2$ in the flue gas and propane as fuel.

Position of the gas tube

It has been experienced that the position of the gas tube relative to the burner tube is a sensitive parameter. Earlier experiments by Røkke [7] positioned the gas tube 10 cm inside the burner tube (Figure 2), while recently this parameter has been changed to 2 cm (Figure 1). Due to this variation, it was desirable to investigate how this affected the NO$_x$ emissions. The results plotted in Figure 9 shows that the emissions can be reduced by positioning the gas tube about 7 cm or further inside the burner tube.
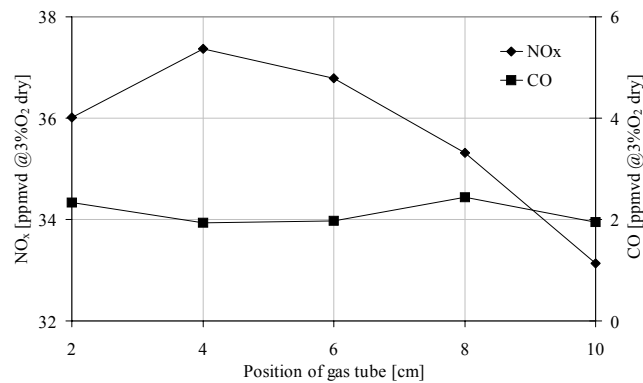
Figure 9. Positioning of the gas tube relative to the exit of the burner tube. Tests conducted at 120 kW power output and 3% O$_2$ in the flue gas.

Optimizing the nozzle arrangement for methane as fuel

Due to the laboratory facilities, most of the experiments have been under-

taken using propane as fuel. Some tests were performed to find an optimum nozzle arrangement with methane as fuel gas. Lowest NO_x-emissions were attained with the same nozzle distribution and total area as for propane. There were not observed any instabilities when burning methane with the same nozzle configurations earlier tested with propane. This implies that when burning methane, the nozzle configuration can be chosen more freely. As can be seen from Figure 10, different nozzle arrangements can be used depending on if low NO_x or low fuel gas supply pressure is the most important. The emissions of CO is well below 10 ppmvd for all nozzle configurations, except the case with smallest nozzle area.
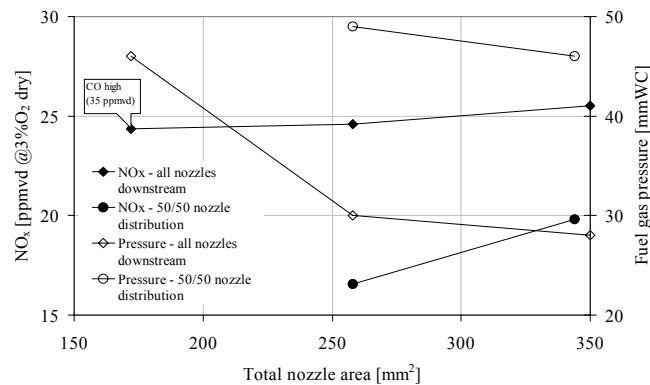
Figure 10. NO_x emissions and fuel gas pressure using methane as fuel, varying total nozzle area and distribution of fuel nozzles relative to the swirl generator.

DISCUSSION OF EXPERIMENTAL RESULTS

Tests with the first burner prototype using propane as fuel (Figure 3), were very promising without secondary air. These experiments were conducted in the vertical boiler, and the results could not be completely verified in the smaller CEN-boiler used in recent tests (Figure 5 and Figure 6).

The variation in experimental results from the vertical boiler and the CEN boiler have been experienced with different types of burners. The vertical boiler has in some cases shown a reduction in NO_x emissions of a factor of 2 compared to experiments using the CEN boiler with the same burners. This behaviour can be understood by considering the different conditions in these boilers. The vertical boiler was cooled by tap water (10 °C), while the CEN boiler has a cooling circuit where the temperature is kept constant at 70 °C, resulting in a significant difference in the combustion chamber wall temperature in the two boilers. The volume of the combustion chamber in the vertical boiler is also greater than in the CEN boiler, giving a lower combustion chamber heat

load. Both reduced wall temperature and reduced combustion chamber heat load will lead to a significant reduction in the flame temperature and hence reduction in the emissions of NO_x. Therefore, in this paper, the NO_x emissions shown in Figure 3 are used as a guide only, to compare the difference in emission performance when using two stage and single stage oxidizer, since they are not obtained in a standard boiler.

The above mentioned results lead to a revised burner design with no secondary oxidizer. The original idea of this design was to utilize both internal recirculation induced by the swirling flow, and air staging to achieve low emissions of NO_x. As can be seen from Figure 3, neither counter- nor co-swirl gave the desired results. According to Røkke [7] this can be explained by the mixing mechanisms of the primary and the secondary swirling flow. Between these flows there is a rotating shear-layer, in which the mixing occurs. In the counter-swirling flow, the shear forces are high, resulting in intense turbulence and rapid mixing, creating a short flame with high volumetric heat release, and hence increased NO_x-production. The counter-swirl flame has a premixed behaviour and there is no recirculation zone transferring products back to the combustion. In the co-swirling flow the shear forces are small, resulting in little mixing of oxidizer into the primary flow. Due to the centrifugal forces, the flame struggles to get rid of combustion products.

It is believed that the single stage oxidizer burner design shown in Figure 1 takes full advantage of internal product recirculation induced by the swirling flow. Combining this mechanism with two-stage oxidizer as the first prototype, disturbs the recirculation and reduces the intended mission of the swirling flow, resulting in an increase of NO_x-emissions.

Varying the total nozzle area of the burner resulted in an optimized nozzle configuration for low NO_x-emissions. Figure 7 shows that the NO_x production can be reduced by increasing the area of the nozzles, but it also shows that increasing this area too much results in higher NO_x emissions. This suggests that a 50% increase of the nozzle area results in an ideal fuel jet trajectory through the oxidizer. An expression for the trajectory of a jet penetrating into a cross-flow [9] has been used to investigate how the different fuel nozzles tested affects the fuel distribution. Based on pressure measurements, the fuel injected into the oxidizer is found to be distributed with 35% upstream and 65% downstream of the swirl generator. The fuel trajectories computed from [9] using velocities corresponding to 120 kW power output is plotted in Figure 11. How well this equation predicts the fuel distribution can be disputed, and therefore this plot is only assumed to be a qualitative guidance. It indicates however that the paths of the fuel jet trajectories changes with the different nozzles. Fuel from all the upstream nozzles has a trajectory close to the gas tube, while the downstream fuel trajectories have a stronger dependence on the nozzle size. This proposes that the production of NO_x depends on how the fuel is mixed

into the oxidizer, and that different nozzle arrangements results in a more or less favourable fuel trajectory path with regards to the NO$_x$ emissions.
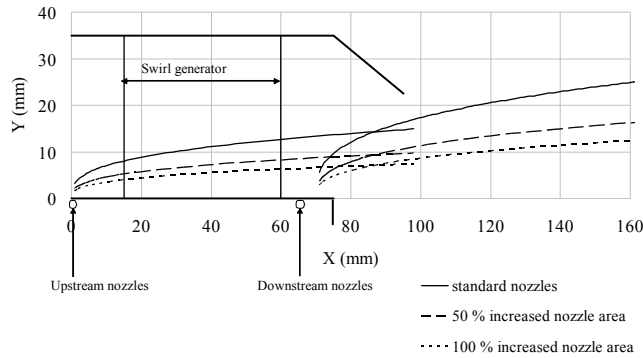
Figure 11. Trajectory of fuel jet in oxidizer crossflow, correlation from [9]. Burner geometry are also indicated.

The experiments have shown that the swirl intensity and hence the swirl number is an important parameter to reduce the emissions of NO$_x$. This can be seen from Figure 8. The recirculation of combustion products back to the core of the of the swirling flow increases with the intensity of the swirl [9]. This agrees with the fact that product recirculation will reduce the production of thermal NO$_x$ by lowering the combustion temperature.

Besides providing product recirculation, the swirling flow helps to stabilize the flame. Experiments were carried out to investigate the influence of swirl by reducing the vane angle of the swirl generator. This lead to poor flame stabilization, and with a swirl number below 0.9, the flame did not stabilize and blew off.

The axial position of the gas tube relative to the burner tube exit was assumed to be a sensitive parameter. This has earlier been experienced when demonstrating the burner at an external lab. The demonstration was carried out using natural gas from Russia containing about 99% methane. This behaviour was not observed when using propane as fuel. From Figure 9 it can be seen that the NO$_x$ emissions only changes slightly (33 to 37 ppmvd) with the gas tube position.

Experiments undertaken using methane as fuel have indicated that the stability is less sensitive to the fuel nozzle configuration. The combustion has been stable both with all fuel nozzles placed downstream the swirl generator, and with equal amount of fuel nozzles placed on each side of the swirl generator. The unstable behaviour observed when burning propane, where the flame front occasionally propagates into the burner tube in a fluctuating way, can be explained by the different reactivity of the fuels. A propane-air mixture is more reactive than a methane-air mixture [10]. This implies that a deflagration

of a propane-air mixture will accelerate faster than a methane-air mixture, resulting in the unstable behaviour observed with propane.

This result means that when using methane as fuel, the fuel nozzle geometry can be more freely chosen. As can be seen from Figure 10, distributing all fuel nozzles downstream the swirl generator gives reduced fuel pressure, but increased NO_x emissions. Distributing equal amount of the nozzle area on both sides of the swirl generator increases the fuel pressure, but gives lower emissions of NO_x.

CONCLUSIONS

A novel swirl gas burner concept has been developed. Experiments have been performed to investigate the influence of changes in the burner geometry on the emissions of NO_x and fuel supply pressure.

The swirl burner employs internal flue gas recirculation as a NO_x reduction technique and for flame stabilization. This is obtained by the strong swirling flow, where combustion products are transferred back to the core of the flame. Experiments have shown that combining this technique with other NO_x-reducing techniques may interfere with the swirling flow, and hence reduce the internal recirculation and increase the emissions of NO_x.

Further experiments on the revised design have been carried out to investigate how the emission performance of the burner can be optimized by varying geometrical parameters. A favourable configuration of fuel nozzles has been found. This includes specifications about both the nozzle distribution relative to the swirl generator and the total area of the fuel nozzles. Further, the necessary swirl number to give a stable combustion and to minimize emissions is found. The best configuration found for propane as fuel gas has achieved a NO_x emission of 36 ppmvd @3% O_2 in the flue gas and 120 kW power output.

The best methane configuration has achieved NO_x emission of 16 ppmvd @ 3% O_2 in the flue gas and 120 kW power output.

ACKNOWLEDGEMENTS

APPENDIX A

NOMENCLATURE

d	diameter of swirl generator
d_h	diameter of swirl generator hub
k	reaction rate coefficient
mmWC	millimetre water column
ppmvd	parts per million volume dry
S	swirl number
t	time
β	exit angle of swirl vanes

REFERENCES

1. U.S. Environmental Protection Agency. NO_x - How Nitrogen Oxides Affect the Way We Live and Breathe. EPA Report, EPA-456/F-98-005, 1998.

2. Bowman, C.T. Control of Combustion-generated Nitrogen Oxide Emissions: Technology Driven by Regulation. 24th Symposium (Int.) on Comb., 1992; 859-878; The Combustion Institute, Pittsburgh.

3. Slungaard, T., Engebretsen, T. and Sønju, O.K. Development of Low NO_x Gas Burner Technology. 1st Biennal Meeting, Scand.-Nord. Sect. Comb. Inst., April 2001, Gothenburg, Sweden; 287-292.

4. Zeldovich, Y.B. (1946). The Oxidation of Nitrogen in Combustion and Explosions. Acta Physicochimica U.R.S.S., Vol. 21, 577-628, 1946.

5. Fenimore, C.P. Formation of Nitric Oxide in Premixed Hydrocarbon Flames, 13th Symposium (Int.) on Comb., 1971; 373-380; The Combustion Institute, Pittsburgh.

6. Warnatz, J., Maas, U. and Dibble, R.W. *Combustion, Physical and Chemical Fundamentals, Modelling and Simulation, Experiments, Pollutant Formation, Second Edition*, Springer-Verlag Berlin Heidelberg New York, 1999, ISBN 3-540-65228-0.

7. Røkke, N.A. *Experimental and Theoretical Studies of Environmental Aspects of Natural Gas Combustion*, Ph.D. Thesis, The Norwegian Institute of technology, Department of Thermal Energy and Hydropower, Trondheim, Norway, 1994.

8. Gupta, A.K., Lilley, D.G. and Syred, N. *Swirl Flows,* Abacus Press, Tunbridge Wells, 1984, ISBN 0-85626-175-0.

9. Lefebvre, A.H. *Gas Turbine Combustion, Second Edition*, Taylor & Francis Philadelphia, 1999, ISBN 1-56032-673-5.

10. Bjerketvedt, D., Bakke, J.R. and van Wingerden, K. *Gas Explosion Handbook, Version 1.2*, Christian Michelsen Research, Bergen, Norway, 1993, pp 71-72.

APPENDIX A

APPENDIX B - INPUT FILE FOR CALCULATION OF A LAMINAR PREMIXED FLAT FLAME USING PREMIX

```
RSTR
USTG
TDIF
/   burner stabilised flame
BURN
TGIV
/   begin on a uniform mesh of 28 points
NPTS  28
/   definition of the computational interval
XSTR  0.0
XEND 1.6
XCEN  0.3
WMIX  2.0
/   pressure and inlet mass flow rate
PRES  1.0 (atmospheres)
FLRT  0.0072442407 (g/cm**2-sec)
/   temperature to be fixed for  the flame speed computation
TFIX  400.0
/   adaptive mesh criteria
GRAD   0.2
CURV   0.2
/   unreacted mole fractions
MOLE
REAC CH4 0.067713
REAC O2  0.195780
REAC N2  0.736507
/
/   estimated products
PROD  CH4 1e-7
PROD  H2O 0.16
PROD  O2  0.03
PROD  CO2 0.08
PROD  CO  0.00002
PROD  H2  0.067
PROD  H   0.004
PROD  CH3 2e-3
PROD  O   5e-4
PROD  OH  2e-4
PROD  N2  0.72
/   estimated peak intermediate mole fractions
INTM   HO2   0.00004
INTM   O     0.0006
```

```
INTM  H     0.0005
INTM  OH    0.003
INTM  CH2   0.0002
INTM  CH    0.00003
INTM  CH3   0.0003
/
/   tolerances for the Newton iteration
ATOL  1.0e-18
RTOL  1.E-4
/   tolerances for the time step Newton iteration
ATIM  1.E-18
RTIM  1.E-3
/   print control
PRNT   2
/   in the event of a Newton failure
TIME   100 5.00E-7
TIM2   200 1.00E-6
/
/   Measured uncorrected TEMPerature
/
/         X [cm]      T [K]
/TEMP  0.0000E+00  1.2990E+03
/TEMP  5.0000E-02  1.6160E+03
/TEMP  1.0000E-01  1.8480E+03
/TEMP  1.5000E-01  1.9290E+03
/TEMP  2.0000E-01  1.9170E+03
/TEMP  2.5000E-01  1.9000E+03
/TEMP  3.0000E-01  1.8880E+03
/TEMP  3.5000E-01  1.8830E+03
/TEMP  4.0000E-01  1.8770E+03
/TEMP  4.5000E-01  1.8710E+03
/TEMP  5.0000E-01  1.8650E+03
/TEMP  5.5000E-01  1.8600E+03
/TEMP  6.0000E-01  1.8540E+03
/TEMP  6.5000E-01  1.8540E+03
/TEMP  7.0000E-01  1.8480E+03
/TEMP  7.5000E-01  1.8480E+03
/TEMP  8.0000E-01  1.8420E+03
/TEMP  8.5000E-01  1.8390E+03
/TEMP  9.0000E-01  1.8370E+03
/TEMP  9.5000E-01  1.8310E+03
/TEMP  1.0000E+00  1.8310E+03
/TEMP  1.0500E+00  1.8270E+03
/TEMP  1.1000E+00  1.8250E+03
/TEMP  1.2000E+00  1.8190E+03
/TEMP  1.3000E+00  1.8140E+03
/TEMP  1.4000E+00  1.8080E+03
```

/TEMP 1.5000E+00 1.8030E+03
/TEMP 1.6000E+00 1.7970E+03
/
/ 1. corrected temperature, using velocities from previous calculation
/ d=3.5e-4 e=0.22 NPTS=28
/   X   T_corr
/TEMP 0.0000E+00 1.3350E+03
/TEMP 5.0000E-02 1.6938E+03
/TEMP 1.0000E-01 1.9764E+03
/TEMP 1.5000E-01 2.0809E+03
/TEMP 2.0000E-01 2.0651E+03
/TEMP 2.5000E-01 2.0430E+03
/TEMP 3.0000E-01 2.0276E+03
/TEMP 3.5000E-01 2.0210E+03
/TEMP 4.0000E-01 2.0133E+03
/TEMP 4.5000E-01 2.0056E+03
/TEMP 5.0000E-01 1.9980E+03
/TEMP 5.5000E-01 1.9916E+03
/TEMP 6.0000E-01 1.9840E+03
/TEMP 6.5000E-01 1.9840E+03
/TEMP 7.0000E-01 1.9764E+03
/TEMP 7.5000E-01 1.9764E+03
/TEMP 8.0000E-01 1.9688E+03
/TEMP 8.5000E-01 1.9650E+03
/TEMP 9.0000E-01 1.9625E+03
/TEMP 9.5000E-01 1.9549E+03
/TEMP 1.0000E+00 1.9549E+03
/TEMP 1.0500E+00 1.9499E+03
/TEMP 1.1000E+00 1.9474E+03
/TEMP 1.2000E+00 1.9397E+03
/TEMP 1.3000E+00 1.9335E+03
/TEMP 1.4000E+00 1.9260E+03
/TEMP 1.5000E+00 1.9197E+03
/TEMP 1.6000E+00 1.9123E+03
/
/ 2. corrected temperature, using velocities from previous calculation
/ d=3.5e-4 e=0.22 NPTS=28
/   X   T_corr
/TEMP 0.0000E+00 1.3348E+03
/TEMP 5.0000E-02 1.6933E+03
/TEMP 1.0000E-01 1.9756E+03
/TEMP 1.5000E-01 2.0798E+03
/TEMP 2.0000E-01 2.0641E+03
/TEMP 2.5000E-01 2.0420E+03
/TEMP 3.0000E-01 2.0265E+03
/TEMP 3.5000E-01 2.0201E+03
/TEMP 4.0000E-01 2.0125E+03

```
/TEMP   4.5000E-01   2.0048E+03
/TEMP   5.0000E-01   1.9970E+03
/TEMP   5.5000E-01   1.9907E+03
/TEMP   6.0000E-01   1.9831E+03
/TEMP   6.5000E-01   1.9831E+03
/TEMP   7.0000E-01   1.9755E+03
/TEMP   7.5000E-01   1.9755E+03
/TEMP   8.0000E-01   1.9679E+03
/TEMP   8.5000E-01   1.9641E+03
/TEMP   9.0000E-01   1.9616E+03
/TEMP   9.5000E-01   1.9541E+03
/TEMP   1.0000E+00   1.9541E+03
/TEMP   1.0500E+00   1.9490E+03
/TEMP   1.1000E+00   1.9465E+03
/TEMP   1.2000E+00   1.9390E+03
/TEMP   1.3000E+00   1.9328E+03
/TEMP   1.4000E+00   1.9253E+03
/TEMP   1.5000E+00   1.9191E+03
/TEMP   1.6000E+00   1.9116E+03
/
/   Final radiation corrected temperature profile
/   d=3.5e-4 e=0.22 NPTS=28
/   X         T_corr
TEMP   0.0000E+00   1.3348E+03
TEMP   5.0000E-02   1.6933E+03
TEMP   1.0000E-01   1.9756E+03
TEMP   1.5000E-01   2.0798E+03
TEMP   2.0000E-01   2.0641E+03
TEMP   2.5000E-01   2.0420E+03
TEMP   3.0000E-01   2.0265E+03
TEMP   3.5000E-01   2.0201E+03
TEMP   4.0000E-01   2.0125E+03
TEMP   4.5000E-01   2.0048E+03
TEMP   5.0000E-01   1.9970E+03
TEMP   5.5000E-01   1.9907E+03
TEMP   6.0000E-01   1.9831E+03
TEMP   6.5000E-01   1.9831E+03
TEMP   7.0000E-01   1.9755E+03
TEMP   7.5000E-01   1.9755E+03
TEMP   8.0000E-01   1.9679E+03
TEMP   8.5000E-01   1.9641E+03
TEMP   9.0000E-01   1.9616E+03
TEMP   9.5000E-01   1.9541E+03
TEMP   1.0000E+00   1.9541E+03
TEMP   1.0500E+00   1.9490E+03
TEMP   1.1000E+00   1.9465E+03
TEMP   1.2000E+00   1.9390E+03
```

```
TEMP   1.3000E+00   1.9328E+03
TEMP   1.4000E+00   1.9253E+03
TEMP   1.5000E+00   1.9191E+03
TEMP   1.6000E+00   1.9116E+03/
/
END
```

APPENDIX B

APPENDIX C - UDF FUNCTION TO GENERATE SWIRL IN CFD MODEL

```
/* ****************************************************************** */
/*                                                                    */
/* UDF to generate Swirl                                              */
/*                                                                    */
/* UDF to modify the tangential (swirl)                               */
/* velocity by using axial velocity as                                */
/* input in a 2D annulus (or cylinder).                               */
/*                                                                    */
/* Velocity is given a tangential                                     */
/* component equivalent to what a curved                              */
/* swirl vane would.                                                  */
/* Tang_vel = axial_vel*tan(Beta)                                     */
/* Beta = exit angle of swirl vane                                    */
/*                                                                    */
/* For details on the discretization                                 */
/* and linearization, see below.                                      */
/* ****************************************************************** */

#include "udf.h"
#define Beta 60. /*Exit angle of swirler*/
#define PI 3.14159265359
#define WEIGHT 1.e20

DEFINE_SOURCE(user_swirl, cell, thread, dS, eqn)
{
real swirl_vel, x[3], y, source;
/*float swirl_vel, x[3], y, source;*/
C_CENTROID(x, cell, thread);

y=x[1]; /* y-coord, radius */
swirl_vel=(C_U(cell, thread))*(tan(Beta*PI/180)); /*swirl vel in cell*/

/* returning the linearized source (see below) */
source=WEIGHT*(swirl_vel-C_WSWIRL(cell, thread));
dS[eqn]=-WEIGHT;

return source;
}

/* ****************************************************************** */
/* A source term is linearized as follows: S(fi) = A + B*fi,          */
/* where fi is the unknown scalar in each node.                       */
```

```
/*                                                                    */
/* To assign fi to a desired value, as an internal boundary condition */
/* fi_desired, the linearization of the source is done as follows:    */
/* A = WEIGHT*fi_desired                                              */
/* B = -WEIGHT                                                        */
/* where WEIGHT is a BIG value (i.e. 1.e20)                           */
/*                                                                    */
/* S(fi) is now so big, that any other part of the discretized        */
/* transport equation is negligible, leaving only the source to       */
/* calculate fi in each node, as follows:                             */
/*                                                                    */
/* A + B*fi ~ 0                                                       */
/* fi = -A/B = -WEIGHT*fi_desired/-WEIGHT = fi_desired                */
/*                                                                    */
/* Using DEFINE_SOURCE in Fluent, source = A and dS[eqn] = B          */
/* This will returns any desired value for each cell in the chosen    */
/* internal thread.                                                   */
/*                                                                    */
/* References:                                                        */
/* Fluent 6.0 UDF manual, chapter 4.3.8                              */
/* Patankar, S.V., Numerical heat Transfer and Fluid Flow, p145       */
/* ************************************************************ */
```